THE RELATIVE ABUNDANCES OF Sn, Te, Xe, Ba, and Ce IN THE COSMIC RADIATION

Thesis by

Keith E. Krombel

In Partial Fulfillment of the Requirements

for the Degree of

Doctor of Philosophy

California Institute of Technology

Pasadena, California

1983

(Submitted May 24, 1983)

ACKNOWLEDGEMENTS

This thesis is truly the result of many hands and minds. First, thanks are due to my advisor, Dr. Edward Stone, for his guidance. Then there is the rest of the HEAO team: Dr. M.H. Israel, Dr. C.J. Waddington, Dr. J. Klarmann, Dr. W.R. Binns, Dr. R.K. Fickle, and Dr. T.L. Garrard. Nancy Brewster provided many helpful propagation calculations which are much appreciated.

Thanks are due also to the programming staff both at Washington University, fellow HEAOid Dave Grossman, and at Caltech, Nancy Collins, especially helpful in the final days, and Brownlee Gauld and Shelley Mjolsness. These people have provided not only programming assistance but personal support and relief from the rigors of physics when necessary. Also included among this number must be Randy Burrell and family.

Fellow graduate students who have contributed to making the years of study more pleasant are Dr. John Spalding, Dr. Neil Gehrels, and especially Dr. Jim Zumberge and wife Cindie. Among the current grads who must be mentioned are Brian Newport, a HEAOid, and Eric Aslakson, whose friendship did much to make the office a more livable place.

In the purely personal realm, the number worthy of mention is large and long. I will mention only two, however, Dan Sallitt and Mike Spagnuolo, fellow Wilkes-Barre natives who have remained friends through the many changes of the past seven years. For the rest, an insufficient thank you for all the comfort provided. It will be sad to leave many of the people I have met here.

Thanks are also due to the National Science Foundation for a three year fellowship and to Caltech for tuition fellowships. This research was supported in part by NASA under contracts NAS 8-27976, 77, 78 and grants NGR 05-002-160, 24-005-050, and 26-008-001.

ABSTRACT

Elements with even atomic number (Z) in the interval $50 \leq Z \leq 58$ have been resolved in the cosmic radiation using the Heavy Nuclei Experiment on the HEAO-3 satellite. Their relative abundances have been compared with the results expected from pure r-process material, pure s-process material, and solar system material, both with and without a modification due to possible first ionization potential effects. Such effects may be the result of the preferential acceleration, and hence enhancement in the cosmic rays, of those elements having low first ionization potentials. We find that our measurements are inconsistent with pure r-process material at the greater than 98% confidence level whether or not the first ionization potential adjustments are made.

In addition, we have compared our results with mixtures having varying ratios of pure r-process material to pure s-process material. We find that, if no first ionization potential effects are included,

$$\frac{(r/s)_{CRS}}{(r/s)_{SS}} = 0.20^{+0.18}_{-0.14}$$

where CRS refers to the cosmic ray source and SS refers to the solar system, consistent with having an almost pure s-process source. If the first ionization potential adjustments are applied

$$\frac{(r/s)_{CRS}}{(r/s)_{SS}} = 1.5^{+1.1}_{-0.7}$$

consistent with a solar system mixture.

Table of Contents

I. INTRODUCTION

Galactic cosmic rays are highly energetic particles in space, one of the few samples of extra-solar material available for direct study. As such, knowledge of their elemental and isotopic composition should ultimately help us to understand the processes of nucleosynthesis responsible for their formation and for the formation of the chemical elements in general. For many lower charge nuclei the elemental composition of the cosmic radiation has already been reasonably well determined. For a much lesser number the isotope ratios have also been determined and, in some cases, show significant differences from the composition of the solar system (see e.g. Mewaldt 1983 and references therein). However, for approximately 2/3 of the periodic table, those elements heavier than iron (i.e. atomic number, Z, greater than 26), relatively little detail is known about the elemental, and nothing at all about the isotopic, cosmic ray abundances. Although comprising only a small fraction of the cosmic ray flux, and of the solar system, these elements are important because the processes believed responsible for their formation constitute a distinct class of events which can best be studied in this charge range. This thesis will discuss measurements of a limited, but important, region from $_{50}$Sn to $_{58}$Ce, where differences between the possible nucleosynthesis mechanisms are particularly evident.

Figure 1.1 is a graphic presentation of the abundances of the chemical elements in the solar system as compiled by Anders and Ebihara (1982). The vertical axis is logarithmic in order to display the full range of variation present. Although these are the solar abundances (derived in large part from meteorite studies), to a rough first order the cosmic ray elemental abundances follow a similar curve. Note the general decline in abundance as one proceeds up scale, some 4-5 orders of magnitude from hydrogen to iron (Z=26), with an even sharper decrease

Figure 1.1

The abundances of the chemical elements in the solar system as compiled by Anders and Ebihara (1982).

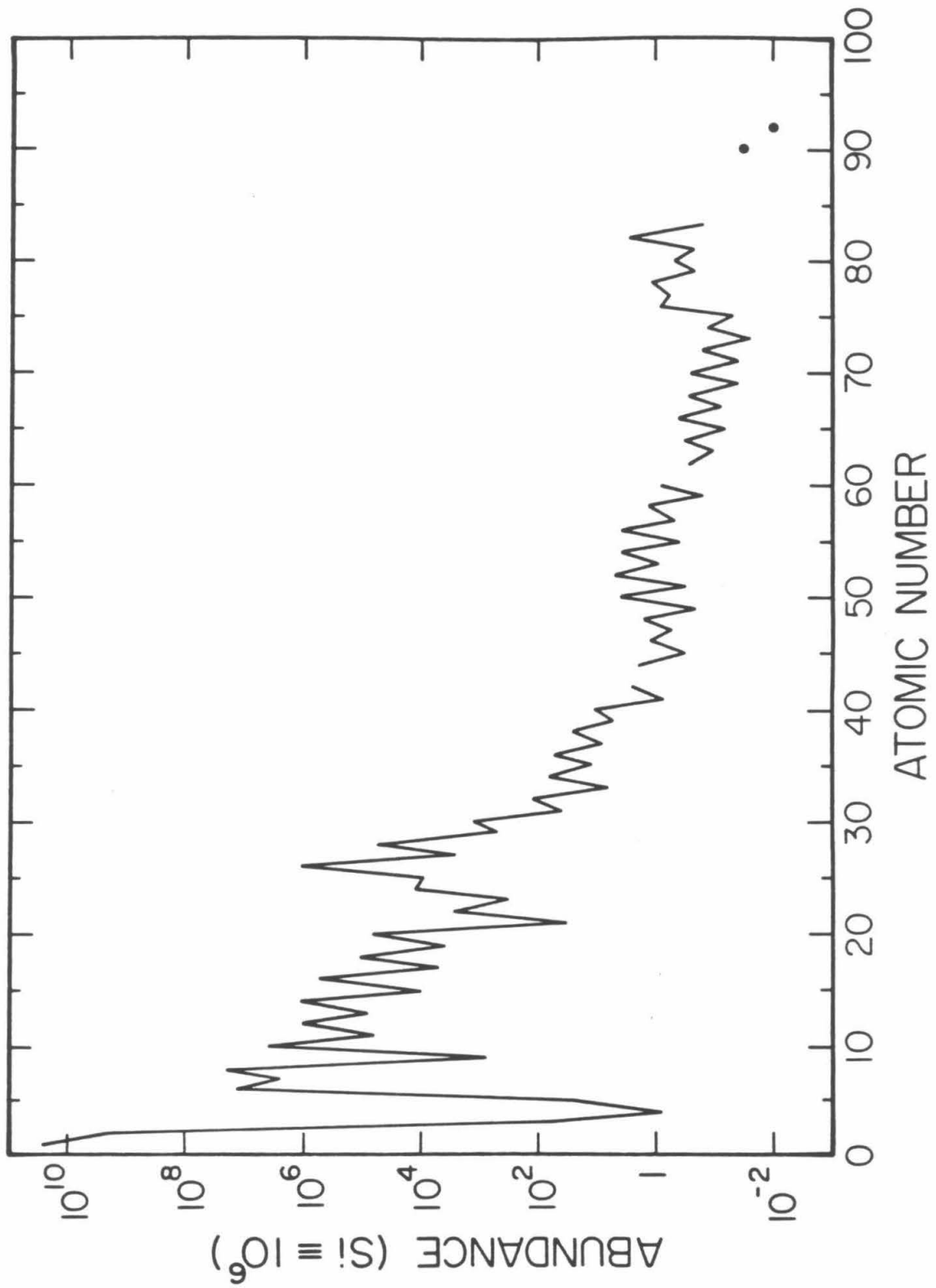
ABUNDANCE (Si ≡ 10^6)
10^10
10^8
10^6
10^4
10^2
1
10^-2
0
10
20
30
40
50
60
70
80
90
100
ATOMIC NUMBER

immediately above iron. The ultra-heavy component, $Z \geq 30$, is approximately 4 orders of magnitude less abundant than iron. Note also the moderate abundance increase in the charge 50-60 region which falls off again above charge 58.

Theories of nucleosynthesis, which attempt to explain the features of the solar system and "cosmic" abundances in terms of nuclear processes occurring in stars, have been quite successful in reproducing the general features of this curve. One of the pioneering papers in this field is that of Burbidge, Burbidge, Fowler and Hoyle (1957). The formation of the elements below iron is mainly the result of charged particle interactions which also serve as a stellar energy source. However, the synthesis of the elements above iron cannot be explained using these processes. By the time one reaches iron, the coulomb barrier between the interacting charged nuclei is so large that the temperature required to provide a particle with enough energy to penetrate the barrier will also disrupt the product nucleus. In addition, iron lies at the maximum in the binding energy per nucleon curve making formation of higher charged particles energetically unfavorable. It was Burbidge *et al.* (1957) who first clearly explained the formation of the elements above iron by means of neutron capture processes, thereby avoiding the coulomb barrier problems.

These processes start with a "seed" nucleus, the result of prior nucleosynthesis, and a source of neutrons. The seed nuclei go through a sequence of neutron captures and beta decays continuing until the onset of fission or exhaustion of the neutron source. The seed is usually assumed to be a member of the iron group, the nuclides in the vicinity of the maximum in the binding energy per nucleon curve, most commonly ^{56}Fe. The source of neutrons is still a matter of some debate with the reactions $^{13}C(\alpha,n)^{16}O$ and $^{22}Ne(\alpha,n)^{25}Mg$ two likely candidates proposed by Cameron (1955, 1960). The two main processes are actually the two

extreme cases of a more general neutron capture process (Blake and Schramm 1976). These are the r (rapid) and the s (slow) process.

In the s-process, the flux of neutrons is low enough that the time between subsequent neutron captures is large compared with the beta decay time of any unstable nucleus encountered. As a result, the s-process follows a path along the valley of beta stability. Figure 1.2 is a schematic chart of the nuclides adapted from Norman and Schramm (1979) illustrating the neutron capture path of the s-process. The horizontal axis is the neutron number, N, and the vertical axis is the atomic number, Z. Stable nuclei are indicated by dots. Figure 1.3 is a detail of the chart in the Sn-Ce region where the stable nuclides are now indicated by a box with the mass number, A, inside. If we start at ^{116}Sn, the s-process path proceeds by neutron capture through the heavier isotopes of Sn until reaching ^{121}Sn which, unstable with a half life of 2.8 hours, undergoes beta decay and becomes ^{121}Sb before capturing another neutron. As a result, ^{122}Sn and ^{124}Sn are not formed in the classic s-process. The path continues in this same fashion along the valley of beta stability, bypassing the isolated neutron rich isotopes such as ^{128}Te and ^{134}Xe.

The classic r-process is at the other extreme. Here the flux of neutrons is extremely large with the neutron capture times assumed to be very much less than the beta decay times of the nuclides involved. As a result, the path of the r-process progresses through extremely neutron rich nuclei far from the valley of beta stability. The location of the path is determined by $(n,\gamma)-(\gamma,n)$ reactions which prevent further neutron addition when the binding energy of the extra neutron is insufficient to prevent dissociation by the ambient photon gas (the neutron drip line). In a more generalized r-process (Blake and Schramm 1976), the "path" is determined by the place where the beta decay times of the increasingly neutron rich nuclei become comparable with the neutron capture times.

Figure 1.2

A schematic chart of the nuclides adapted from Norman and Schramm (1979) showing the paths of the r-process and the s-process. Neutron number is along the horizontal axis and atomic number is along the vertical. Stable nuclei are indicated by dots. Also shown are the neutron and proton magic numbers.

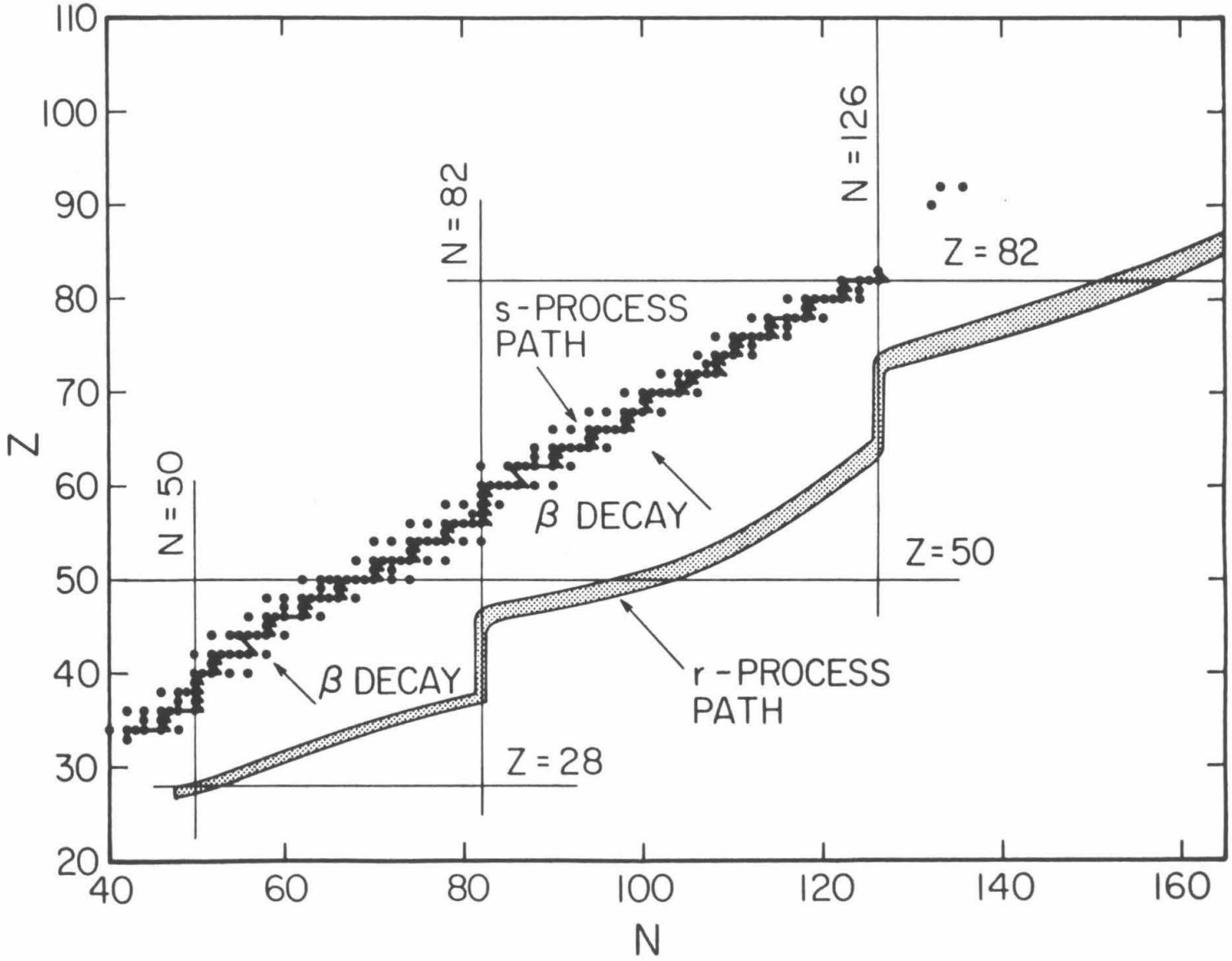
110
100
90
80
70
60
50
40
30
20
Z
40
60
80
100
120
140
160
N
N = 50
N = 82
N = 126
Z = 82
Z = 50
Z = 28
s - PROCESS
PATH
β DECAY
β DECAY
r - PROCESS
PATH

Figure 1.3

A detail of the chart of the nuclides in the $_{50}$Sn - $_{58}$Ce region. The vertical axis is the atomic number (element) and the horizontal axis is the neutron number. Mass numbers are indicated for the stable nuclides. The light diagonal lines are meant to suggest the beta decay of the results of r-process nucleosynthesis.

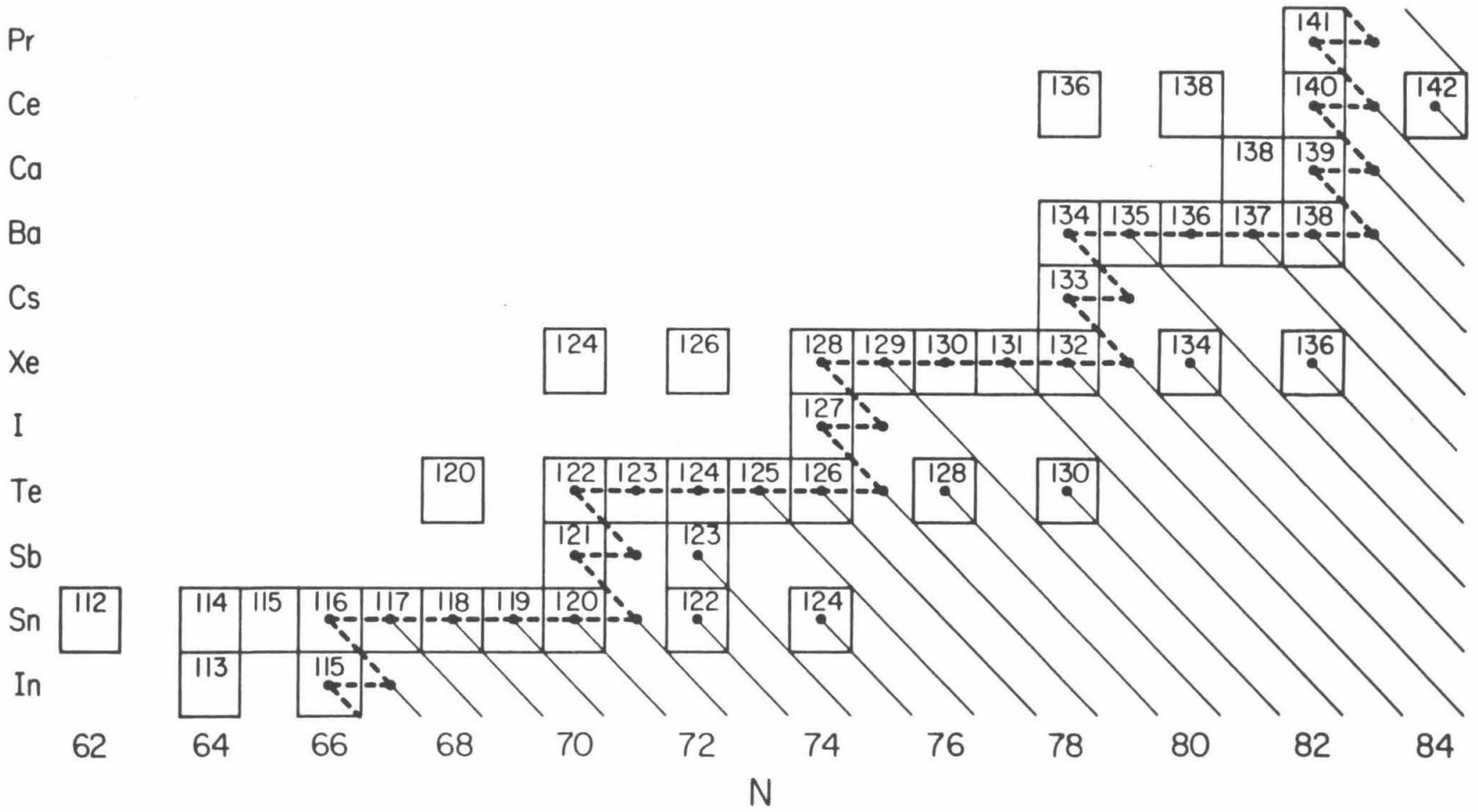
Pr
Ce
Ca
Ba
Cs
Xe
I
Te
Sb
Sn
In
141
136
138
140
142
138
139
134
135
136
137
138
133
124
126
128
129
130
131
132
134
136
127
120
122
123
124
125
126
128
130
121
123
112
114
115
116
117
118
119
120
122
124
113
115
62
64
66
68
70
72
74
76
78
80
82
84
N

although use of the word path here does not imply that only one unique capture sequence is allowed. One possible r-process path is indicated in Figure 1.2 and typically involves nuclides some 10 or more neutrons richer than the valley of beta stability. It is only after the neutron flux ceases that the nuclei beta decay back to the valley of beta stability. In Figure 1.3 this is indicated by the diagonal lines terminating at the first stable nuclide encountered. Note that, as a result of this, nuclei such as ^{124}Te and ^{130}Xe cannot be produced by the r-process because they are shielded from the beta decay of the r-process path by ^{124}Sn and ^{130}Te, respectively. Such nuclei are called s-only nuclei.

The proton rich nuclei to the left of the valley of beta stability cannot be produced by either the r- or the s-process. Another process, the p-process, a proton capture or neutron removal process, is invoked to explain their abundances (Arnett 1973 discusses the p-process briefly in reference to explosive nucleosynthesis). However, since these isotopes are much less abundant (generally 1-2 orders of magnitude) than s- and r-process isotopes, we will ignore contributions due to the p-process in what follows.

The determination of the abundances resulting from the s-process involves knowledge of the neutron capture cross sections of all nuclei along the s-process path. In the s-process, $\sigma_A N_A$, where N_A is the s-process abundance of a nuclide along the path with mass number A and neutron capture cross section σ_A, is a smoothly varying function of A, and, at least locally, the relative abundances of nuclides are inversely proportional to their neutron capture cross sections. Nuclei having a magic number of neutrons (and to a lesser extent a magic number of protons) have small neutron capture cross sections and therefore large s-process abundances. This is the case for ^{138}Ba which has a magic number of neutrons and also for $_{50}$Sn which has a magic number of protons. The validity of the s-process model can be tested by examining its

ability to reproduce the known abundances of the s-only isotopes. Results of Käppeler *et al.* (1982), for example, show that it is able to do this quite well with the correct choice of neutron exposure values, within the uncertainties in the measured cross sections and abundances.

The situation for the r-process is not as well established. No site responsible for r-process synthesis has as yet been agreed upon, although attempts have been made to place limits on the temperature and density of the synthesis region (e.g. Norman and Schramm 1979) both of which affect the location of the r-process path. The problem is further complicated by the need for neutron capture and beta decay rates for nuclei far from the valley of beta stability, the large majority of which have never been synthesized in the laboratory. The necessary information is obtained by extrapolation using various nuclear models with order of magnitude differences between beta decay rates from different models. Nevertheless, the r-process is similar to the s-process in that the production of neutron magic number nuclei along its path is favored because their longer decay times result in a buildup at these magic numbers. However, because the r-process path is displaced from the valley of beta stability during the neutron exposure, the subsequent beta decay results in a shifting of the r-process peaks to lower atomic numbers than those of the s-process, as can be deduced from an examination of Figure 1.2. The actual amount of the shift depends on the location assumed for the r-process which in turn is a function of neutron density, ambient temperature, and beta decay rates (see e.g. Norman and Schramm 1979, Schramm 1973, and Cowan *et al.* 1983).

The results of r-process calculations can be compared with the "r-only" isotopes (although the existence of r-only isotopes may be only an approximation if the s-process occurs in flashes, see Cameron 1982a). What is usually done however, is to decompose a given abundance distribution into r- and s-process contributions by subtracting the s-process

theory results from the full distribution. This is done by matching the s-process model to the s-only isotopes and then using the $\sigma_A N_A$ curve to determine the s-process contribution to the mixed isotopes. Figure 1.4 shows a decomposition of the solar system abundances in the Sn-Ce region into r and s process contributions. As explained in more detail in Chapter 4, this was derived using the s-process of Käppeler *et al.* (1982) and subtracting it from the solar system abundances of Anders and Ebihara (1982) on an isotope by isotope basis. Other decompositions, such as Cameron 1982a, differ in details but the general structure remains similar. The main features to note here are that, for the s-process contribution, $_{50}$Sn and $_{56}$Ba, the magic number nuclei, are significantly more abundant than $_{52}$Te and $_{54}$Xe. For the r-process, the situation is reversed with Te and Xe being the dominant elements. Additionally, $_{58}$Ce can be seen to be primarily an s-process element. These rather gross differences make this region a sensitive indicator of the relative amount of r- and s-process material present.

Early measurements of the ultra-heavy cosmic rays in a higher charge range indicated the presence of an r-process contribution. These experiments were primarily detectors of the passive type consisting of large areas of plastic track detector and/or photographic emulsion flown on balloons and later recovered. Charge identification was made by examining the damage trails left by the particle where it penetrated the material. (The ultra-heavy component of the cosmic rays was first detected by means of "fossil" tracks in meteorites (Fleischer *et al.* 1967)). The need for hand scanning of the detector material resulted in attention being focused on the high charge, rarer nuclei for which the detection efficiencies were near unity. The s-process is unable to produce elements heavier than $^{209}_{83}$Bi because of the lack of stable nuclei between $_{83}$Bi and $_{90}$Th. Therefore, detection of any nuclei with charge greater than $_{83}$Bi, in particular the actinides $_{90}$Th and $_{92}$U, would be

Figure 1.4

A decomposition of the solar system material into r- and s-process contributions using the solar system abundances of Anders and Ebihara (1982) and the s-process of Käppeler *et al.* (1982) (See Chapter 4). The solar system abundance of $_{14}$Si is defined to be 10^6.

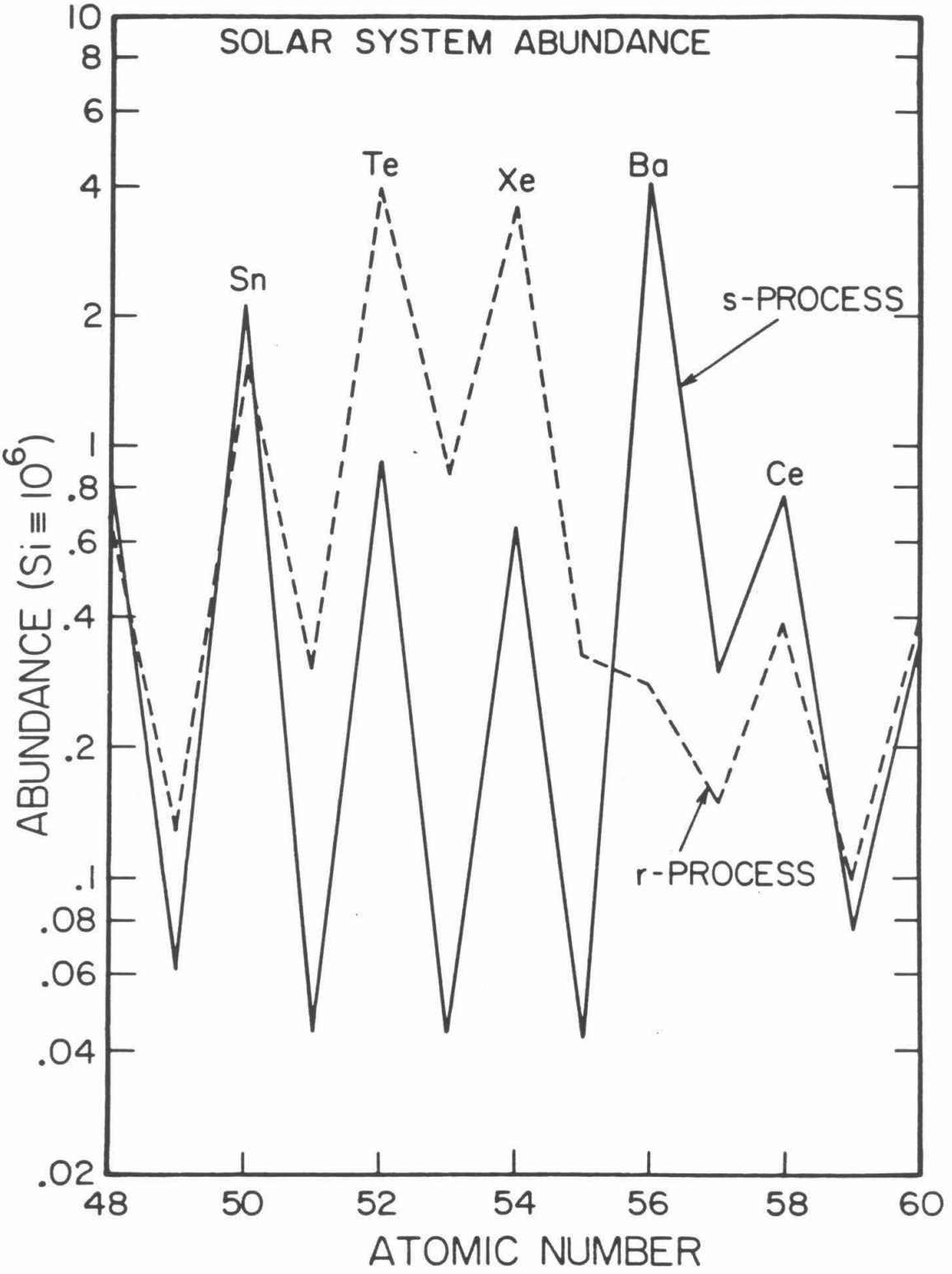
SOLAR SYSTEM ABUNDANCE
ABUNDANCE (Si ≡ 10^6)
ATOMIC NUMBER
10
8
6
4
2
1
.8
.6
.4
.2
.1
.08
.06
.04
.02
48
50
52
54
56
58
60
Sn
Te
Xe
Ba
Ce
s-PROCESS
r-PROCESS

evidence of r-process contributions. Several such particles were reported both in early balloon results (Fowler 1977 gives a brief review) and in measurements made from long term exposures of Lexar. on board Skylab (Shirk and Price 1978). However, the charge resolution and/or exposures were such that only element groups, and not individual charges, could be studied.

Electronic detectors, with their ability to process greater amounts of data and their promising charge resolution, were used to study the region just above iron (Israel *et al.* 1979). The results agreed better with a solar system mixture of r- and s-process material than with either component separately. However, because of the combination of small instrument geometry and short exposure times on balloons, statistics were insufficient to measure abundances above charge 40. Only with the advent of the long exposure times available on satellites could the rarer elements, such as Sn and Ba, be studied. Results have recently become available from two electronic satellite experiments to detect the ultra-heavy cosmic rays: the University of Bristol experiment on the Ariel VI satellite and the Heavy Nuclei Experiment on the HEAO-3 satellite.

This thesis will report on measurements of the abundances of the even charge elements in the region from $_{50}$Sn to $_{58}$Ce based on a first study of the data from 440 days of operation of the HEAO-3 Heavy Nuclei Experiment. These results are inconsistent with a pure r-process source but do not rule out the presence a solar system type mixture and are therefore consistent with measurements made by the same instrument in the charge range $26 \leq Z \leq 40$ (Binns *et al.* 1981b) and in the actinide region (Binns *et al* 1982).

II. THE INSTRUMENT

The Heavy Nuclei Experiment on the third High Energy Astronomy Observatory (HEAO-3) satellite was designed to measure the elemental composition of the ultra-heavy component of the cosmic radiation. The experiment was the result of a collaboration of three research institutions: the California Institute of Technology, Washington University at St. Louis, and the University of Minnesota at Minneapolis. A description of the instrument, its electronics, and its design considerations can be found in Binns *et al.* (1981a). Here I will give a summary description of the instrument emphasizing those features which are relevant to the present results.

Because the flux of the ultra-heavy cosmic radiation is many orders of magnitude below that of the more abundant nuclei of carbon, oxygen, and iron, any instrument designed to measure its elemental composition with reasonable statistical accuracy must, of necessity, have a large collecting power (geometry factor) and/or long exposure times. As a result, one of the most striking characteristics of the Heavy Nuclei Experiment instrument is its size. Whereas most cosmic ray detectors designed for use on spacecraft to measure abundances in the lower charge ranges have areas in the neighborhood of 500 mm^2 and geometry factors of less than or equal to 1 cm^2 sr, this experiment has an area of about 2 m^2 and a total geometry factor of 59,000 cm^2 sr.

The determination of the charge of a particle incident on the detector is by means of the dE/dx-Cerenkov technique. In this method the particle passes through both an ionization chamber, which measures the amount of energy deposited in the detector through interactions with atomic electrons, and a Cerenkov counter, which measures the amount of Cerenkov light emitted as the particle penetrates the radiator at a

velocity greater than that of light in the radiator material. The response of both of these detectors is a function of the speed of the particle (divided by the speed of light), β, and its charge, Z. The ionization signal, I, can be written approximately as (Janni 1966)

$$I \propto \frac{Z^2}{\beta^2}\left\{\ln\gamma^2\beta^2 - \beta^2 + \kappa\right\} \tag{2.1}$$

while for the Cerenkov signal, C,

$$C \propto Z^2\left\{1 - \frac{1}{n^2\beta^2}\right\} \tag{2.2}$$

where $\gamma = (1 - \beta^2)^{-\frac{1}{2}}$, κ is approximately a constant, and n is the index of refraction of the Cerenkov radiator material. Since the cosmic rays have a spectrum of incident energies and charges, both of these measurements are, in the absence of other information, necessary for the determination of the particle's charge.

Figure 2.1 is plot of the square root of the ionization signal per unit pathlength, ZI, versus the square root of the Cerenkov signal per unit pathlength, ZC. Shown on this plot is a family of curves representing the response of the HEAO instrument to the elements with even charge in the iron region. Each curve represents the response to a different charge with distance along the curve parametrized by the particle energy. The minimum in ZI for each curve is at approximately 2 GeV/nucleon with the increase in ZI at high energies, the relativistic rise, the result of the logarithmic term in (2.1). For both the Cerenkov and the ionization response we have used the the Z-squared scaling shown above and in the lower energy regime slowing down of the particle within the detector has been taken into account (Krombel 1980). One should note that for high enough energies the Cerenkov response alone is sufficient to determine the charge.

Figure 2.1

A plot of the square root of the ion chamber signal per unit pathlength, ZI, versus the square root of the Cerenkov chamber signal per unit pathlength, ZC. The curves on the plot show the expected response of the Heavy Nuclei Experiment to the even charge elements from $_{14}$Si to $_{34}$Se. The normalization of ZC is such that a $\beta \sim 1$ charge 26 (iron) particle will result in a ZC of 26. ZI is normalized so that its minimum value for iron is 26.

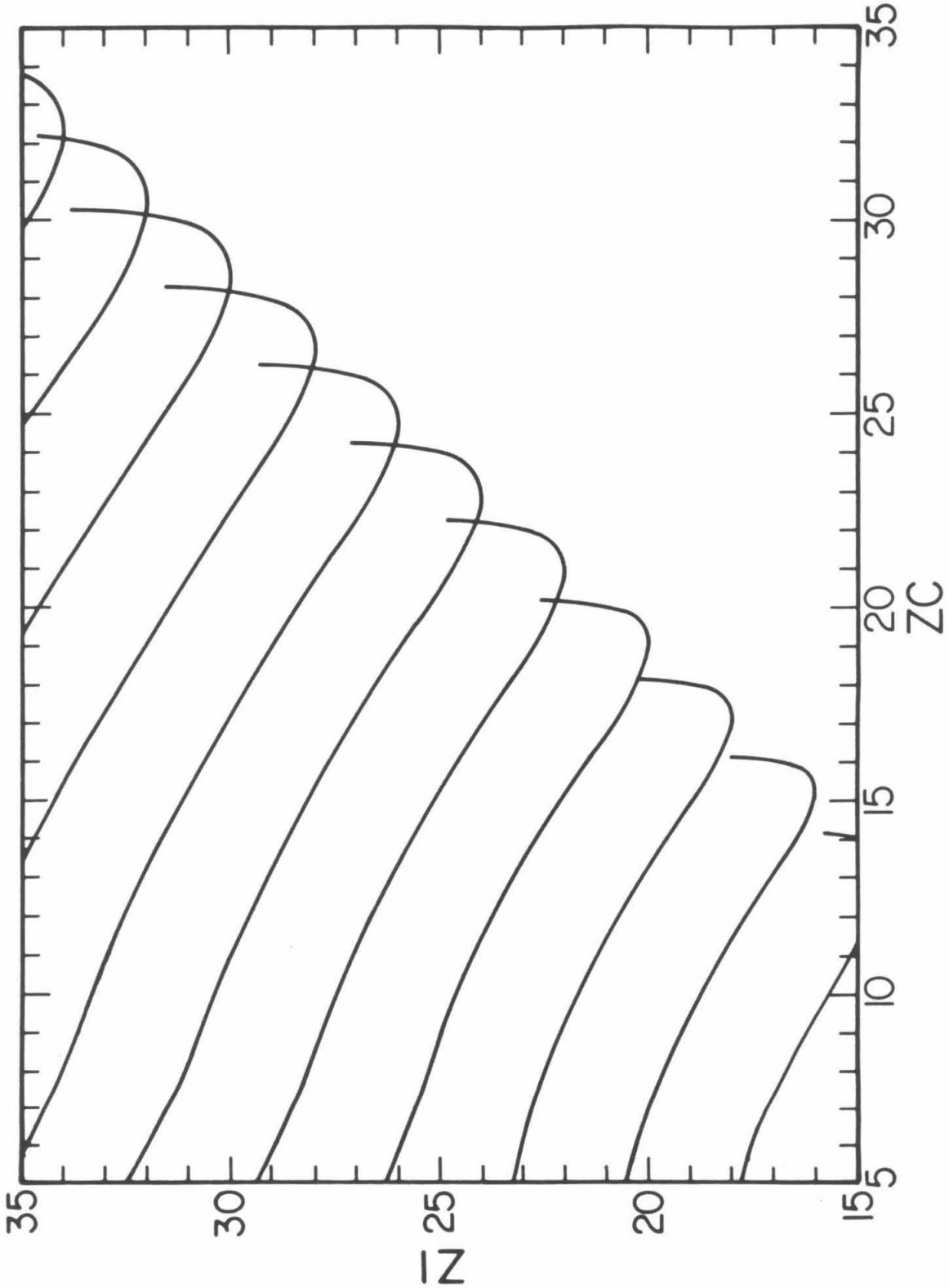
35
30
25
20
15
ZI
5
10
15
20
25
30
35
ZC

Figure 2.2 is a cross section view of the experiment. The instrument consists of six parallel plate ionization chambers (IC), four pairs of multiwire ionization hodoscopes (HODO), and a dual radiator Cerenkov detector (RAD1 and RAD2). The arrangement is symmetric about the detector midplane (the X-Z plane) with three ion chambers, two sets of hodoscope planes, and a Cerenkov radiator on either side. Each "half" of the instrument consists of a sealed pressure vessel containing the three ion chambers and two hodoscopes. The Cerenkov radiator is mounted on the outside of the pressure vessel and the module so formed is attached to its mate with the Cerenkov radiators facing each other. The radiators do not touch but are separated by a vacuum and the Cerenkov light box is formed by enclosing this volume in a light-tight seal. Both radiators are viewed by the same set of eight photomultiplier tubes. The instrument and each of the modules has the shape of a rectangular parallelepiped which was dictated by the satellite geometry.

Each pressure vessel is a sealed unit in order to obviate the necessity for an external onboard gas supply. P-10 gas has been used, which is a mixture of 90% argon and 10% methane with a trace (approx 0.5%) of helium added for leak detection. The gas pressure is a nominal 838 torr at 20° C. The instrument windows consist of aluminum honeycomb with a thickness of 8.9 cm and a mean areal density of 1.2 g cm^{-2}. Aluminum honeycomb was chosen for the window material because it combines the features of high strength and low density thereby minimizing the amount of fragmentation which occurs as a particle penetrates the instrument. The ultra-heavy cosmic rays are particularly sensitive to this because of their small fragmentation pathlengths.

The ionization chambers are of dual-gap design with the anode mounted midway between the two cathodes. The cathodes are shared by adjacent ion chambers and/or the adjacent hodoscope planes. The electrodes are made of aluminum screenwire and the ion chambers have an

Figure 2.2

A cross sectional view of the Heavy Nuclei Experiment on HEAO-3 showing the ion chambers (IC), the Cerenkov radiator (RAD 1 and RAD 2), and the hodoscope planes (HODO). The aluminum honeycomb windows are suggested by the dashed lines showing the division of the instrument into two separate pressure vessels.

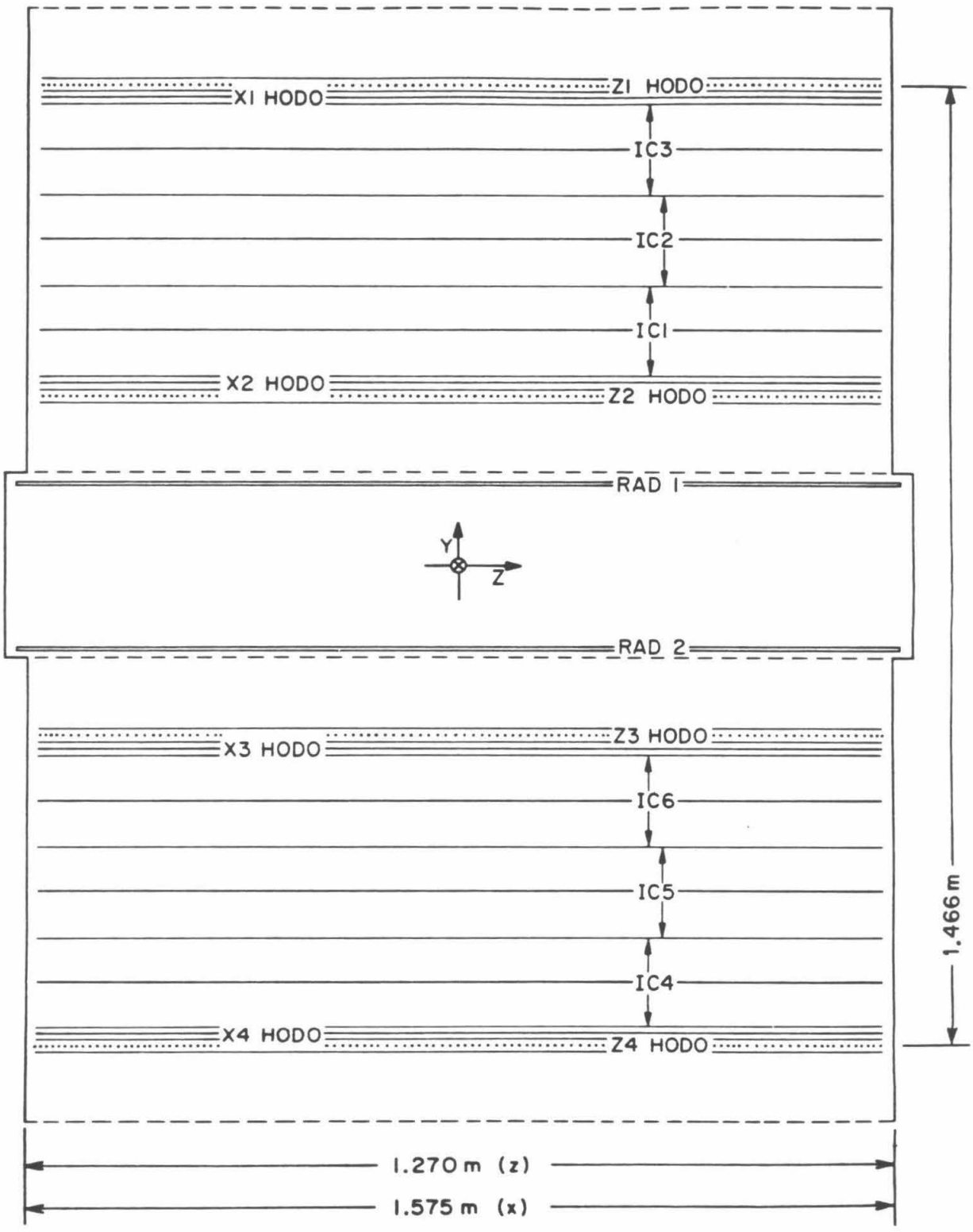
X1 HODO
Z1 HODO
IC3
IC2
IC1
X2 HODO
Z2 HODO
RAD 1
Y
Z
RAD 2
X3 HODO
Z3 HODO
IC6
IC5
IC4
X4 HODO
Z4 HODO
1.466 m
1.270 m (z)
1.575 m (x)

anode to cathode spacing of 6.9 cm and are operated at -1000 V. This choice of operating voltage was made to minimize both electron collection losses and variation of electron drift velocity with small variations in pressure or voltage as detailed in Binns *et al.* (1981a). Each ion chamber is separately pulse height analyzed and all six pulse heights recorded for each accepted particle.

The trajectory of the incident particle is determined by the use of discrete wire ionization hodoscopes. Each hodoscope layer consists of a an anode composed of 0.025 cm diameter parallel stainless steel wires with a center to center spacing of 1 cm. The anode layer is midway between two screen wire cathodes with an anode to cathode spacing again of 1 cm. The operating voltage is -1000 V and the diameter of the wires is such that the hodoscopes are operated in the ionization mode and no gas amplification takes place. Each anode wire has its own charge sensitive preamplifier and discriminator. For each event, the instrument records the discriminator state of up to 16 wires in each of the 8 hodoscope layers in the form of two address/patterns. The first address/pattern consists of the address of the first (lowest address) wire fired and the discriminator state of the subsequent 7 wires. The second pattern has the same format as the first and is used when more than 8 wires have fired.

The Cerenkov counter portion of the detector consists of two sheets of 0.47 cm thick Pilot 425 viewed by eight photomultiplier tubes. Each sheet has been sandblasted in order to improve uniformity of response and the face against the pressure vessel has been painted with white paint as has the interior of the light box. The two radiators are separated by a distance of 24.7 cm. The eight photomultiplier tubes are arranged in pairs with one pair at each corner of the rectangle forming the light box. Each photomultiplier tube is separately pulse height analyzed and the eight values are recorded for each event. The index of

refraction of the Pilot 425 for the wavelengths of interest is approximately 1.52 which corresponds to a threshold energy of approximately 300 MeV/amu.

The criteria for acceptance of an event for analysis, in the normal mode of operation, are triggering of one wire or more in both the X and Z planes in at least two of the four hodoscopes and the firing of at least two of the seven charge measuring detectors, i.e. the six ion chambers and the Cerenkov detector. These particular requirements were meant to ensure that one is able to make a trajectory determination for the event but do not ensure that the event has both a Cerenkov and an ion signal. A perfectly valid event could conceivably pass through two hodoscopes and miss both Cerenkov radiators (e.g. triggering the X1-Z1 HODO and the X2-Z2 HODO in Figure 2.2). One can still assign a charge to this kind of event, albeit with reduced confidence, using geomagnetic cutoff data to restrict the possible energy range. However all the events used in this analysis were required to have a Cerenkov signal.

The minimum charge particle needed to trigger the hodoscope depends on the the angle of incidence of the particle and its position with respect to the anode wire. For the typical trajectory the path contributing to one anode wire is about 2 cm and the minimum charge particle that will fire the discriminator on that wire is about 11.5 charge units (all charges are in units of the proton charge). A vertical trajectory midway between two anodes, the worst case, has a path of 1 cm contributing to each anode and requires a particle with charge of approximately 16.2 to trigger either discriminator. The Cerenkov trigger, C2, consists of the "or" of two photomultiplier tubes not in the same corner of the instrument as shown in Figure 2.3. The discriminator for each photomultiplier tube is set at 16% of a perpendicular $\beta = 1$ charge 26 (iron) nucleus or the full signal of a perpendicular, $Z \sim 10$, $\beta = 1$ nucleus. The actual charge threshold is a function of incident angle because

Figure 2.3

A schematic drawing of the Cerenkov radiator layout showing placement and labeling of individual photomultiplier tubes along with the Cerenkov triggering criterion.

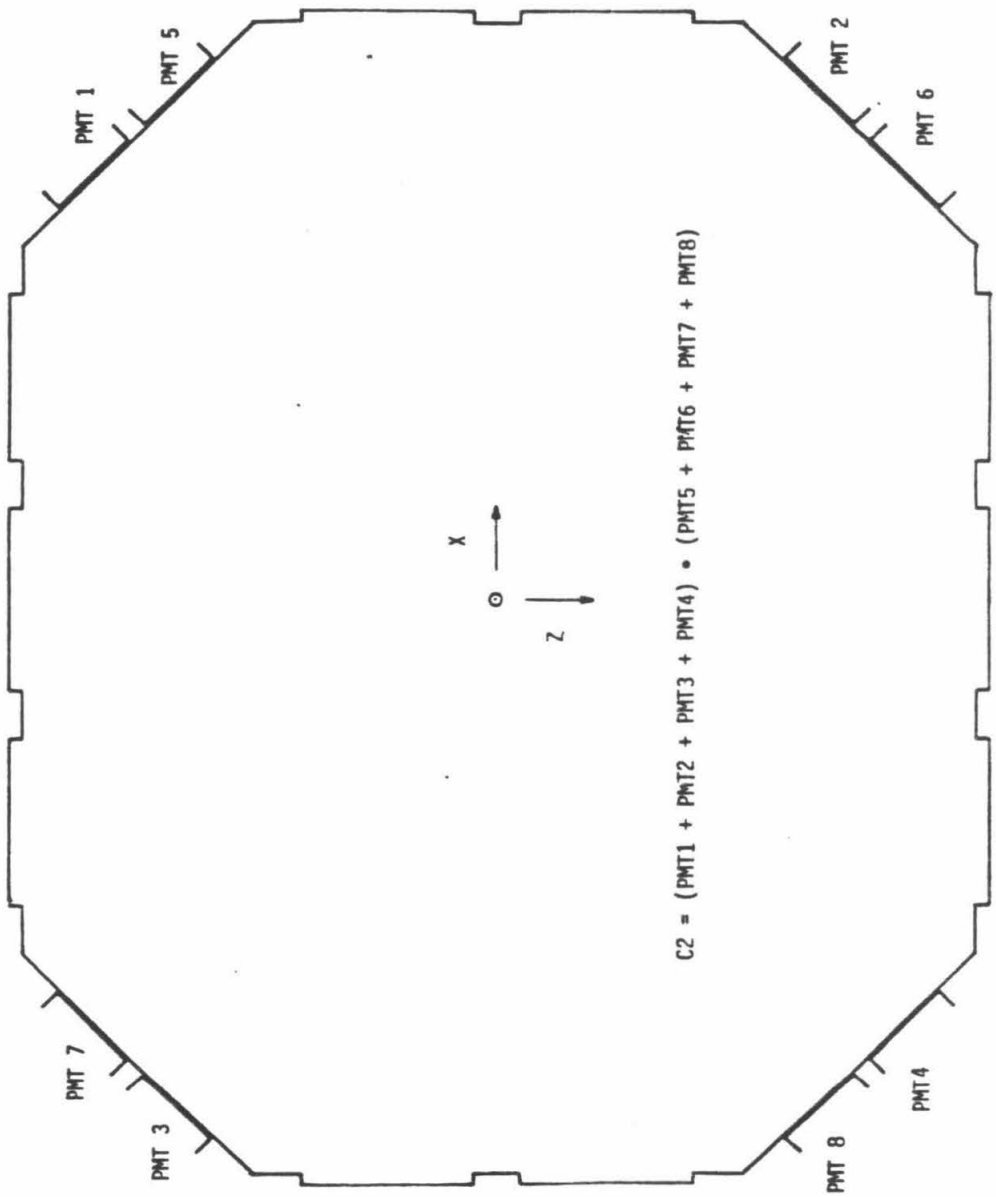
PMT 1
PMT 5
PMT 2
PMT 6
PMT 7
PMT 3
PMT 8
PMT4
X
Z
C2 = (PMT1 + PMT2 + PMT3 + PMT4) • (PMT5 + PMT6 + PMT7 + PMT8)

particles with a larger angle to the normal have, in general, a greater pathlength in the detector and hence a larger signal. The ion chambers each have three different discriminator levels: LLD, ILD, and HLD. These three levels are set to correspond to vertically incident charges 16.1, 33.3, and 43.7 respectively. The LLD is the trigger used for event analysis while the other discriminators are used for determining event "priority". The presence of a relatively large flux of iron nuclei results in a significant amount of dead time for non-priority events due to the data transmission rate of 128 events every 40.96 seconds. The priority system was instituted to ensure that the high charge events are recorded with essentially 100% efficiency by allowing a priority event to write over any non-priority event being held for transmission. An event is designated priority if any HLD fires or if any ILD and C2 fire. These ensure that any event with charge greater than 44 is recorded as well as any event with charge greater than 33 and an energy greater than about 350 MeV/nucleon.

Figure 2.4 is a schematic view of the satellite indicating the placement and configuration of the Heavy Nuclei Experiment. The instrument windows are exposed on either side of the spacecraft with the instrument itself oriented along the spacecraft's Y axis. The rather loose event acceptance criteria allow for the analysis of particles which did not enter through the windows. Such "sidewall" events have had to penetrate larger amounts of material than the window events, typically 2-3 g cm^{-2}, due to the satellite body and electronic packages mounted to the outside of the instrument. However, allowing such events to be analyzed results in approximately a threefold increase in our geometry factor over using window events exclusively.

The spacecraft was launched into a circular orbit with initial altitude of 496 km and an inclination of 43.6° on 1979 September 20. The usual mode of operation was for the spacecraft Z axis (the solar panel

Figure 2.4

A schematic view of the HEAO-3 satellite showing the placement of the Heavy Nuclei Experiment (Linder 1979). The spacecraft is normally oriented with its Z axis (and solar panels) pointed towards the sun. It spins about the Z axis with a 20 minute period.

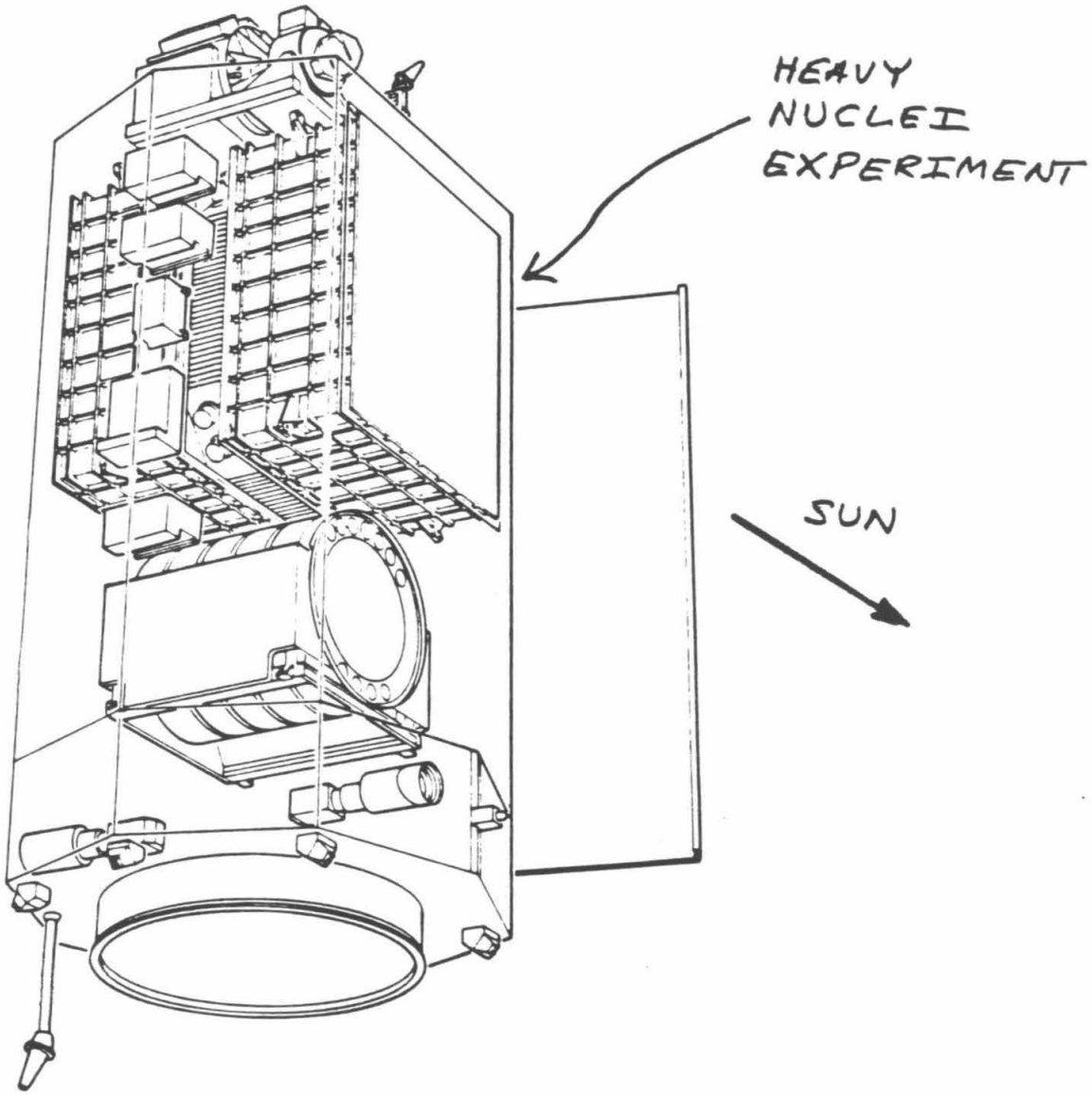
HEAVY
NUCLEI
EXPERIMENT
SUN

axis) to be pointed toward the sun with a rotation period of 20 min around this axis. As a result, the instrument does not have a fixed orientation with respect to the earth. To accommodate the other experiments on board, there were several periods when the Z axis was directed towards a point some 30° away from the sun ("offset scan" mode). Star sensors on the satellite allow for post-facto attitude determination to better than 0.5°.

The altitude and inclination of the orbit are such that the spacecraft will pass though a region of the geomagnetic field known as the South Atlantic Anomaly (SAA) during many of its orbits. The configuration of the geomagnetic field is such that a large flux of trapped protons are encountered here with the flux being high enough that the instrument response is severly degraded by accidental coincidences, possible baseline shifts, and other effects. As a result data taken during an SAA passage are extremely unreliable without special processing and are not used in this study.

The instrument operated until 1981 May 29 with the latter part of the mission characterized by a degradation in response in several of the ion chambers (for that time period, the ion chambers showing the degradation were not used in the present analysis). We report here on the results from approximately 440 days of operation. Appendix A lists the time periods used.

III. THE DATA

3.1. Overview

Because of the large variation in the flux of the ultra-heavy cosmic rays (a decrease of at least five orders of magnitude from iron to uranium) and the desire to establish a reference point in a previously investigated charge range, a large number of iron, and other lower charge nuclei, are present in the data telemetered back to earth from the Heavy Nuclei Experiment on the HEAO-3 satellite. Typically some 180,000 events per day were recorded by the instrument. The presence of such a large flux of particles allows for in-flight calibrations and mapping of instrument response. However, the sheer volume of data creates problems in data processing and handling, especially when we consider the amount of sorting that must be done to select out the less than 150 events in the charge range of interest here.

In order to facilitate analysis the data processing was divided into several stages, each more selective than the preceding. The first stage, or pass through the data, converts all events from their raw encoded form into one which is more easily interpreted. In the second pass, a high charge subset is selected from the output of the first pass and the charge estimates are further refined by more sophisticated processing. Events from this greatly reduced subset were classified on the basis of their probable energy and separated into categories of different expected charge resolution. The various categories were then examined using the technique of modulo 2 superposition of even element peaks to select those actually having the best resolution. Those selected were added together to yield the final results presented in Section 3.6. In this chapter, we will describe in more detail the processing steps outlined above.

3.2. First Pass Analysis

In the first pass at data analysis no attempt was made to be selective but instead as many events as possible were converted from their raw form, as telemetered from the satellite, into more physically meaningful quantities. This processing was done by the library generator program, LIBGEN (Garrard 1979a) which converted production (raw data) tapes, as received from Goddard Space Flight Center, into Library tapes. The data from the instrument fill one 2400 foot, 1600 BPI production tape per day of operation and each Library tape contains the analyzed data from one production tape.

The LIBGEN program is a rather extensive algorithm which does the following:

1. Converts the wire patterns from the instrument hodoscopes into trajectories using known dimensions for the wire and hodoscope spacings. This step results in the first major classification of particle types depending on the accuracy with which a trajectory can be constructed. A list is maintained of wires in each layer for which the firing rates have been determined to be excessively high or low based on examinations of daily rate data. This information is used to eliminate "missing" or "extra" wires from the hodoscope patterns. For those events which have patterns with no "missing" or "extra" wires in 2 or more hodoscope planes (in both the X and Z coordinates of that plane), the center of each pattern is used in a least squares fit to a straight line to obtain the particle trajectory. Those events having inconsistencies in the wire patterns which preclude construction of reliable trajectories are classified separately from the good trajectory events for future consideration.

2. Flags those events which have data quality or logic problems, i.e. parity or telemetry errors, nominally repeated events which do not match their predecessor, etc. Also flagged are those events for which trajectories were able to be constructed, but which still had trajectory inconsistencies such as more wires triggered than is consistent with the calculated trajectory, an ion chamber which is on the trajectory but which does not have a signal, a large χ^2 on the fitted trajectory, etc.

3. Converts raw ion chamber pulse heights, from the pseudo-logarithmic pulse height analyzers (PHA), to signal in femto-coulombs.

4. Converts the raw photomultiplier tube pulse heights, again from a pseudo-logarithmic PHA, into signal in volts.

5. Normalizes both ion and Cerenkov signals to signal per unit path-length using the trajectory information and measurements made prior to launch of the thickness of the Cerenkov radiators. Each radiator has its own thickness map which is used in the calculation.

6. Extracts and processes the satellite attitude and orbit data for each event which are necessary to relate the particle trajectory in the spacecraft frame to an external frame of reference.

7. Makes initial estimates of the particle's charge using Cerenkov and ion chamber data. These estimates are based on the fact that the ratio of the Cerenkov signal to the ion signal is, to first order, independent of particle charge with both being proportional to Z^2 in this approximation. Thus, referring to Figure 2.1, one can derive a charge independent function of ZC/ZI, using iron data, which will correct ZI by an amount determined by ZC/ZI and allow an energy independent estimate of the charge to be made (Israel 1980 and private communication). Such a function can be applied to the

average ion chamber signal from either module. If either of these estimates is greater than 30.5, the event is flagged as a "high charge" event. For 54% of the time period reported on here, ZC alone was also used to select high charge events. Because of subsequent ion chamber and Cerenkov agreement criteria and the distance of the threshold from the present charge region, this distinction is unimportant for this analysis.

3.3. High Charge Subset

The first pass does not decrease the volume of the data but does do a preliminary classification and processing of the events. In this next pass only those events which had some indication of having a charge greater than 30.5, i.e. the "high charge" events mentioned above, were retained. In addition, more refined processing was done to obtain better charge estimates.

Because of the large surface area of the detector, it was necessary to make corrections for nonuniformities in detector response over the active area of the instrument. For this purpose the large flux of iron nuclei was useful in deriving a two dimensional response map for each ion chamber and for the Cerenkov detector. In mapping the ion chambers, variations in the ionization signal caused by differences in particle energies were reduced by choosing a subset of the iron data in the minimum ionizing region. All the particles in this subset should have the same ionization signal and were binned according to their position within the chamber under study. The resulting maps are uniform in the central area (more than 44 cm from any wall) with variations of less than 0.1%. The response falls off linearly to 0.98 of the central value as one approaches to within 8 cm of a wall. For events used in this analysis, we ignore all chambers for which the particle trajectory indicates passage closer than 8 cm to a wall within that chamber. These

maps were constructed at Washington University and each ion chamber has its own position dependent correction based on its response map. The in-flight iron data were also used to normalize the chambers to one another.

The Cerenkov chamber map, on the other hand, has a much larger variation over its surface. Response maps were made for each individual photomultiplier tube and for the mean of all eight tubes. Only the eight tube map was used in the response corrections, however, with the single tube maps being used solely for the determination of consistency criteria (see below). The largest light collection non-uniformities are the result of "hot spots" in front of each PMT. In the central region of the eight tube map, more than 25 cm from any PMT, the typical gradients are less than 0.2%/cm with variations of about 10% over the entire central region. The corrections in front of a PMT however can be as large as 0.72 with gradients of 1.5 %/cm. The iron data were again used to construct the Cerenkov maps. This work was done at the University of Minnesota.

In addition to the mapping corrections, there was a correction applied for time variations in response. Observation of the iron peak position showed that the ion chamber time variation was less than 0.2%. The individual PMTs however showed a variation which correlated well with temperature and was of the order of 0.7 %/°C. However, the gain variations were slow enough, usually well under 0.5 %/day, that sufficient numbers of iron particles were collected to allow corrections to be made on a daily basis, to each PMT, to 0.15 %. Both the ion chamber and the photomultiplier tube response were monitored on a daily basis for the duration of the flight. In addition, corrections were made for differences in the individual PMT gains so that all tubes were weighted equally in the final charge determination.

Both the mapping and the corrections for daily variations in the PMTs were done in this second pass. Additionally, a more sophisticated algorithm was applied to the particles for which the LIBGEN program was unable to determine a trajectory in order to assign, by deletion of bad hodoscope planes etc., a trajectory and a charge to these events. However, neither these events nor those flagged as having residual trajectory inconsistencies were used in the data set presented here. Eliminated before the next analysis stage were those events previously flagged as having data quality or logic problems. In addition, preliminary consistency checks were made using the multiparameter nature of the instrument in order to remove obviously anomalous events before further processing.

The first of these selections was based on agreement between the measurements made by the individual photomultiplier tubes for a given event. Figure 3.1 exhibits histograms, for the high charge data set, of the ratio of single tube to mean of all eight both for tubes which are in the same quadrant as the particle and for tubes which are in the opposite X-half of the Cerenkov box. No single tube mapping has been done for this selection and the width of the distributions is dominated by the mapping variations. The difference in the peak location between the two histograms indicates that the near quadrant tubes have a signal that is some 1.3 times the average while the distant tubes have only 75% of the average signal. By using the individual tube maps, limits on the allowable deviation of a single tube from the mean of eight tubes was determined. The agreement criteria were based on the location of the tube with respect to the particle's position at the midplane of the Cerenkov box. Only a gross determination of location was used: whether the tube was in the same quadrant (or half) of the radiator as the particle. This selection helps to eliminate errors in the Cerenkov charge due to single tube errors. By far the most common tube error is the presence of one

Figure 3.1

Histograms of the ratio of individual Cerenkov photomultiplier tubes to the mean of all eight tubes. The eight tube average has been corrected for position variations in response. The individual tube values have not. The upper histogram is for tubes determined to be in the same quadrant as the particle based on its position at the center of the Cerenkov box (the "closest" tubes). The lower histogram is the same for tubes in the opposite X-half of the Cerenkov box (the "farthest" tubes). Also indicated are the agreement limits used in the consistency selections. "Single tube hits" have been eliminated from these plots.

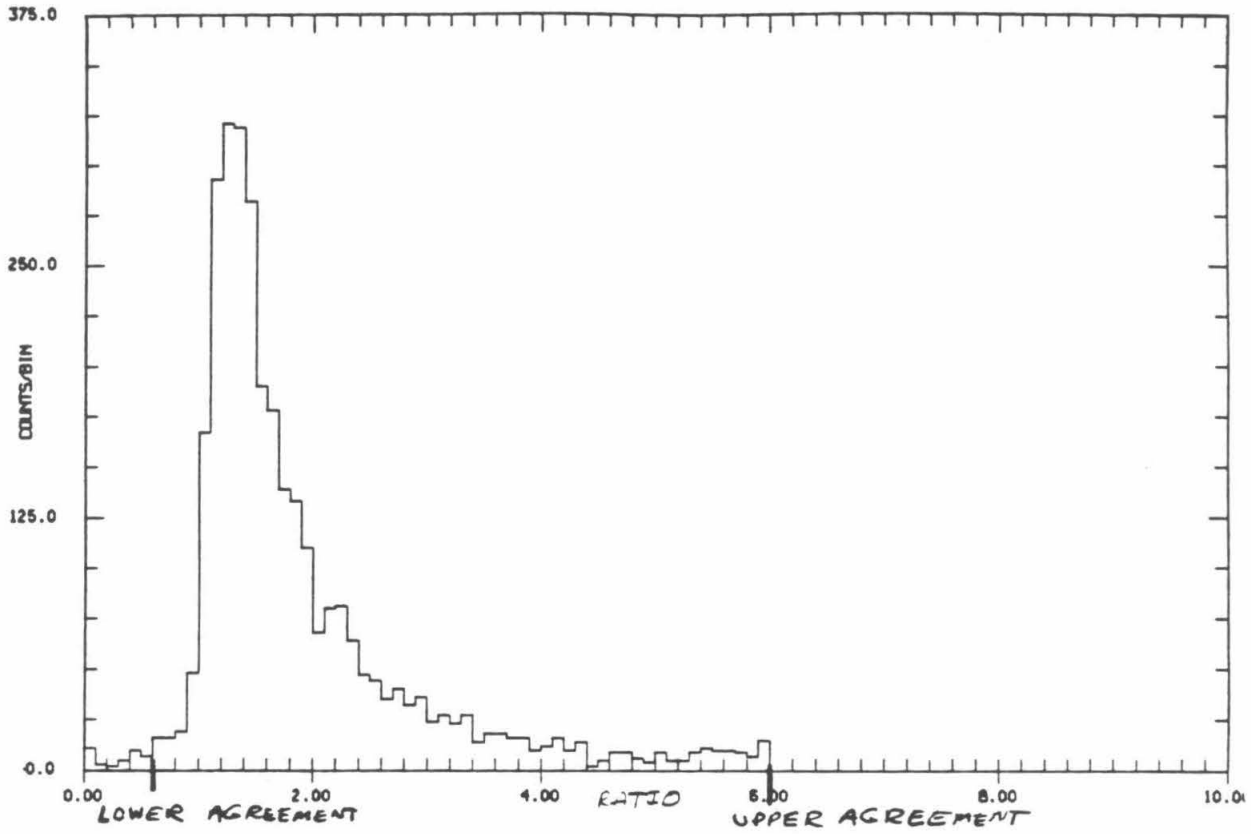
375.0
250.0
125.0
0.0
COUNTS/BIN
0.00
2.00
4.00
6.00
8.00
10.0
RATIO
LOWER AGREEMENT
UPPER AGREEMENT

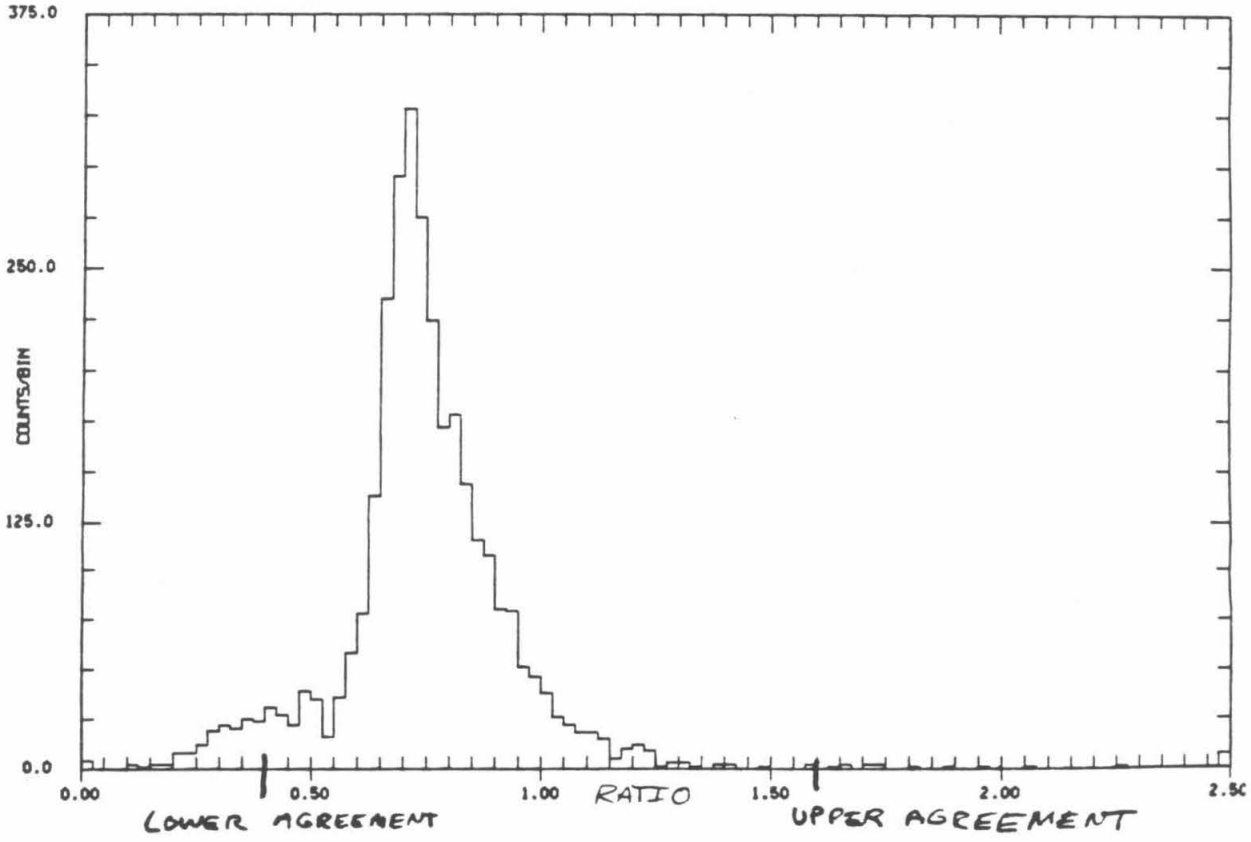
375.0
250.0
125.0
0.0
COUNTS/BIN
0.00
0.50
1.00
1.50
2.00
2.5
RATIO
LOWER AGREEMENT
UPPER AGREEMENT

tube which dominates the sum of eight. That these events are the result of the particle actually hitting the photomultiplier tube in question is borne out by the particle trajectory which almost always indicates that it passed through the Cerenkov box in a corner. These spurious "high charge" events constitute some 88% of the high charge data set. The "single tube hits" have been removed from Figure 3.1 by eliminating those events having a ratio greater than 6.0. (For the case where one tube dominates the average, we would expect its ratio to the average to be approximately 8.) The location of the consistency cuts are indicated on the histograms. The accepted values were between 0.6 and 6.0 for the same quadrant tubes, 0.5 and 2.5 for same X-half but not same quadrant, and 0.4 and 1.6 for opposite X-half tubes (Israel 1979).

A second selection was made on the agreement between ion chambers within a module. The amount of matter between the chambers in one module is small enough (<0.1 g cm^{-2}) that there should be no appreciable energy loss from one chamber to the next. Figure 3.2 shows a histogram of the dispersion between chambers within a single module (the module containing ion chambers 1, 2, and 3 in Figure 2.2). The histogram includes both two and three chamber events. The quantity plotted is

$$FDZ = \frac{1}{2} \frac{\frac{1}{n}\sum_{i=1}^{3} |I_i - I_{avg}|}{Z_{est}} \qquad (3.1)$$

where I_i is the signal from ion chamber i, I_{avg} is the mean ion signal within that module, Z_{est} is the charge estimate (of the type discussed in section 3.2) based on the module, and the sum over i (and I_{avg}) includes only the n ion chambers in the module with a valid signal. This value, in the absence of correlated errors between chambers, corresponds to the uncertainty in the charge estimate expected from using the ion

Figure 3.2

Histogram showing the degree of agreement between ion chambers within a single module. The horizontal axis is a measure of the dispersion between chambers, in charge units (see text). Also shown is the consistency selection used.

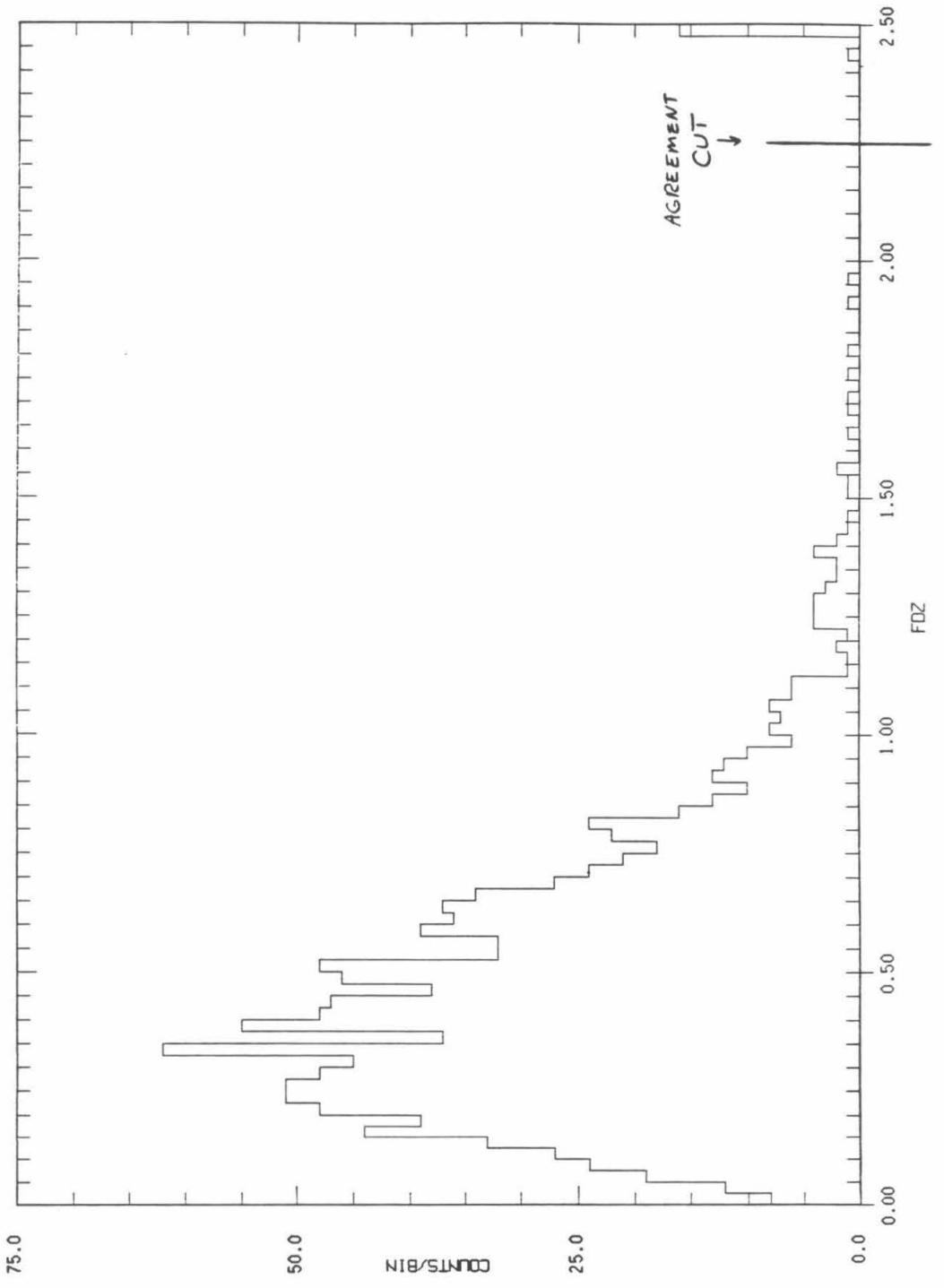
AGREEMENT
CUT
COUNTS/BIN
FDZ
0.0
25.0
50.0
75.0
0.00
0.50
1.00
1.50
2.00
2.50

chambers since, because of the Z-squared dependence of the signal, I, $I \propto Z^2$ and thus $2\frac{\delta Z}{Z} = \frac{\delta I}{I}$. The amount of dispersion indicated by the mode of this plot however, approximately 0.3 charge units (measured in terms of the proton charge), is lower than would be expected on the basis of the observed ion chamber charge resolution, and is probably the result of correlations between chambers within a module. In order to eliminate only those events having obvious ion chamber inconsistencies, we required FDZ < 2.25 charge units.

As mentioned in the previous chapter, events which occurred during passage through the South Atlantic Anomaly (SAA) were also excluded from consideration. The location of the SAA was determined both on the basis of orbital position and the "singles" rates in the ion chambers, i.e. the number of firings of the ion chambers as indicated by the number of signals above the LLD, whether or not the event met the coincidence requirement.

3.4. Energy Selections

For this first study, because it has better resolution, we have used the Cerenkov chamber alone as the determinant of charge with the ion chamber information used only for consistency checks and in the classification scheme. As a result, it is necessary to accept only those particles having energy great enough that the Cerenkov response has reached its plateau. This can be done by using the earth's magnetic field as an rigidity filter (Rigidity, R, being defined as $\frac{pc}{Ze}$ where p is the particle momentum, c is the speed of light, and Z is the charge of the particle in units of the proton charge, e). In the earth's field, particles arriving from any given direction must have a rigidity greater than some critical rigidity which is a function of the direction of arrival and position of observation in the field. The theory of motion in the earth's

magnetic field was first developed by Störmer (e.g., Störmer, 1955) by modeling the geomagnetic field as a dipole. The axial symmetry of the dipole results in a constant of the motion which allows derivation of the following equation for the Störmer cutoff rigidity, R_c, as a function of observation position in the dipole and direction of viewing.

$$R_c = \frac{M}{r^2}\left[\frac{1 - \left(1 - \cos\gamma \cos^3\lambda\right)^{1/2}}{\cos\gamma \cos\lambda}\right]^2 \qquad (3.2)$$

where M is the magnitude of the dipole moment, r is the radius from the center of the dipole, γ is the angle that the particle's trajectory makes with the west (a particle traveling due west has a γ of zero) and λ is the latitude of the observation point. Although the geomagnetic field is not truly a dipole and the determination of the exact R_c involves complicated calculations for tracing the particle's assumed trajectory backwards, we can still define a local magnetic west and local magnetic latitude using the value of the magnetic **B** field and the McIlwain L value at the point in question. Then using the dipole approximations (Roederer 1970) that

$$B^2 = \frac{M^2}{r^6}\left(4 - 3\cos^2\lambda\right) \qquad (3.3)$$

and

$$L = \frac{\cos^2\lambda}{r/r_e} \qquad (3.4)$$

(with r_e the radius of the earth) we can eliminate λ and estimate the cutoff rigidity for the direction of arrival of the particle (Garrard 1979b). The values of **B** and L used were calculated at Goddard Space Flight Center from standard reference geomagnetic fields which approximate the earth's actual field by a spherical harmonic expansion. Figure 3.3 is

a plot of ZI versus ZC for data in the sub-iron region both with and without a rigidity selection applied. It can be seen that, although the theory used is an approximation, the rigidity cut does succeed in excluding the majority of the low energy particles. A cutoff rigidity of 8 GV was used for this analysis. For $_{50}$Sn (typical atomic mass 120 amu), this corresponds to an energy of 2.53 GeV/nucleon and a Cerenkov signal which is 94% of the $\beta = 1$ value.

The determination of a unique R_c involves knowledge not only of the particle trajectory, but also of the direction of motion along the trajectory. Changing γ by 180° changes R_c. Since the Heavy Nuclei Experiment does not have a device for determining direction of motion along the trajectory, two possible R_c are assigned to each event, corresponding to the two possible directions. For some of these particles, only one of these two directions is permissible because, if traced backwards in the other direction, the trajectory intersects the earth. Determination of these earth shadowing directions was done empirically by using data provided by the Danish-French cosmic ray isotope experiment also on the HEAO-3 satellite (Lund and Westergaard, private communication; Garrard and Ennis 1980a & b). Having a time of flight device, they were able to map out forbidden directions in the sky. In practice, use of the forbidden directions is necessary for only 12% of the high rigidity data selected for use in the Sn-Ce region. The remainder of the events have both R_c greater than 8 GV.

Since the high cutoff particles constitute only 40% of the data, in order to increase the number of events in the sample we have also analyzed particles which were chosen to be high energy on the basis of their ratio of ZC to ZI. Figure 3.4 is a crossplot of ZC/ZI versus ZC for two days of selected iron data which illustrates the rationale behind this selection. The curves in Figure 3.4 are the same as the element tracks seen in Figures 3.3 and 2.2 and, again, distance along the curve can be

Figure 3.3

Crossplots of the ion chamber charge estimate versus the Cerenkov charge estimate for two days of data in the iron and sub-iron charge region. Only events with two estimates of the charge based on the ion chambers, i.e. two module events, which agree to within approximately 7.5% were used. The upper plot has only particles with rigidities above 8 GV, chosen using the selection in the text. The lower has no rigidity selection. (The lack of events at ZC<7 is an artifact of the selection program.)

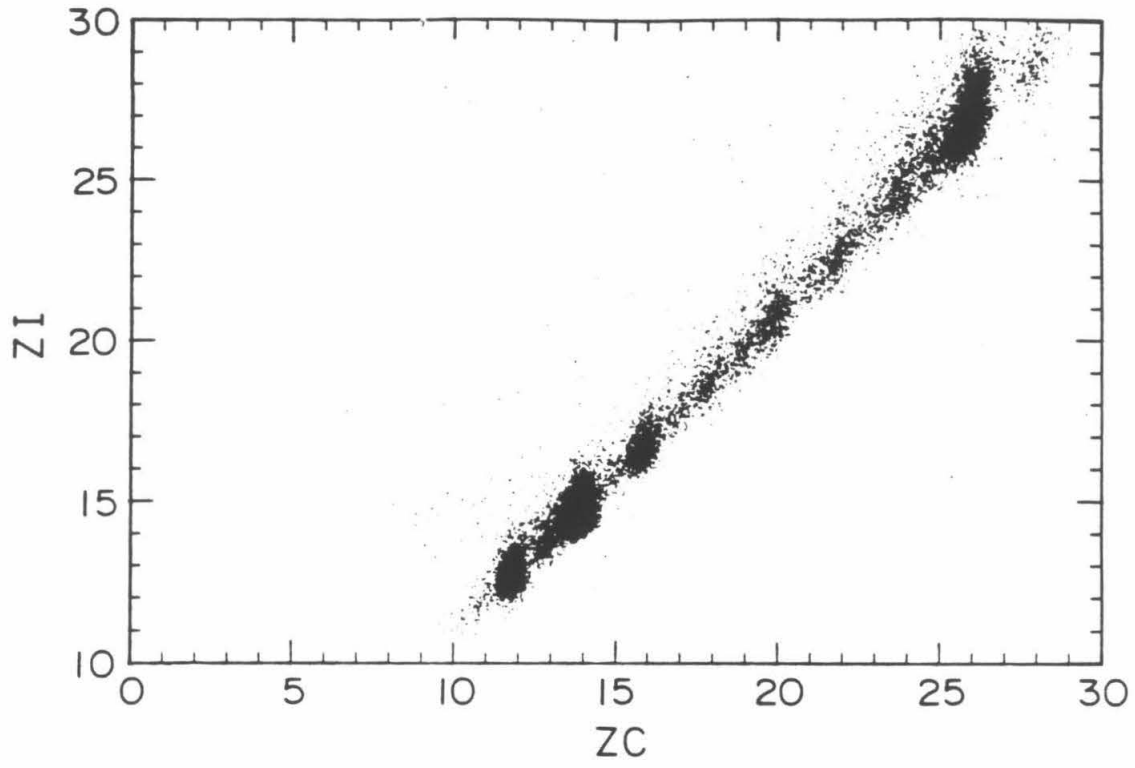
30
25
20
15
10
ZI
0
5
10
15
20
25
30
ZC

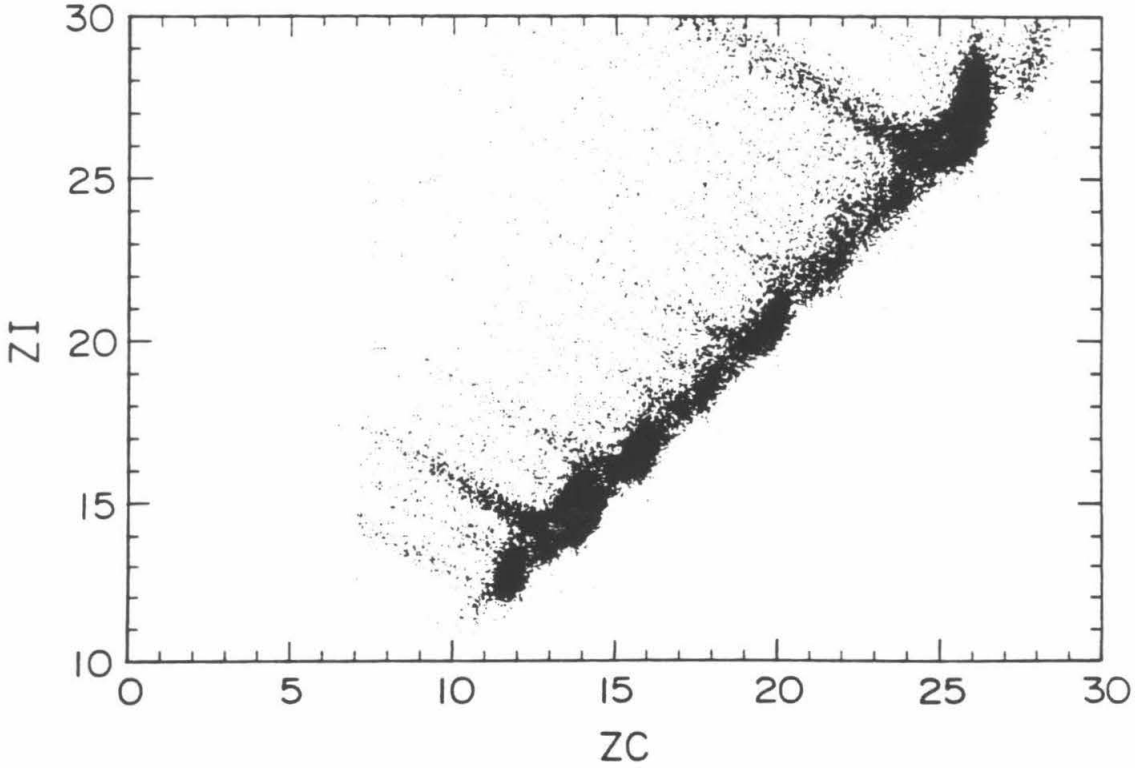
30
25
20
15
10
ZI
0
5
10
15
20
25
30
ZC

Figure 3.4

Crossplot of the ratio of ZC to ZI as a function of ZC for two days of iron data. This plot illustrates how the selection on ZC/ZI (see text) chooses only the "tip" of the response curve enabling the use of ZC as a valid charge estimate. Note that silicon (Z=14) may be affected by threshold effects.

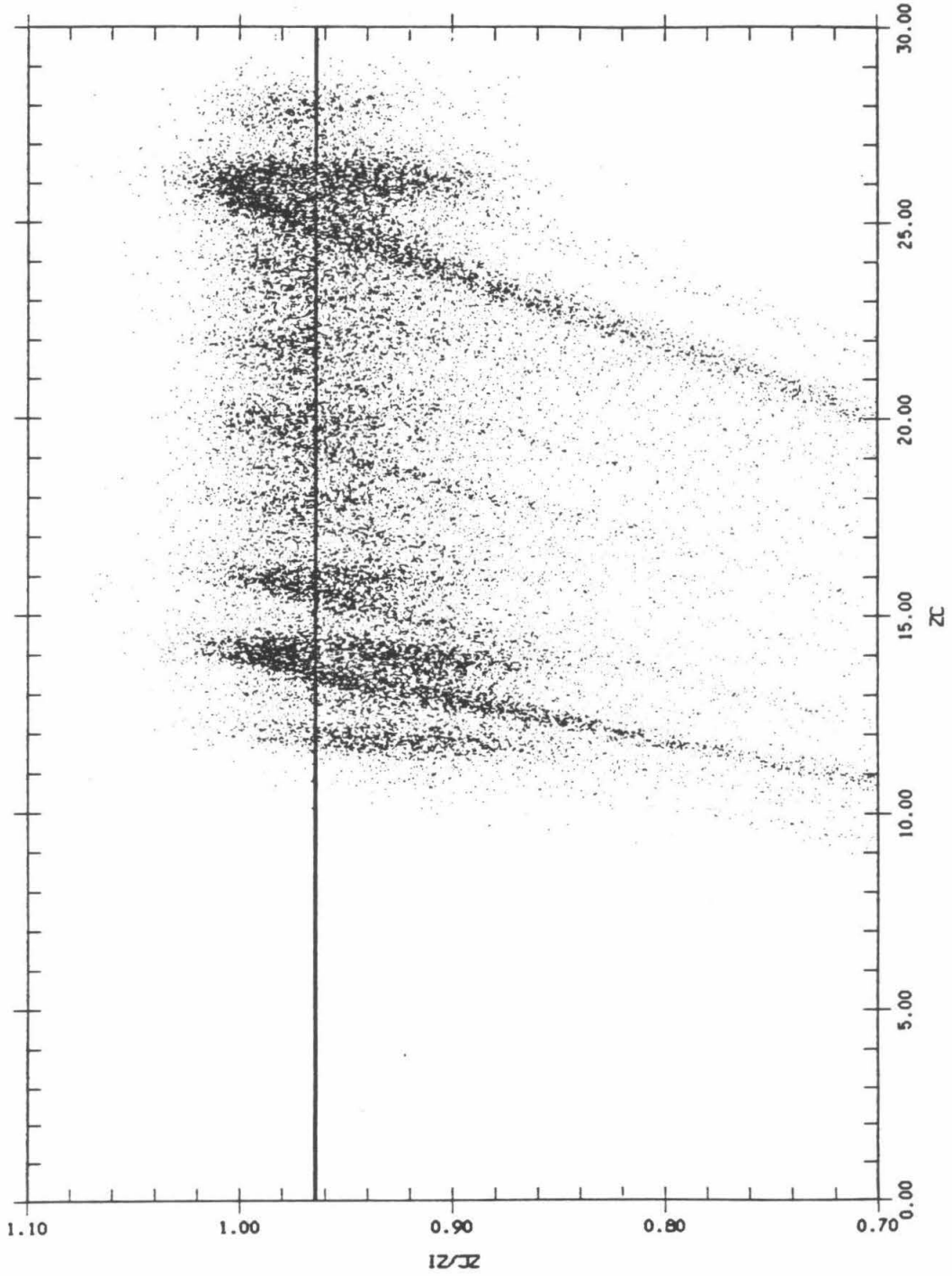
30.00
25.00
20.00
15.00
10.00
5.00
0.00
ZC
1.10
1.00
0.90
0.80
0.70
ZC/ZI

parametrized by the particle energy. (In Figures 3.3 and 2.2, curves of constant ZC/ZI are straight lines through the origin with slope equal to the ratio.) Events on Figure 3.4 with the highest values of ZC/ZI, at the tip of the curve, correspond to energies in the neighborhood of 5 GeV/nucleon with lower energies lying to the lower left and higher energies to the lower right. By selecting on ZC/ZI, we can eliminate the low energy particles of each element which would otherwise contaminate the charge peaks below it due to the energy dependence of the Cerenkov signal. The value used in the selection, 0.964, was chosen by varying the ZC/ZI requirement on the iron data in order to obtain the best combination of statistics and resolution.

3.5. Event Selections

Having selected events for which the Cerenkov charge estimate, ZC, should be a valid measure of the particle charge, we are now in a position to sort them into categories which will enable us to choose those classes of events having the best resolution. A schematic version of the classification scheme is shown in Figure 3.5. The same scheme is used for both the high cutoff and the high ZC/ZI data separately. Only particles having a Cerenkov signal and at least one ion chamber signal were used in this analysis. All others were discarded. The selection limits were originally developed for use in other charge regions and minor "tweaking" of the limits, although investigated, was deemed unnecessary because the small statistics of the analysis region precluded observation of all but large effects. The figures presented here serve as a diagnostic tool to ensure, for this first study, that the selections are reasonable, although not necessarily "optimal".

The layout of the classification scheme can be understood in terms of particle fragmentation within the instrument, and the different categories by their varying amount of contamination by interacted

Figure 3.5

Schematic diagram of the selection "tree" used to categorize events on the basis of interactions.

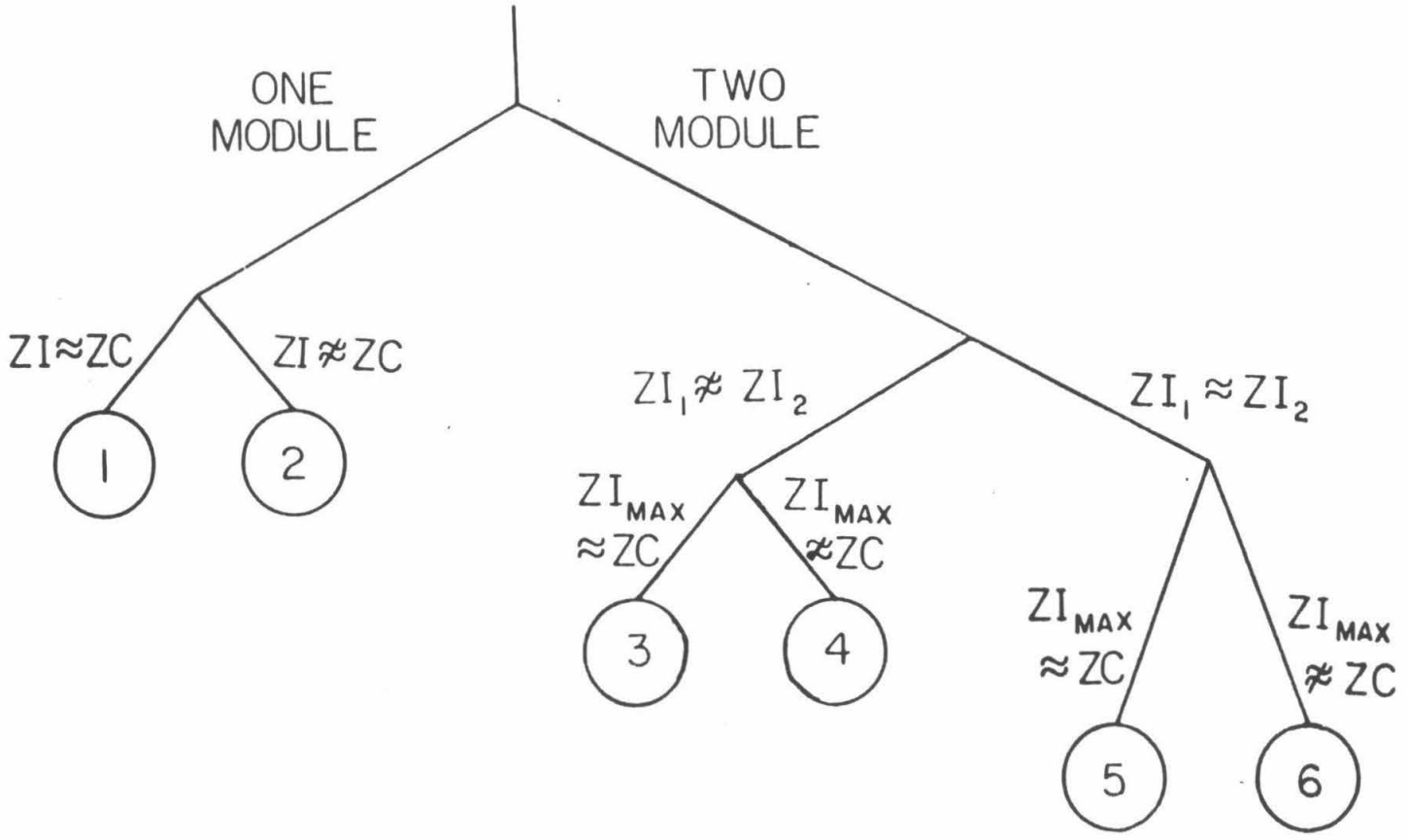
ONE MODULE
TWO MODULE
ZI≈ZC
ZI≉ZC
ZI1≉ ZI2
ZI1 ≈ ZI2
ZIMAX ≈ZC
ZIMAX ≉ZC
ZIMAX ≈ZC
ZIMAX ≉ ZC
1
2
3
4
5
6

particles. If a particle penetrates the detector without any fragmentation occurring, one would expect, at these high energies where slowing down is not important, that the charge estimates from the ion chamber, or chambers, would match that of the Cerenkov counter. However, if the particle undergoes a nuclear interaction, we would expect the fragments to give a smaller signal than the original nucleus. This is a result of the Z^2 response of the detector. At the energies considered here the fragments usually have the same β and trajectory as the incident nucleus (e.g. Greiner *et al.* 1975), therefore only the charge dependence of the instrument response is involved in a comparison between the incident nucleus and its fragments. If

$$Z_{inc} = Z_1 + Z_2 \tag{3.5}$$

then

$$Z_{inc}^2 > Z_1^2 + Z_2^2 \tag{3.6}$$

where Z_{inc} is the intact incident nucleus charge and Z_1 and Z_2 are its fragments. Thus, by examining the separate estimates of particle charge, we can eliminate particles which have undergone a charge changing interaction while passing through the instrument. Those events having the greatest number of consistent charge estimates should also include the least number of interactions and have the best resolution.

The first major classification of events in the "tree" of Figure 3.5 is on the basis of whether or not there are valid signals from ion chambers on both sides of the Cerenkov, i.e. two-module or one-module events. Having made this broad classification of particles we can now begin to eliminate interactions by examining the one module and the two module events separately. Looking first at the two module events, the first check for interactions is accomplished by comparing the ion chamber

signals on both sides of the Cerenkov box. Between the two ion chamber modules there are the two aluminum honeycomb lids, or windows, each mainly consisting of ~1.24 g cm^{-2} of aluminum, and the two Pilot 425 Cerekov radiators with a mass of ~0.568 g cm^{-2} of Lucite each (Binns 1980). This is to be compared with the average interaction lengths for Sn-Ce of ~15 g cm^{-2} in aluminum and ~6.0 g cm^{-2} in Lucite. Figure 3.6 is a histogram of

$$TWDZ = \frac{ZI_1 - ZI_2}{ZC} \tag{3.7}$$

for the high cutoff events passing the consistency checks explained in section 3.3, where we have used ZI_1 and ZI_2 to designate the two estimates of the charge derived from the mean of the ion chamber signals in each module of the sort described in 3.1 (7) (although for 90% of the events used here ZI_1 and ZI_2 are just the square root of the signal per unit pathlength) and ZC for the Cerenkov charge estimate. The histogram is centered at zero, showing that the ion chambers agree on the average. The full width at half maximum is approximately 0.07 and is dominated by the ion chamber resolution with some contributions from the charge changing interactions present. If we assume that all the width is due to the ion chamber resolution, the TWDZ width implies that the ion chamber rms charge resolution is about 2%. (An ion chamber charge resolution of 1 charge unit at Z=40 roughly agrees with the observed distributions). The lower plot displays TWDZ as a function of ZC along with the approximate agreement criteria used. The quantity which was actually used in the selection was TWDZ + 0.5/ZC. The selection required it to be less than or equal to 0.06.

It is still possible for interactions to have passed the TWDZ ion chamber agreement requirement. For example, in the charge 50-58 region, a particle could have produced a fragment of 2 charge units or less and still be accepted by this cut. For these events, we would like to distinguish between two possible cases. First, the particle may have

Figure 3.6

Histogram showing the effect of the two module agreement criterion on the high charge, high rigidity data set.

$$\mathrm{TWDZ} = \frac{\mathrm{ZI}_1 - \mathrm{ZI}_2}{\mathrm{ZC}}$$

The crossplot shows the selection as a function of ZC.

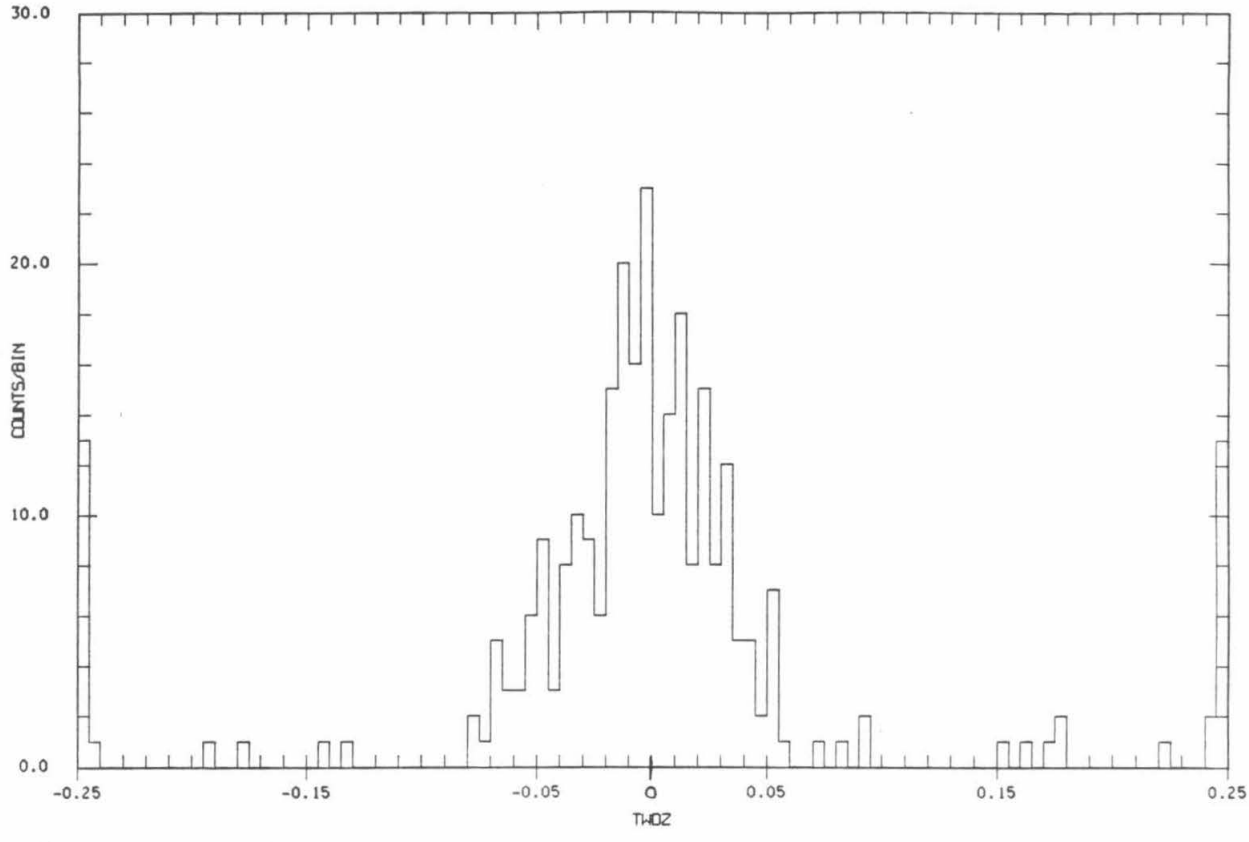
30.0
20.0
10.0
0.0
COUNTS/BIN
-0.25
-0.15
-0.05
0
0.05
0.15
0.25
THOZ

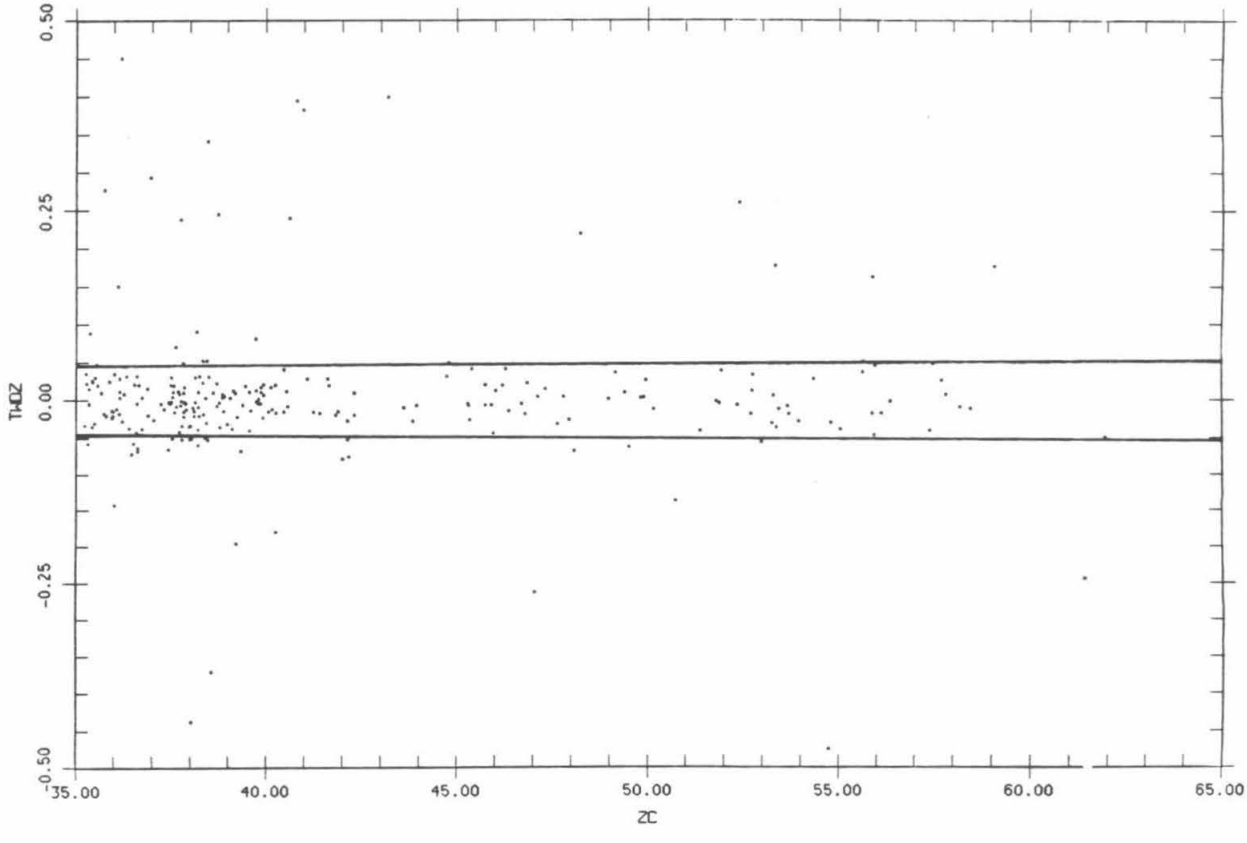
0.50
0.25
0.00
-0.25
-0.50
THOZ
35.00
40.00
45.00
50.00
55.00
60.00
65.00
ZC

undergone the nuclear interaction after its passage through the Cerenkov radiator. In this case ZC is still a valid charge estimator. The other possibility is that the interaction may have occurred before, or during, its passage through the Cerenkov, in which case ZC will not be a measure of the incident particle charge. In order to distinguish between these two possibilities a further selection is made using

$$ZDEL = \frac{ZI_{max} - ZC}{ZC} \tag{3.8}$$

where $ZI_{max} = \max \{ ZI_1, ZI_2 \}$. A histogram of this quantity for the high cutoff events which have agreement between modules is shown in Figure 3.7 along with a crossplot showing its dependence on ZC. The distribution peaks at 0.035 rather than zero both because of the normalization of ZI to minimum ionizing particles and because the use of ZI_{max} biases the distribution towards higher values. The 8 GV requirement selects events which, because of the relativistic rise in the ion chamber response, have a larger ZI than that resulting from a minimum ionizing particle, thus causing the ratio of ZI/ZC to be greater than 1.0 for the events plotted.

To understand the asymmetry of this distribution, we note that if a charge changing interaction of the type discussed above occurs before or within the Cerenkov the result will be a larger ZI_{max} than ZC and thus a larger ZDEL than normal. On the other hand, an error in ZDEL on the low side is less likely to result from an interaction of the type considered here because it would imply that the Cerenkov signal is greater than those of the ion chambers on either side of it. In consequence, since we would like to eliminate interactions which will degrade ZC, the lower limit on acceptance is not crucial as long as the extreme outliers are eliminated. Its value is -0.06. Using the uncertainty in the ion chamber ZI derived from the TWDZ distribution in Figure 3.6 and an estimated

Figure 3.7

Histogram of the agreement between Cerenkov and ion chamber charge estimates for high rigidity particles with two consistent ZI estimates.

$$ZDEL = \frac{ZI_{max} - ZC}{ZC}$$

The crossplot shows ZDEL as a function of ZC.

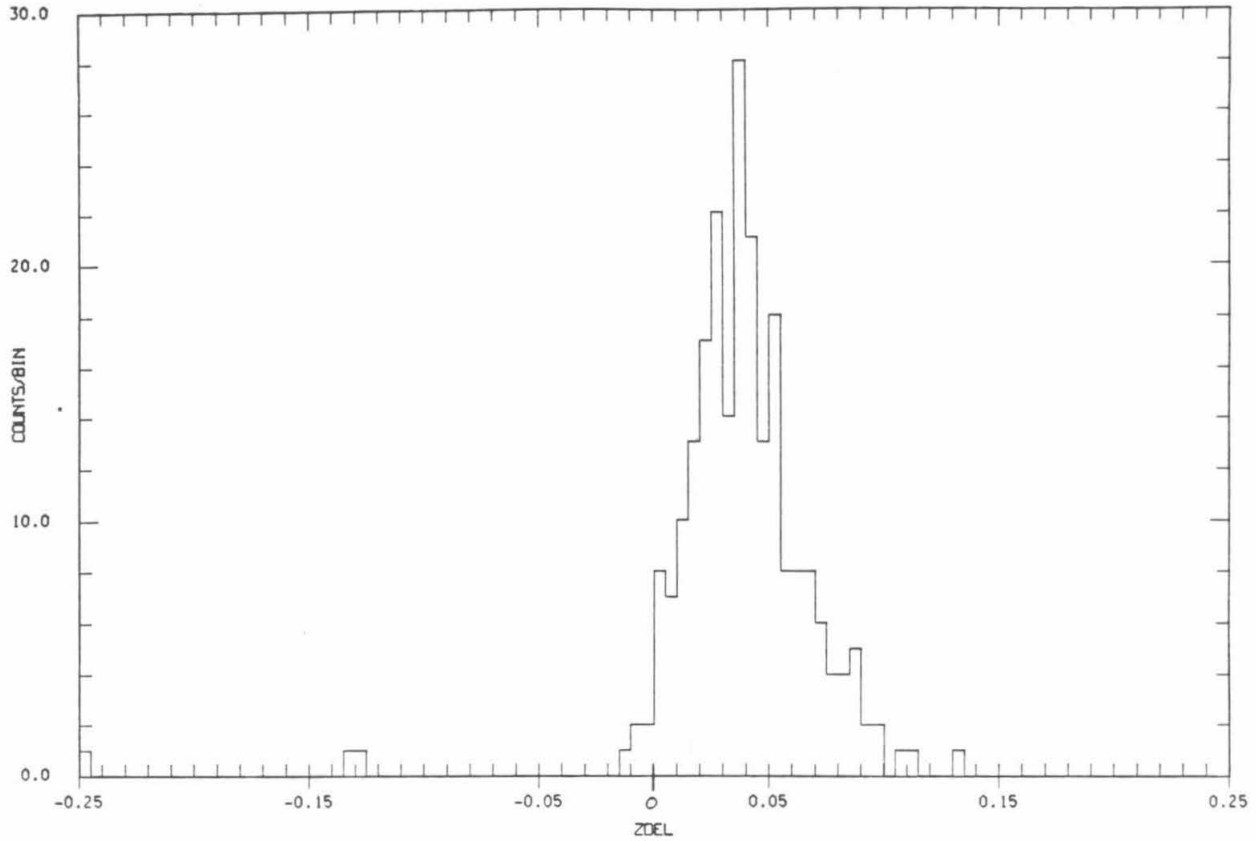
30.0
20.0
10.0
0.0
COUNTS/BIN
-0.25
-0.15
-0.05
0
0.05
0.15
0.25
ZDEL

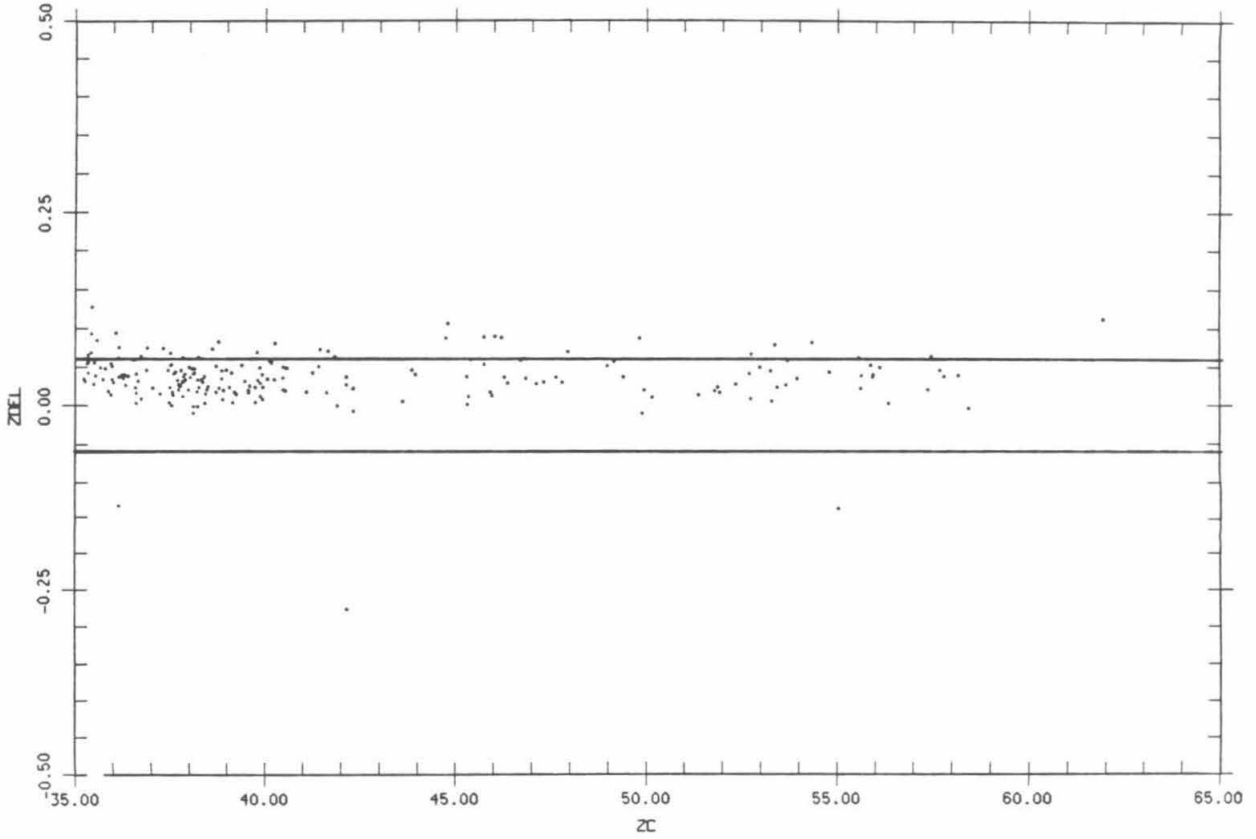
0.50
0.25
0.00
-0.25
-0.50
ZDEL
35.00
40.00
45.00
50.00
55.00
60.00
65.00
ZC

Cerenkov resolution of 0.6% based on the widths of the individual tube to average ratios (map corrected versions of Figure 3.1) we find that the expected ZDEL width should be ~0.02, consistent with what is shown. The upper limit of 0.06 is thus a selection at the ~1.25 sigma level (remembering that the peak is at 0.035). Using this value, we would expect some 10% of the "good", i.e. non-fragmented, events to be rejected (Category 6). Since Category 6 actually contains 20% of the TWDZ agreement events, half should be interactions. Adding this to the previous number outside the TWDZ limits (Category 3 and 4) implies a 28% interaction rate overall, to be compared to the 30% expected from a simple interaction model which assumes a 17 g cm^{-2} interaction length in 5.6 g cm^{-2} of aluminum traversed at a 20° incident angle. The value of 5.6 g cm^{-2} includes not only the aluminum in the lid but also the "aluminum equivalent" of the Cerenkov radiator which accounts for its shorter interaction length. Use of a 17 g cm^{-2} interaction length instead of the 15 g cm^{-2} more characteristic of the Sn-Ce region reflects the large number of particles in the distribution with charge near 40. Care should be taken in these comparisons since proton stripping reactions, which are still able to meet both the TWDZ and the ZDEL requirements, have not been excluded in the simple calculations done here. Those events accepted on the basis of both TWDZ and ZDEL (Category 5 in Figure 3.5) have three consistent charge estimates and should have the best charge resolution. The events in Category 6 on the other hand should be primarily those events for which ZC is measuring the combined fragment charges.

We can also use the ZDEL parameter to further analyze those events which were rejected on the basis of TWDZ. Although these particles have undergone charge changing interactions between the two ion chamber modules, the events which interacted after passage through the Cerenkov radiator may still have a valid ZC charge estimate. We would expect,

since both the thickness of a module lid and a single radiator sheet are approximately the same fraction of an interaction length (~ 8%) that 25% of these rejected TWDZ events would have a valid ZC, i.e. interacted in the lid after passage through both radiators and the first lid. The ZDEL histogram and crossplot for the high cutoff events which failed the TWDZ test are shown in Figure 3.8. The histogram is similar to that shown in Figure 3.7 in its asymmetry. Note, however, that this distribution peaks at a higher ZDEL value, reflecting the larger fraction of events in this subset which interacted before or within the Cerenkov chamber. The same ZDEL cut used for Figure 3.7 was employed here. Again the lower limit is relatively unimportant. Use of 0.06 for the upper limit can be justified on the grounds of attempting to select out the non-fragmented component which should have a distribution similar to the peak in Figure 3.7. The actual fraction of events in Category 3 (interaction after Cerenkov) is approximately 40%, higher than the 25% expected, which indicates that this category includes some particles which have interacted before or within the Cerenkov. There is an additional selection made on those events for which the direction of motion is "known". If the module entered first has a lower ZI than the second ZI, it is rejected without consideration of its ZDEL. This is a minor effect eliminating only one particle in the Sn-Ce region. Since these Category 3 events have only two consistent charge estimates, the resolution is not expected to be as good as those in the analogous two module agreement Category 5.

The one module events cannot be examined for interactions on the basis of module agreement. However, the ZDEL test can be used to select events with a consistent ZI and ZC. The ZDEL histogram for the one module, high cutoff events is shown in Figure 3.9. The most obvious feature is the large number of events with an unusually low ZDEL. Further investigation reveals that all of these events except 4 are "one

Figure 3.8

Histogram of the agreement between Cerenkov and ion chamber charge estimates (ZDEL) for high rigidity particles with two inconsistent ZI estimates and a crossplot showing the ZC dependence.

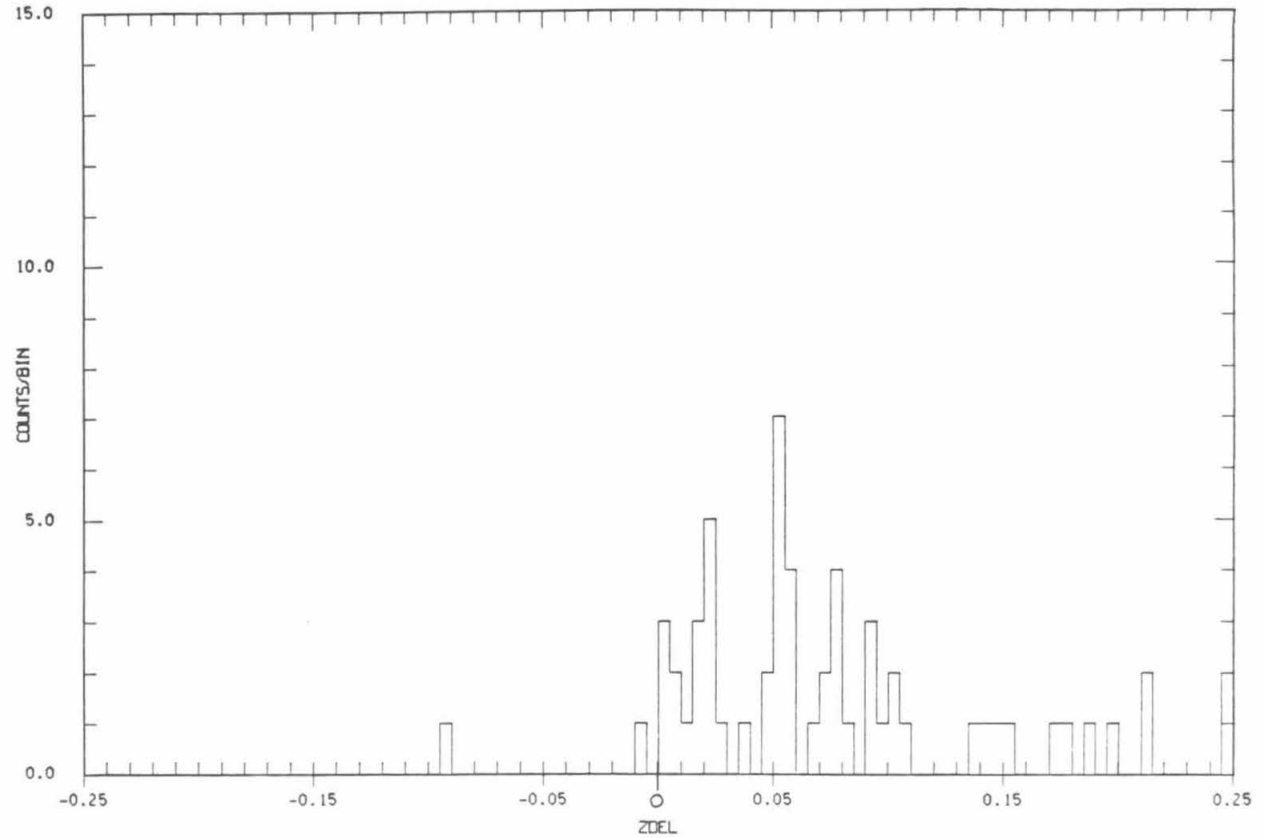
15.0
10.0
5.0
0.0
COUNTS/BIN
-0.25
-0.15
-0.05
0
0.05
0.15
0.25
ZDEL

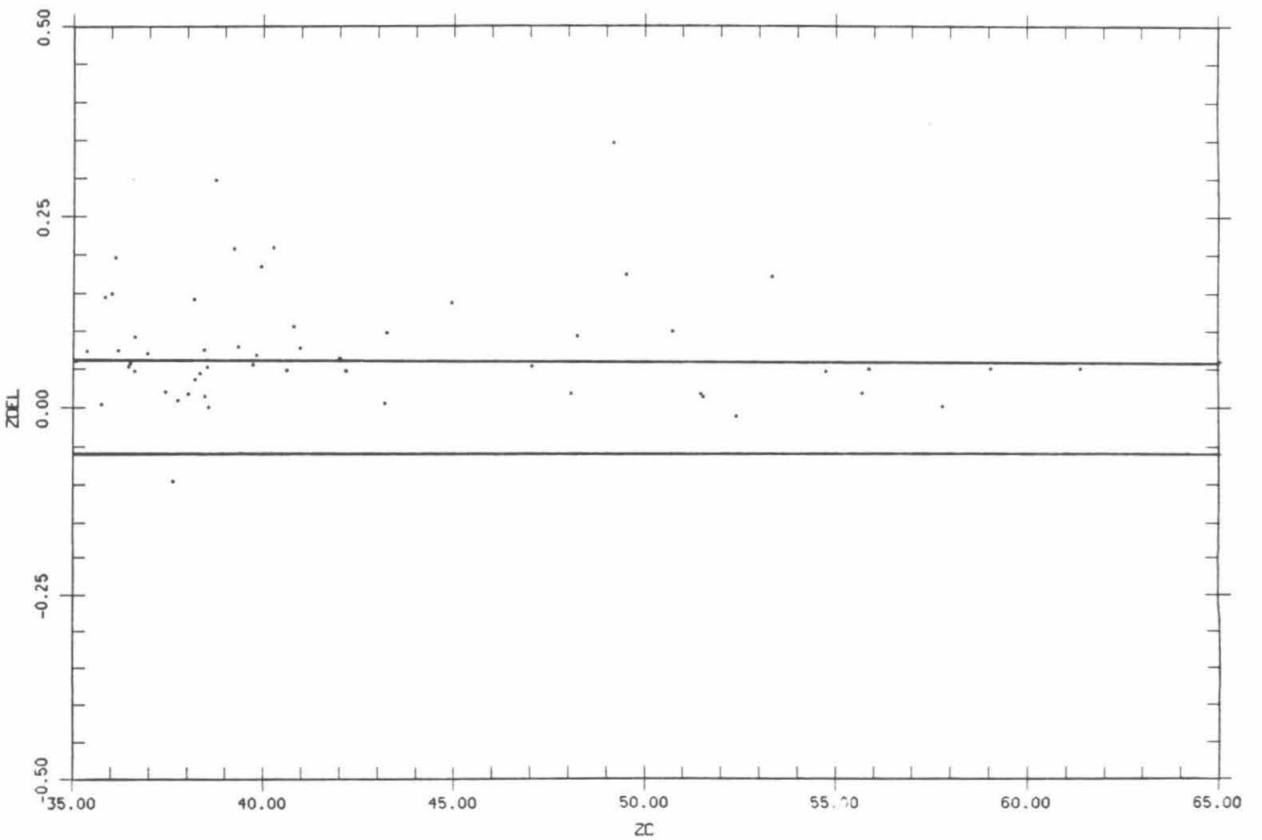
0.50
0.25
0.00
-0.25
-0.50
ZDEL
35.00
40.00
45.00
50.00
55.00
60.00
65.00
ZC

Figure 3.9

Histogram and crossplot versus ZC of the agreement between Cerenkov and ion chamber charge estimates (ZDEL) for high rigidity particles having only one ZI estimate.

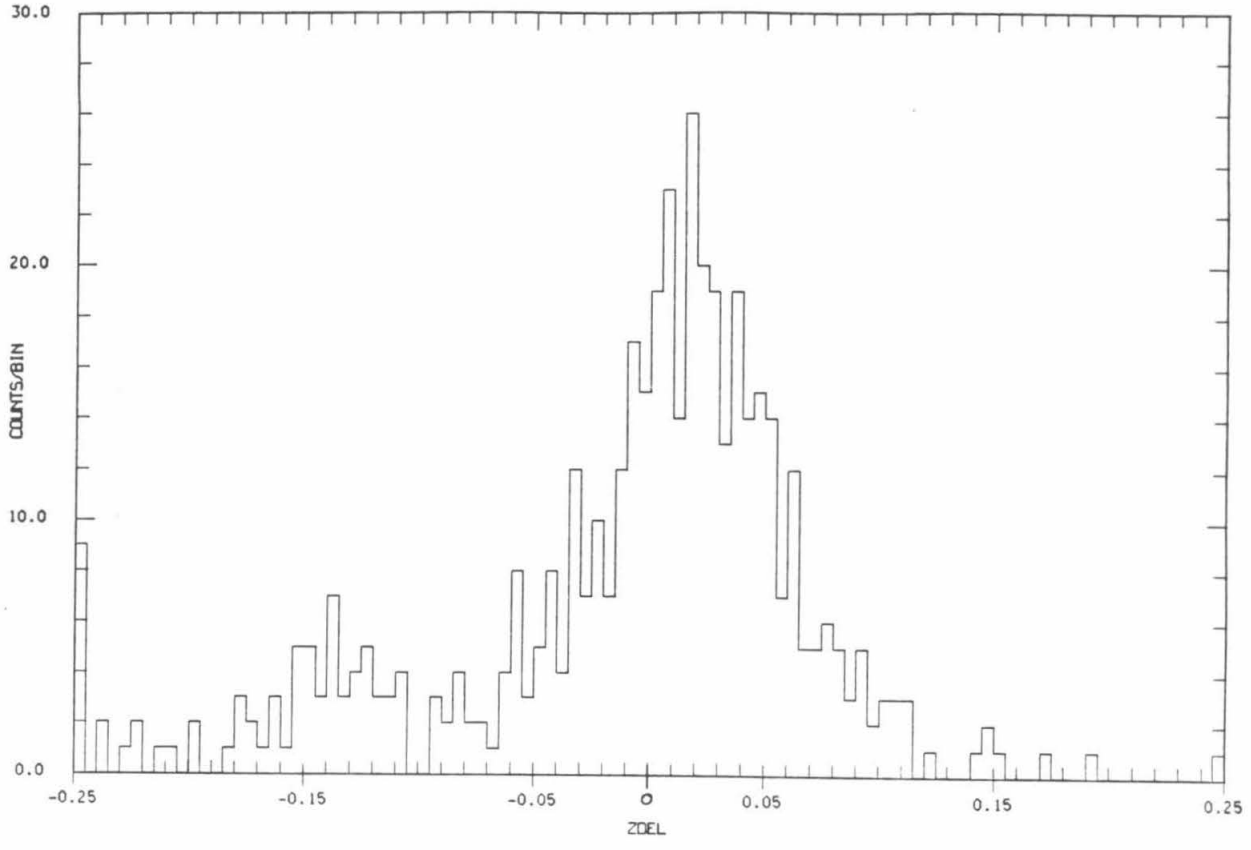
30.0
20.0
10.0
0.0
COUNTS/BIN
-0.25
-0.15
-0.05
0
0.05
0.15
0.25
ZDEL

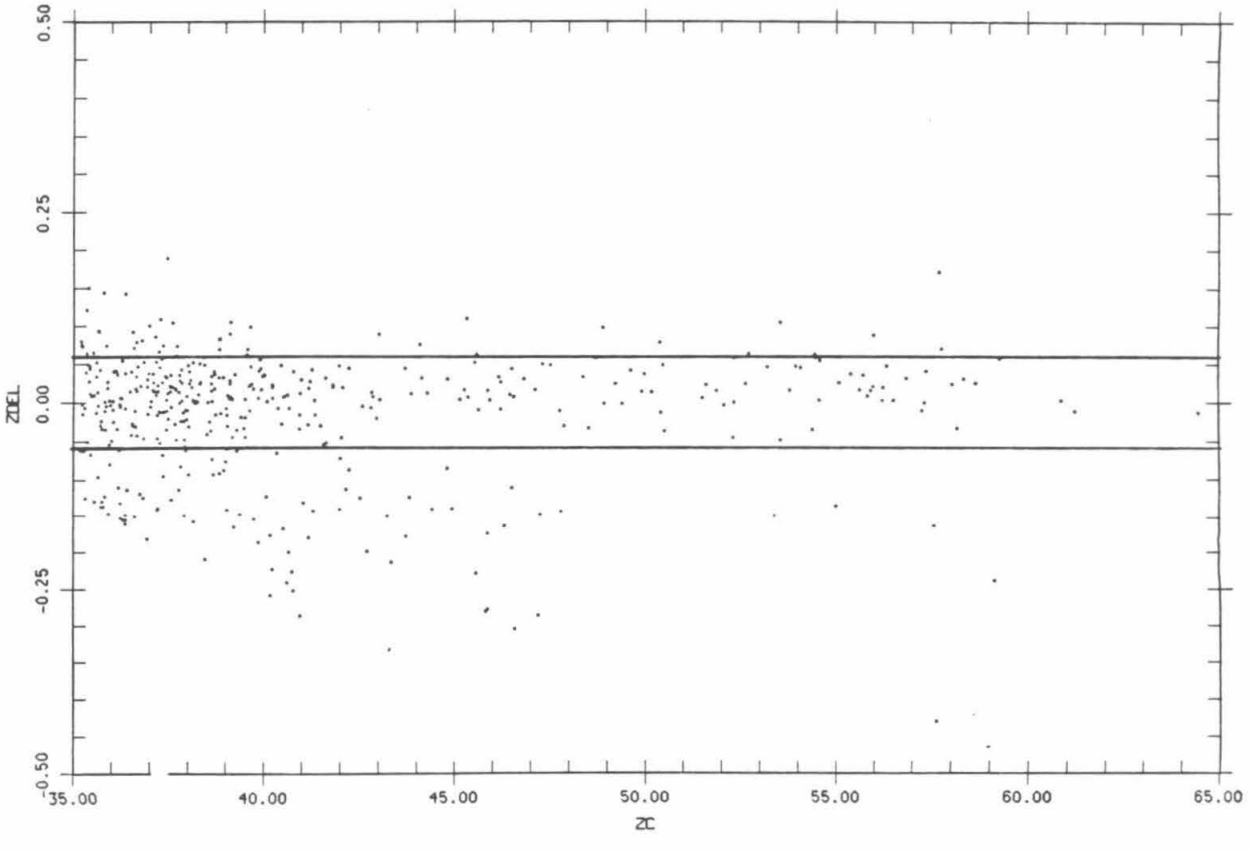
0.50
0.25
0.00
-0.25
-0.50
ZDEL
35.00
40.00
45.00
50.00
55.00
60.00
65.00
ZC

radiator" events, i.e. events which, on the basis of their trajectory information, have penetrated only one of the two lucite sheets forming the Cerenkov radiator (RAD1 or RAD2 of Figure 2.2). These events would be expected to be of lower quality for several reasons. First, because of the instrument geometry, events in this category would also be expected to be wide angle and have only two hodoscope planes determining their trajectory. In addition, both planes are most likely on the same side of the Cerenkov box and, as a result, the computed position of the particle in the Cerenkov box has a larger uncertainty because of the "lever arm" from the hodoscope to the radiator. (Referring to Figure 2.2 again, in general, if the particle penetrated RAD2 and not RAD1, it must have also penetrated the X3-Z3 HODO and the X4-Z4 HODO because of the coincidence requirement since it could not have gone through the X2-Z2 HODO or the X1-Z1 HODO without penetrating RAD1). If the particle actually did penetrate two radiators, but was assigned to the one radiator category due to trajectory error, we would expect its ZC to be too high (because of an erroneous pathlength correction in the Cerenkov) with a resulting low ZDEL. Additionally, the map used to correct for Cerenkov areal response is based on two radiator events only and may only be approximately accurate for one radiator events. The ZDEL distribution for the one module, one radiator events only is shown in Figure 3.10. Note that there are two peaks, the one at ZDEL = −0.12, which may be attributable to the misassignment discussed above, and another at the location of the main peak. As can be seen from the crossplot, most of these low ZDEL particles are present only at lower ZC values.

Figure 3.11 shows the ZDEL plots for the two radiator events of Figure 3.9. This distribution is wider, rms resolution of ~0.026, than that shown in Figure 3.7 for the two module events accepted on the basis of TWDZ. We note that here the definition of ZDEL differs slightly in its physical meaning from the one used in the other selections. For two module

Figure 3.10

Histogram and crossplot versus ZC of the agreement between Cerenkov and ion chamber charge estimates (ZDEL) for the one radiator events in Figure 3.9.

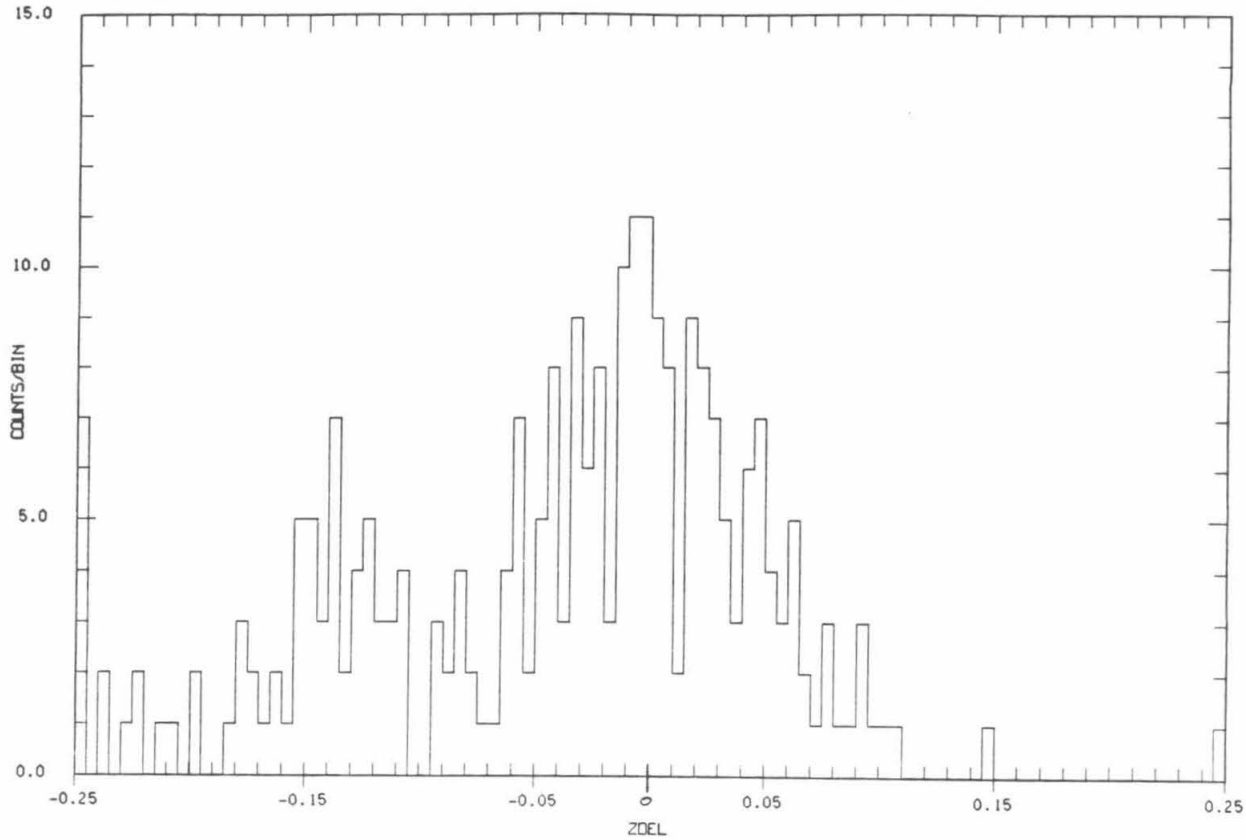
15.0
10.0
5.0
0.0
COUNTS/BIN
-0.25
-0.15
-0.05
0
0.05
0.15
0.25
ZDEL

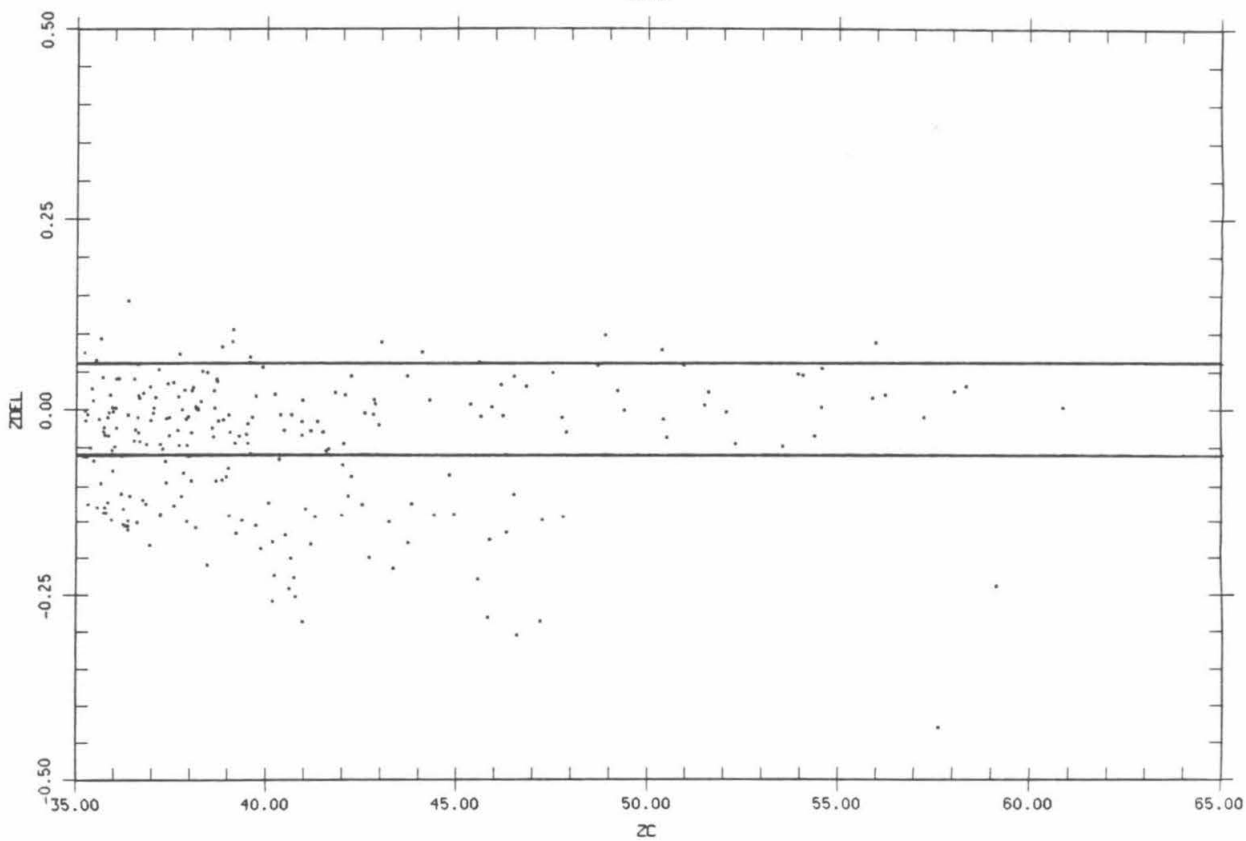
0.50
0.25
0.00
-0.25
-0.50
ZDEL
35.00
40.00
45.00
50.00
55.00
60.00
65.00
ZC

Figure 3.11

Histogram and crossplot of ZDEL for only the two radiator events of Figure 3.9

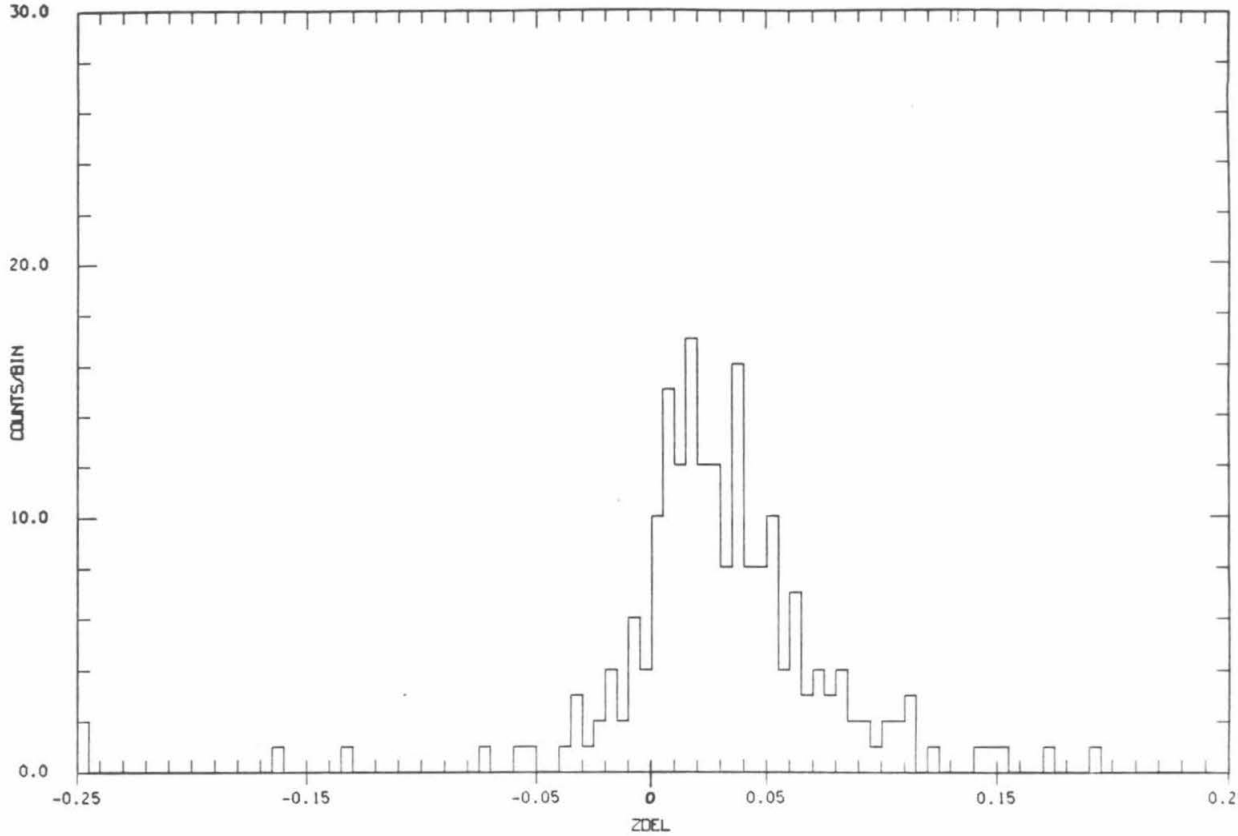
30.0
20.0
10.0
0.0
COUNTS/BIN
-0.25
-0.15
-0.05
0
0.05
0.15
0.25
ZDEL

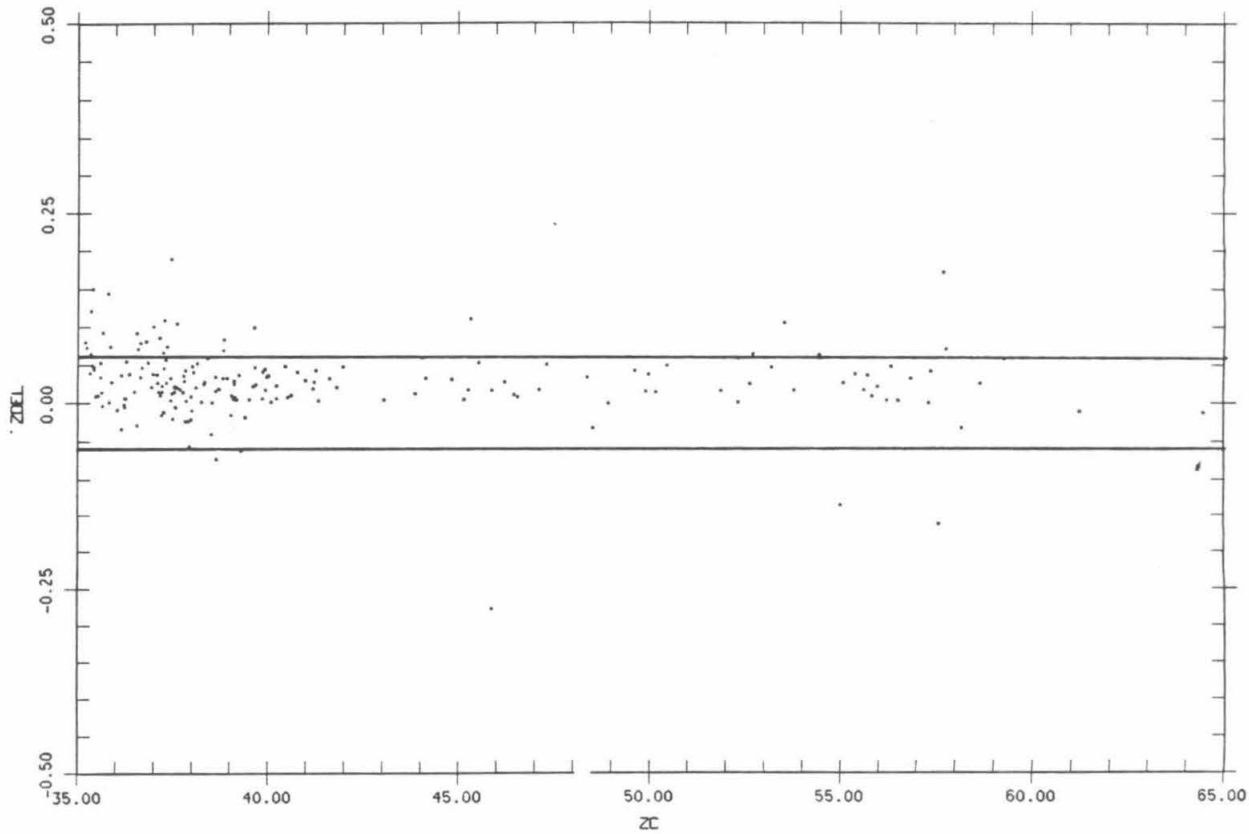
0.50
0.25
0.00
-0.25
-0.50
ZDEL
35.00
40.00
45.00
50.00
55.00
60.00
65.00
ZC

events, the use of ZI_{max} results in the preferential selection of the ion chamber signal from the module containing the non-interacted incident particle. As a result the ZDEL distribution does not include any values which were calculated with ZC measuring the incident particle and ZI the fragments (ignoring fluctuations). For one module events however, there is only one set of ion chambers and the selection of ZI_{max} is superfluous. Thus it is equally likely, given an interaction, that ZC is measuring the incident particle and ZI the fragments as it is for the opposite case. The consequences of this do not affect the logic behind the selections. If the ion chamber measures the fragments and the Cerenkov the incident particle, ZDEL is low because ZC > ZI. Note however that these events should have a valid ZC. If, on the other hand, the fragments are in the Cerenkov instead, ZDEL is high, as before. Thus the upper limit is again the more important one for eliminating interactions. For events on the low side of the ZDEL distribution, ZC should still be a valid charge estimate.

In order to simulate this distribution, we plotted ZDEL for the events in Figure 3.7 (two consistent ion chambers) using ZI_1 or ZI_2 instead of ZI_{max} (the choice between them for each event being made at random). The distribution resembles the main peak shown in Figure 3.11, being wider, a sigma of ~.03, than the ZDEL histogram made using ZI_{max}. We can therefore attribute this extra width to the use of the "fragmented" ZI. For the results presented here, because a comprehensive theory of one radiator events was outside the scope of this analysis, we did not separate them from the two radiator events and therefore they may have functioned as a possibly lower resolution component of the one module events. However, examination of the one radiator events separately reveal no significant difference between them and the two radiator events for the particles in the Sn-Ce region.

The same ZDEL criterion was used for the one module ZDEL plot, Figure 3.9, as was used for the others. As discussed previously, events with a low ZDEL should still have a valid ZC charge estimate. Although this is not true in the case of a misassignment of two radiator events to the one radiator category, the crossplot shows that this is only important at the lower charges. Since the upper side of the ZDEL distribution is not affected by including events for which ZI is measuring the fragments, the same 0.06 limit is still appropriate. Using these values results in 23 (± 6) % of the events from the Sn-Ce region being placed in the interaction category (Category 2). To estimate this consider a simple model of fragmentation which assumes a fragmentation pathlength of 15 g cm^{-2} in 2.8 g cm^{-2} of aluminum traversed at a 45° incident angle. This calculation implies an 21% interaction rate. We should note here that we cannot distinguish, for these one module events, between interactions occurring within the Cerenkov and those occurring between the Cerenkov and the ion chamber for events moving from Cerenkov to ion chamber. As a result, a larger amount of contamination may be present in this category than is present in the two module events.

The same selection "tree" can also be applied to the events selected on the basis of ZC/ZI. The only category having sufficient resolution for inclusion in this analysis was Category 5 of Figure 3.5, the two module events which passed all agreement tests. Shown in Figure 3.12 is the TWDZ histogram and crossplot for the two module events. The width and number of events classified as interactions is similar to that of the two module-high cutoff events (Figure 3.6). The ZDEL plot for the particles which met the TWDZ requirement are shown in Figure 3.13 along with the ZDEL agreement criteria. The sharp cutoff in ZDEL on the high side is an artifact of the selection that ZC/ZI must be greater than 0.964. The cutoff is not perfectly sharp because the mean of ZI_1 and ZI_2 was used for the ZC/ZI selection while ZI_{max} was used in ZDEL.

Figure 3.12

Two module agreement criterion for high ZC/ZI events as a function of ZC (lower) and as a histogram of TWDZ (upper).

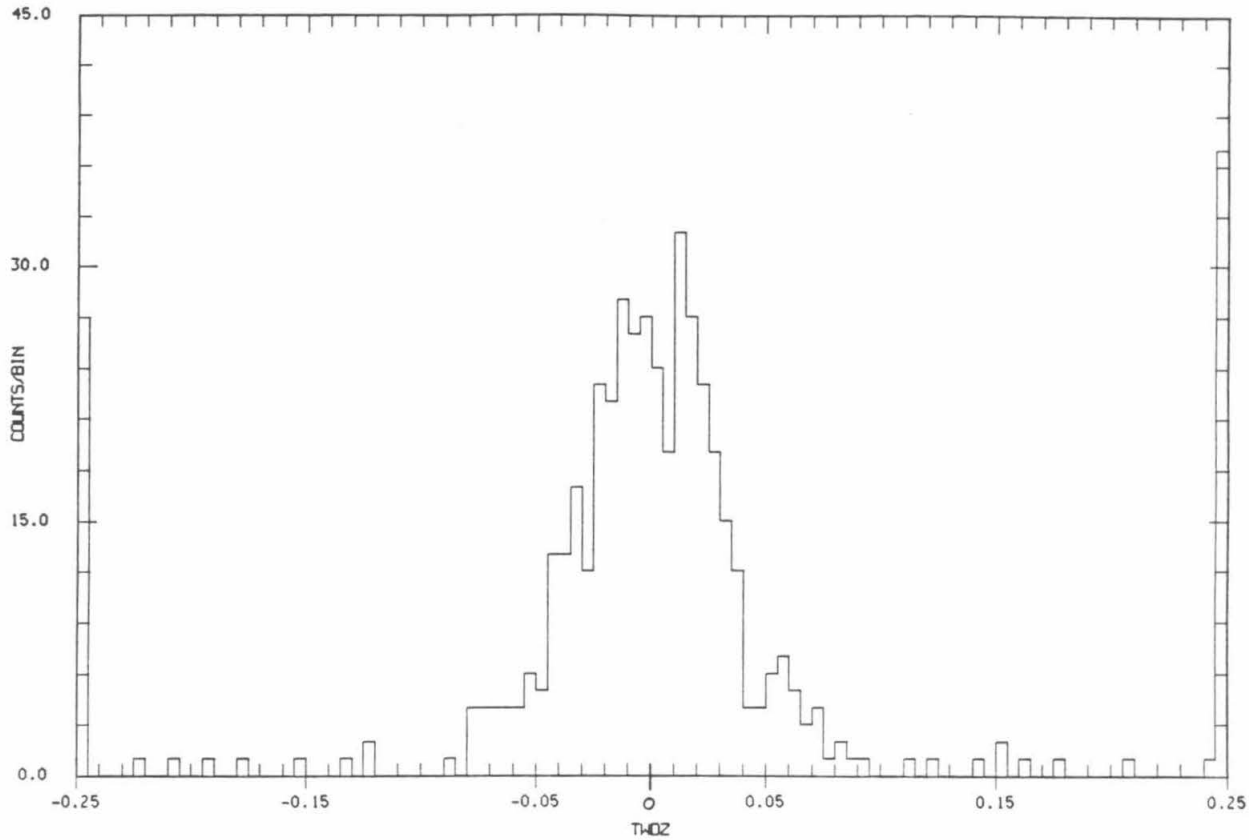
45.0
30.0
15.0
0.0
COUNTS/BIN
-0.25
-0.15
-0.05
0
0.05
0.15
0.25
THDZ

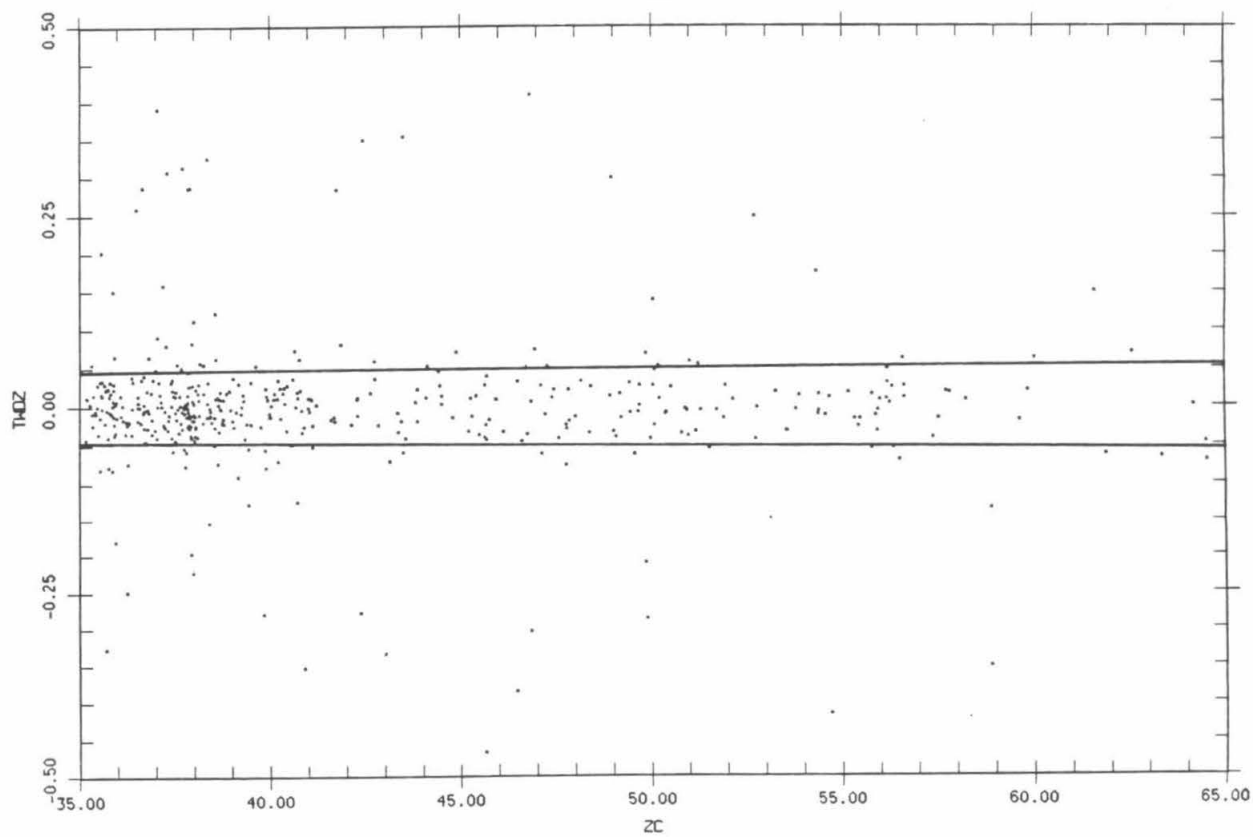
0.50
0.25
0.00
-0.25
-0.50
THDZ
35.00
40.00
45.00
50.00
55.00
60.00
65.00
ZC

Figure 3.13

Histogram and crossplot versus ZC of ZDEL, the agreement between ion chamber and Cerenkov charge estimates, for two module high ZC/ZI events.

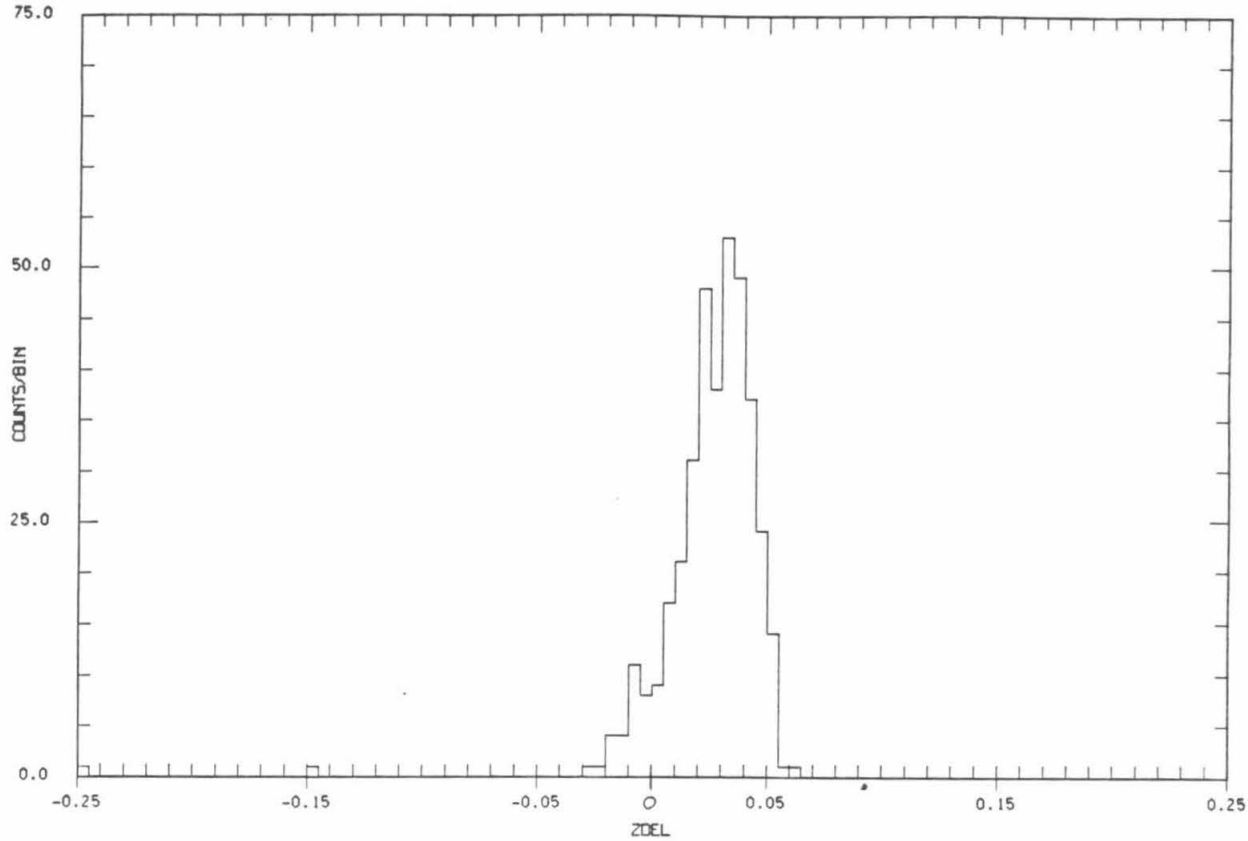
75.0
50.0
25.0
0.0
COUNTS/BIN
-0.25
-0.15
-0.05
0
0.05
0.15
0.25
ZDEL

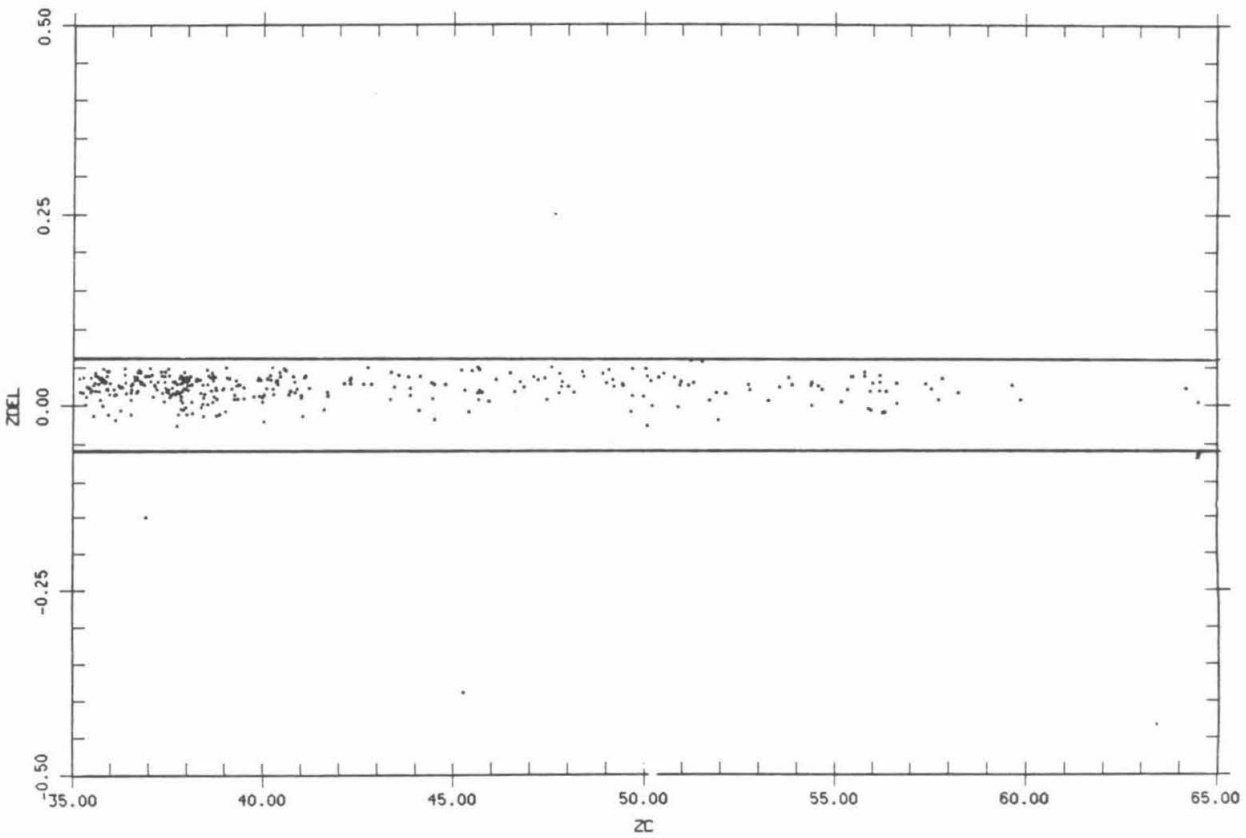
0.50
0.25
0.00
-0.25
-0.50
ZDEL
35.00
40.00
45.00
50.00
55.00
60.00
65.00
ZC

3.6. Final Data Set

The final decision of which of the non-interaction categories (1, 3, and 5 in Figure 3.5) to select for analysis was based on the resolution exhibited by histograms made using a modulo 2 superposition of the data with assigned Cerenkov charge between 49.0 and 59.0. The modulo 2 superposition consists of binning the data according to the difference between its assigned charge and the nearest even integer. This has the effect of adding together the even (and odd) element peaks, thereby increasing the statistical accuracy with which the resolution can be determined. The method is useful here because the odd charge element abundances, for any proposed nucleosynthesis model in this region, tend to be lower than the adjacent even charge element abundances. As a result, the even elements should dominate the modulo 2 histograms.

The categories actually used in the analysis are shown in Figure 3.14 along with their associated modulo 2 histograms. Table 3.1 gives a listing of the number of high charge events meeting the consistency requirements of section 3.2 in each category, or bin of Figure 3.5. Also shown are the numbers obtained considering only the Sn-Ce region ($49.0 \leq ZC \leq 59.0$). High cutoff and high ZC/ZI events are listed separately. In retrospect, the categories which were selected are not a surprise. The selected categories are those having the most information about each particle. The high cutoff, two module events have three consistent measurements of the charge and an independent estimate of the particle energy. A Gaussian fit to their modulo 2 histogram, taking into account the spillover from neighboring elements, indicates a rms charge resolution of 0.47 ± 0.06 charge units, where the error is approximated using the formula for the uncertainty in the sigma of a gaussian distribution, i.e. $\frac{\sigma}{\sqrt{2\,N}}$ with N the number of events in the distribution. The high cutoff, one module events, although having a modulo 2 peak which

Figure 3.14

Final categories of Figure 3.5 selected for use in this data set. Histograms are plotted in 0.5 charge unit bins. Also shown are the modulo 2 histograms (in 0.25 charge unit bins) used in the selection.

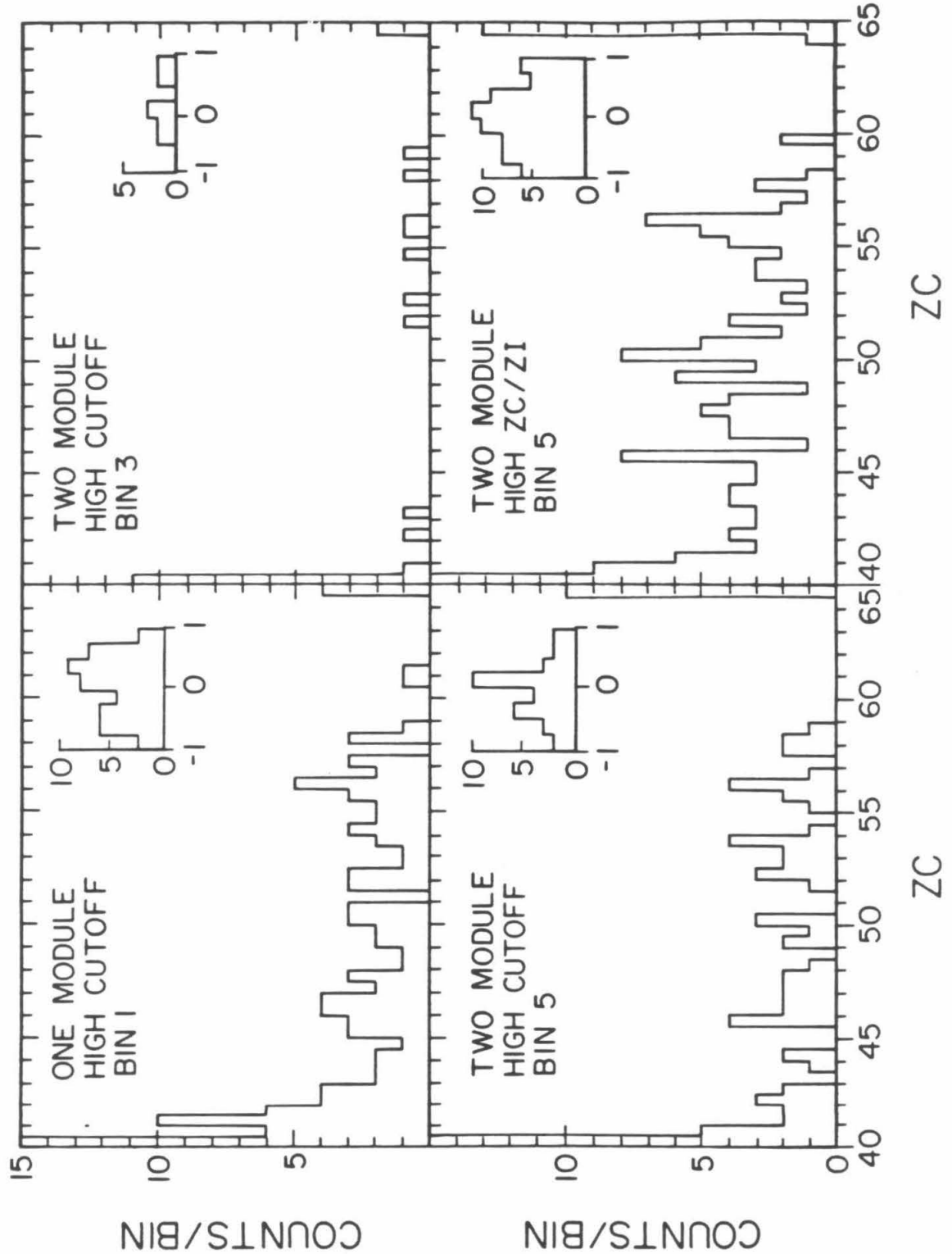
ONE MODULE
HIGH CUTOFF
BIN 1
TWO MODULE
HIGH CUTOFF
BIN 3
TWO MODULE
HIGH CUTOFF
BIN 5
TWO MODULE
HIGH ZC/ZI
BIN 5
COUNTS/BIN
ZC

TABLE 3.1

High Charge Events (ZC>35.0) by Category

Subset	Cat 1	Cat 2	Cat 3	Cat 4	Cat 5	Cat 6
High Rigidity	311	149	23	35	184	45
(Sn-Ce)	44	13	6	5	32	8
High ZC/ZI	576	149	61	68	371	3
(Sn-Ce)	100	15	10	10	63	1

Note: Category Numbers as in Figure 3.5 with Sn-Ce defined as those events with $49.0 \leq ZC \leq 59.0$

is less regular and pronounced, still have a nominal resolution of 0.54 ± 0.06. The two module high cutoff events in bin 3 which were salvaged from the TWDZ interaction events have the poorest statistics and cannot be shown to be statistically different from a uniform distribution. Nevertheless, there is a hint of resolution, a nominal 0.43 ± 0.12, and they might be expected to have at least some valid ZC charge estimates. The high ZC/ZI events, lacking the independent measure of energy, do not exhibit as good a resolution as their high cutoff counterparts having only 0.60 ± 0.05 charge unit resolution (cf. the two "Bin 5" modulo 2 histograms in Figure 3.14). The lower quality categories not selected for use, 1 and 3 for the high ZC/ZI events, have a combined modulo 2 histogram containing 106 events which is consistent with a uniform distribution containing the same number of events, the difference being significant at only the 26% level.

The individual categories selected were normalized to iron by applying the same selections to several days of iron data and then using a normalization factor to position the iron peak at 26. This same normalization factor was then used to correct ZC for the high charge particles. This method worked well for all the high cutoff subsets giving normalizations of 1.00142, 1.00361, and 1.00493 for Bins 1, 3, and 5 respectively. However, for the high ZC/ZI subsets, the normalization obtained in this way was incorrect. For the subset of these events actually used, those with two modules in agreement, the normalization was varied to obtain an approximately centered modulo 2 histogram. The final normalization factor was 1.0000, as compared to the iron result of 1.01521. The discrepancy between the iron and the modulo 2 normalizations for the high ZC/ZI subset has not been fully explained. However, it may be due to spectral differences, non-Z^2 effects in the ion chambers, or a combination of both. Such effects, although not insignificant from iron (Z=26) to tin (Z=50), should be unimportant in the relative abundances of the

elements from tin to cerium (Z=58).

The final data set is shown in Figure 3.15. The main histogram, in 0.25 charge unit bins, exhibits peaks at charge 38 and 40 serving to establish our charge scale. Possible charge dependent biases in the selections are such that relative abundances of widely separated charges should not be inferred from this plot. Inset a is an enlargement of the region of interest in 0.5 charge unit bins. One can clearly see peaks at the even elements $_{50}$Sn, $_{52}$Te, $_{54}$Xe, $_{56}$Ba, and $_{58}$Ce. Also shown, as inset b, is the modulo 2 histogram of the final data set. A Gaussian fit to this histogram, taking into account the spillover from neighboring elements, indicates a rms charge resolution of 0.55 ± 0.03, with the errors again estimated assuming a gaussian distribution. This resolution would be expected to be the result of similar contributions from photoelectron statistics (Garrard 1980) and residual mapping variations. The difference between it and a uniform distribution with the same number of events is significant at the greater than 99% level. The data set presented here has several differences from the one presented in Binns *et al.* (1983). As the result of a reanalysis of the data, some additional time periods were included (~4% increase) and a restriction on position in the Cerenkov radiator was relaxed (~12%). Additionally, all of the questionable trajectory events (58 in the Sn-Ce region) previously included in the data set, were eliminated here. These differences did not significantly change any of the relative abundances.

The presence of a peak in the modulo 2 histogram, coupled with the presence of a peak at charge 38, shows that our assumption of Z-squared scaling of the Cerenkov signal cannot be significantly in error. Since elements with even charge are more abundant than their neighboring odd elements, we are not likely to have an error of one charge unit, but an error of approximately two charge units cannot be immediately ruled out. However, if there were a two charge unit error for any

Figure 3.15

Histogram of the data from charge 35.0 to 60.0 in 0.25 charge unit bins. Although negligible over the limited range from $_{50}$Sn to $_{58}$Ce, charge dependent biases in the consistency and energy selections may affect the relative abundances of widely separated charges. Insets show (*a*) the region of interest in 0.5 charge unit bins and (*b*) a modulo 2 histogram of the data from charge 49.0 to 59.0 in 0.25 charge unit bins.

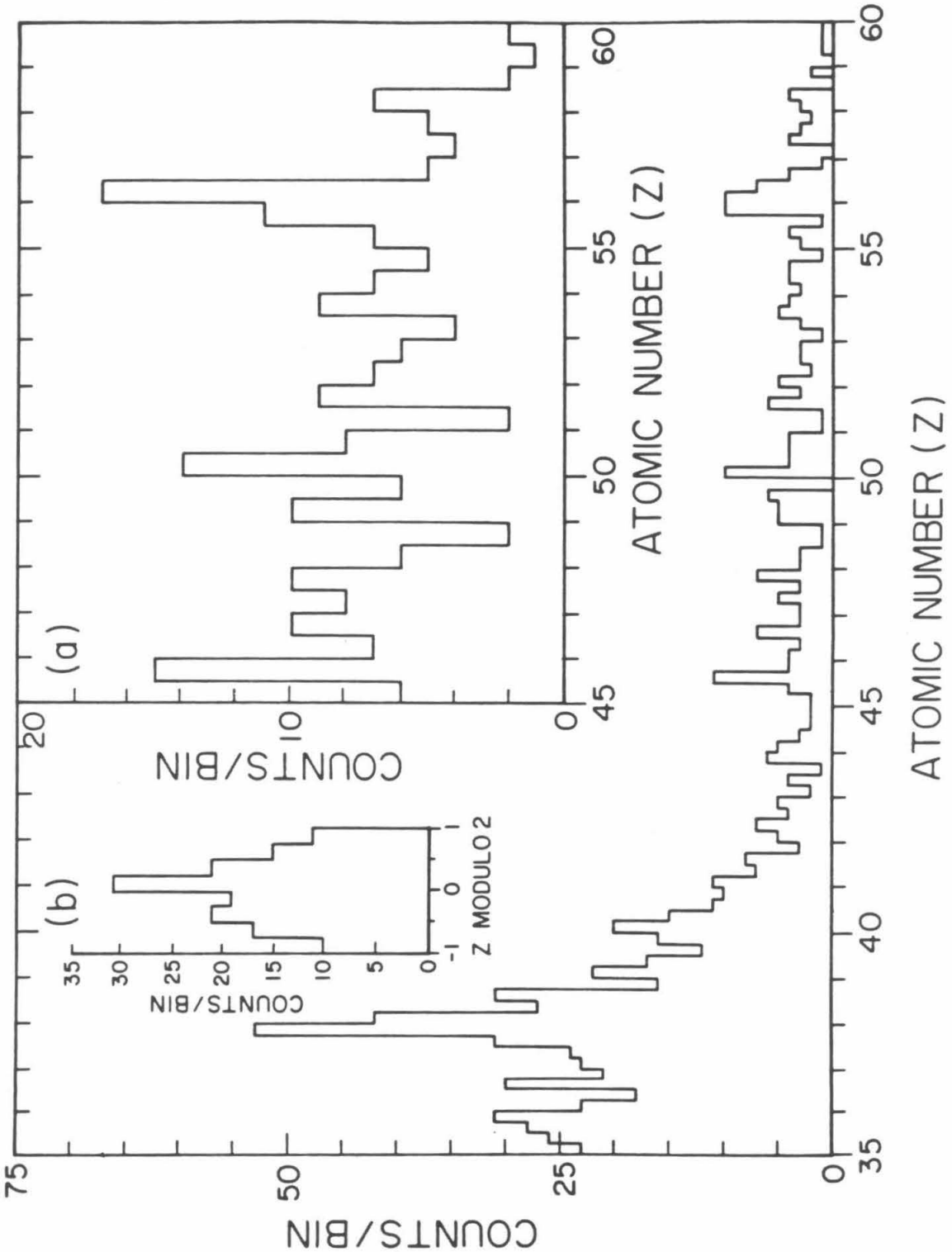
COUNTS/BIN
75
50
25
0
35
40
45
50
55
60
ATOMIC NUMBER (Z)
(a)
20
10
0
45
50
55
60
ATOMIC NUMBER (Z)
(b)
35
30
25
20
15
10
5
0
-1
0
1
Z MODULO 2

one of the peaks in inset a, i.e. the Sn-Ce region,, while the peak at 38 was correct, then the separation between even element peaks in this interval would be approximately 1.7 or 2.3 charge units (depending on the direction of the error) rather than 2.0, with the result that the modulo 2 histogram would not have such a well defined structure. Furthermore, such a large error in the charge estimate is not consistent with calculations of non-Z^2 Cerenkov effects by Derrickson *et al.* (1981). Earlier results from the Heavy Nuclei Experiment, using a different data subset have also shown the approximate validity of Z-squared scaling up to charge 40 (Binns *et al.* 1981b).

Table 3.2 gives the abundances of $_{50}$Sn, $_{54}$Xe, $_{56}$Ba, and $_{58}$Ce normalized to our best estimate of the abundance of $_{52}$Te. These values have been obtained from fitting both even and odd elements, in the range from Z = 45.0 to Z = 60.0, to the 0.25 charge unit histogram using a Gaussian resolution function. The standard deviation of the assumed Gaussian was parametrically varied to obtain the best fit to the data. In addition, the abundances were constrained to be non-negative. The "quality of fit" was determined both by using minimum χ^2 methods, which assume a Gaussian distribution for the uncertainty in each histogram bin, and by maximum likelihood methods, which assume a Poisson distribution. Results for the relative abundances of the even elements did not differ significantly between the two methods. The table values are derived from the χ^2 fit using a value of 0.55 for the Gaussian standard deviation. The uncertainties are the limits, for the given parameter, at which the χ^2 can be made equal to the minimum χ^2 plus one by allowing the other parameters to vary (see e.g. Bevington 1969). This should correspond, approximately, to the one standard deviation errors. The "best fit" abundances have a χ^2 of 48.47 for 43 degrees of freedom. There is a 72.2% probability of obtaining a χ^2 this high or higher by chance. The best fit value of the charge resolution has $\chi^2 + 1$ limits

TABLE 3.2

Element	Abundance (Fit Results)	Abundance ($_{52}$Te ≡ 1)
$_{50}$Sn	41.23 ± 9.47	1.65 ± 0.38
$_{52}$Te	24.93 ± 6.98	1.00 ± 0.28
$_{54}$Xe	25.53 ± 6.73	1.02 ± 0.27
$_{56}$Ba	44.91 ± 7.48	1.80 ± 0.30
$_{58}$Ce	20.27 ± 6.23	0.81 ± 0.25

extending from approximately 0.44 to 0.60 charge units. Also indicated in Table 3.2 are the actual abundance values derived from the χ^2 fit.

No corrections have been applied to the data for fragmentation in the instrument. Employing a simple model of fragmentation, which uses an empirical geometrical cross section, σ, for fragmentation of the incident nuclei of the form

$$\sigma = \pi r_o^2 \left[A_T^{1/3} + A_B^{1/3} - b \right]^2 \qquad (3.9)$$

where r_o = 1.35 fm, b = 0.83, (Westfall *et al.*, 1979) and A_T and A_B are the mass numbers of the target (aluminum) and incident nucleus respectively, and which assumes an equal probability for production of all lower charge fragments, the relative adjustment factors for the the even charge nuclei in this limited charge range are less than 5%.

IV. DISCUSSION

4.1. Overview

The measurements presented in the previous chapter are the first in this charge range to exhibit resolution of the even charge elements. In this chapter we will discuss these results in light of the nucleosynthesis processes believed responsible for the formation of the ultra-heavy cosmic rays. The first three sections will enumerate the complications and uncertainties which arise in comparing the measured cosmic ray flux to the theoretical results of nucleosynthesis. The next two sections will compare our results to the various models and to previous measurements in the same charge interval. Finally, we will conclude with a brief discussion and summary of our findings.

4.2. Nucleosynthesis Source Models

The first obstacle to a comparison between cosmic ray measurements and nucleosynthesis theory is determining what the theoretical results should be. Specifically, what are the abundances which are the result of "normal" nucleosynthesis? The canonical reference to which cosmic ray abundances have been compared for years has been one of the set of periodically updated versions of the "solar system" abundances of Cameron (1968, 1973, 1982b). These abundances are based mainly on measurements made on type C1 carbonaceous chondrites, with solar abundance data and some nucleosynthesis theory being used to fill in the gaps. Carbonaceous chondrite meteorites are chosen because they are believed to be the most representative of the primitive solar nebula. Recently, a new abundance compilation was published by Anders and Ebihara (1982) which is also based on type C1 carbonaceous chondrites and has a larger data base (a factor of two or more) than

that of the most recent Cameron tables. In addition, the new compilation includes estimates of the errors on the assigned abundances, a feature which has been lacking previously.

Figure 4.1 is a logarithmic plot of the even charge element abundances in the Sn-Ce region using the compilation of Anders and Ebihara along with their estimated errors. Also included on the plot are the values of Cameron (1982b). As can be seen, the agreement between the two compilations is good except for an approximately 24% decrease in the Anders and Ebihara values for tellurium ($_{52}$Te) and xenon ($_{54}$Xe) compared with those of Cameron. The value for Te has been decreased because of a systematic error in the data upon which the old value was based (see Anders and Ebihara 1982 and references therein). The decrease in Xe follows from the Te decrease because the abundance of Xe, a noble gas, is not based on actual meteorite measurements, which exhibit a great deal of variability from meteorite to meteorite, but rather on the results of a fit to the "Te-I-Cs-Ba peak". Cameron also uses a similar type of interpolation to determine his Xe abundance.

Besides the solar system abundances, we are also interested in a comparison with the results of r- and s-process nucleosynthesis. In order to separate the contributions of the s- and the r-process in the solar abundances, we must decompose them according to the scheme discussed in chapter I. Although there have been several recent decompositions (e.g. Israel *et al.* 1981, Blake and Margolis 1981, Cameron 1982a), we have chosen to use the results of Käppeler *et al.* (1982) as our model s-process. This calculation uses new and improved measurements of neutron capture cross sections of important s-only and magic number nuclei along the s-process path. In particular, ^{138}Ba, with a magic number of neutrons, is included in this group.

The σN curve of Käppeler *et al.* is the result of an s-process

Figure 4.1

A histogram of the abundances of the even charge elements in the $_{50}$Sn to $_{58}$Ce region. The vertical axis is logarithmic with the abundance of Si defined to be 10^6. The solid histogram uses the results of Anders and Ebihara (1982) while the dashed lines are the results of Cameron (1982b). The error bars are those of Anders and Ebihara.

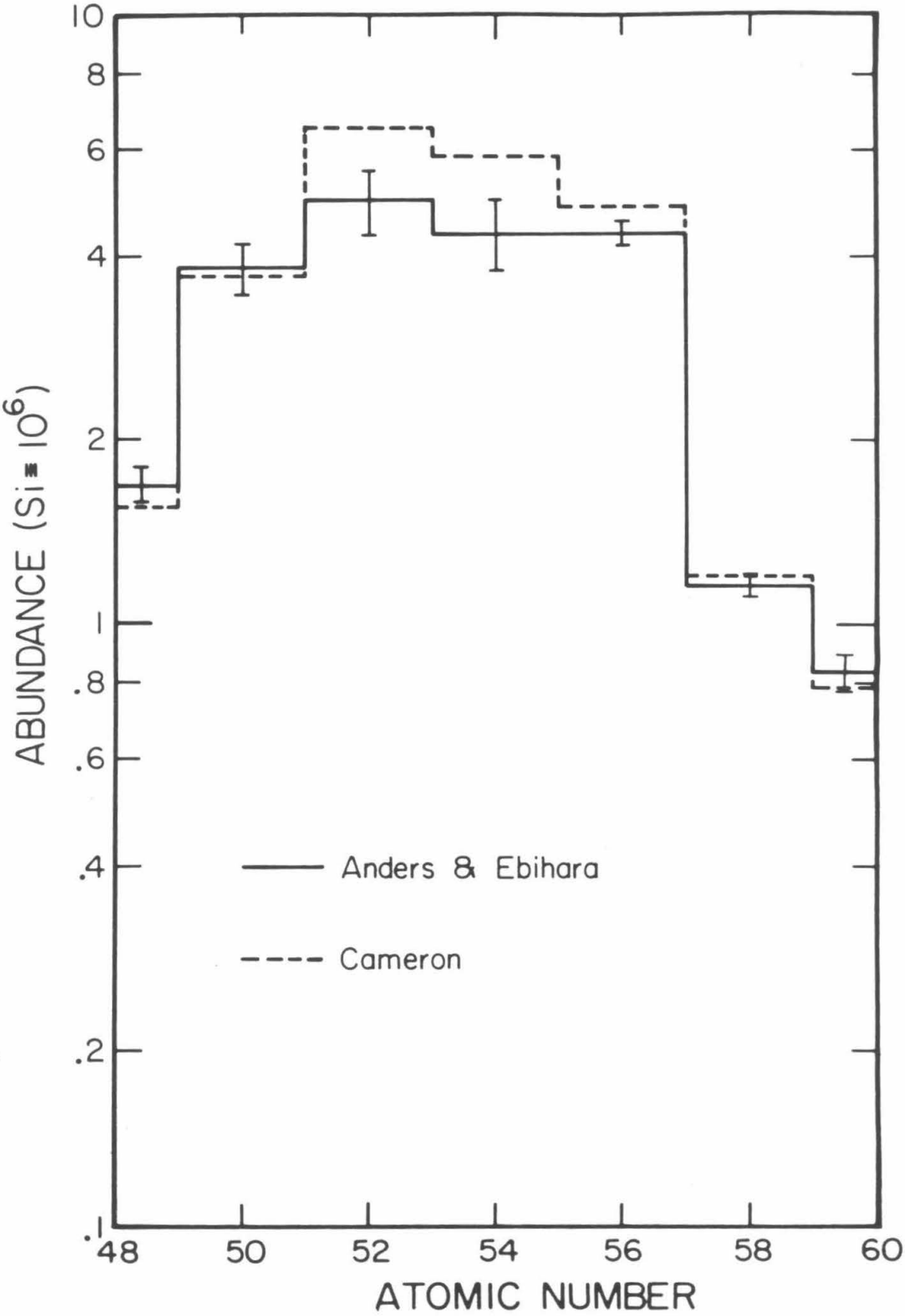
10
8
6
4
2
1
.8
.6
.4
.2
.1
ABUNDANCE (Si = 10^6)
48
50
52
54
56
58
60
ATOMIC NUMBER
Anders & Ebihara
Cameron

calculation which assumes a steady neutron flux and a two component exponential distribution of exposures. The input parameters, consisting of the fraction of iron seed nuclei exposed to the two components and the two mean values of neutron exposure, were varied to obtain a best fit to the Cameron 1982b abundances of selected s-only nuclei. Although the model was fit to the the Cameron abundances, we can still use this s-process in conjunction with the new Anders and Ebihara abundances. Figure 4.2 is a plot of the Käppeler *et al.* σN curve as a function of mass number, adapted from their paper. Indicated on the plot are the empirical values of σN for s-only and predominantly s nuclei which illustrates how well the curve fits the data. The open circles are the abundances of Cameron (1982b) multiplied by the neutron capture cross sections reported in the Käppeler *et al.* paper. The filled circles use the same neutron capture cross sections with the abundances of Anders and Ebihara. The error bars attached to the Cameron points use only the uncertainties in the cross sections (Käppeler *et al.* 1982) and do not include any abundance uncertainties. As a result similar error bars would also apply for the Anders and Ebihara points. Qualitatively, the curve appears to fit both sets of data points equally well with no gross differences. In particular, the fit in the Sn-Ba region is improved using the Anders and Ebihara abundances as a result of the decrease in the value for Te, affecting the s-only isotopes ^{122}Te, ^{123}Te, and ^{124}Te. (This decrease was actually recommended by Käppeler *et al.* in their original paper.) We note in passing that the "ledge-precipice" structure is a characteristic resulting from the "bottlenecks" at the magic number nuclei with their extremely small neutron capture cross sections.

Figure 4.3 shows the s- and r-process values in the Sn-Ce region which result from subtracting the Käppeler *et al.* s-process from the Anders and Ebihara abundances on an isotope by isotope basis. Also shown for comparison is the r-process which results if the original

Figure 4.2

A plot of the σN curve of Käppeler *et al.* (1982) along with the empirical σN product for s-only and predominantly s isotopes. The values of Cameron (1982b) are shown as the open circles with error bars which include only the neutron capture cross section uncertainties. The filled circles are the abundances of Anders and Ebihara (1982) and would have the same uncertainties. The neutron capture cross section, σ, is measured in millibarns and N, the s-process abundance, is based on the usual Si $\equiv 10^6$ scale.

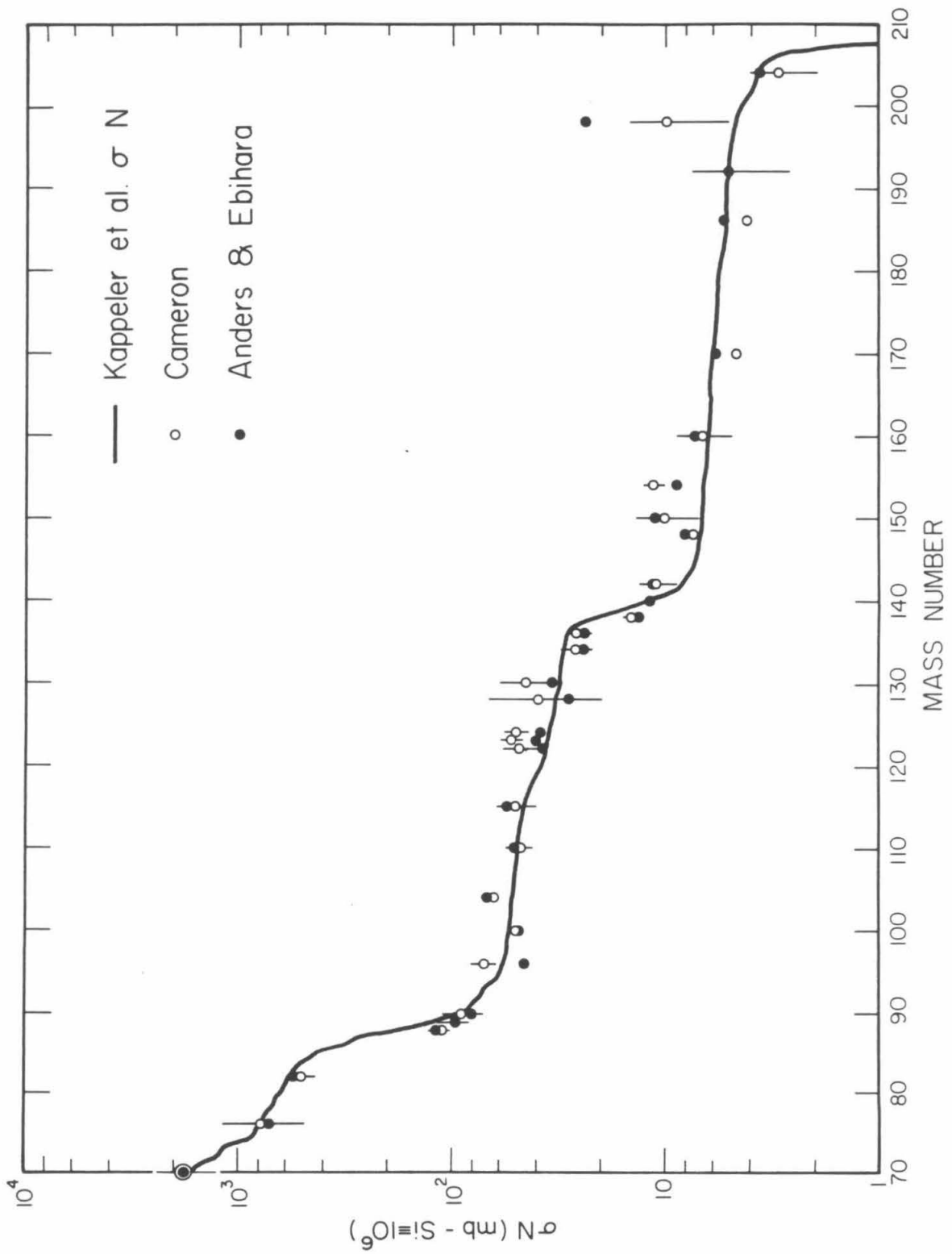
Kappeler et al. σ N
Cameron
Anders & Ebihara
σN (mb - Si≡10⁶)
MASS NUMBER
10⁴
10³
10²
10
1
70
80
90
100
110
120
130
140
150
160
170
180
190
200
210

Figure 4.3

The s-process (left) and r-process (right) components of the solar system in the $_{50}$Sn - $_{58}$Ce region using the Käppeler *et al.* s-process and subtracting it from Cameron (1982b) (dashed lines) and the Anders and Ebihara (1982) (solid lines) solar system values. The errors bars are estimates based on the uncertainties quoted in Anders and Ebihara. The p-process nuclei have been excluded in this analysis.

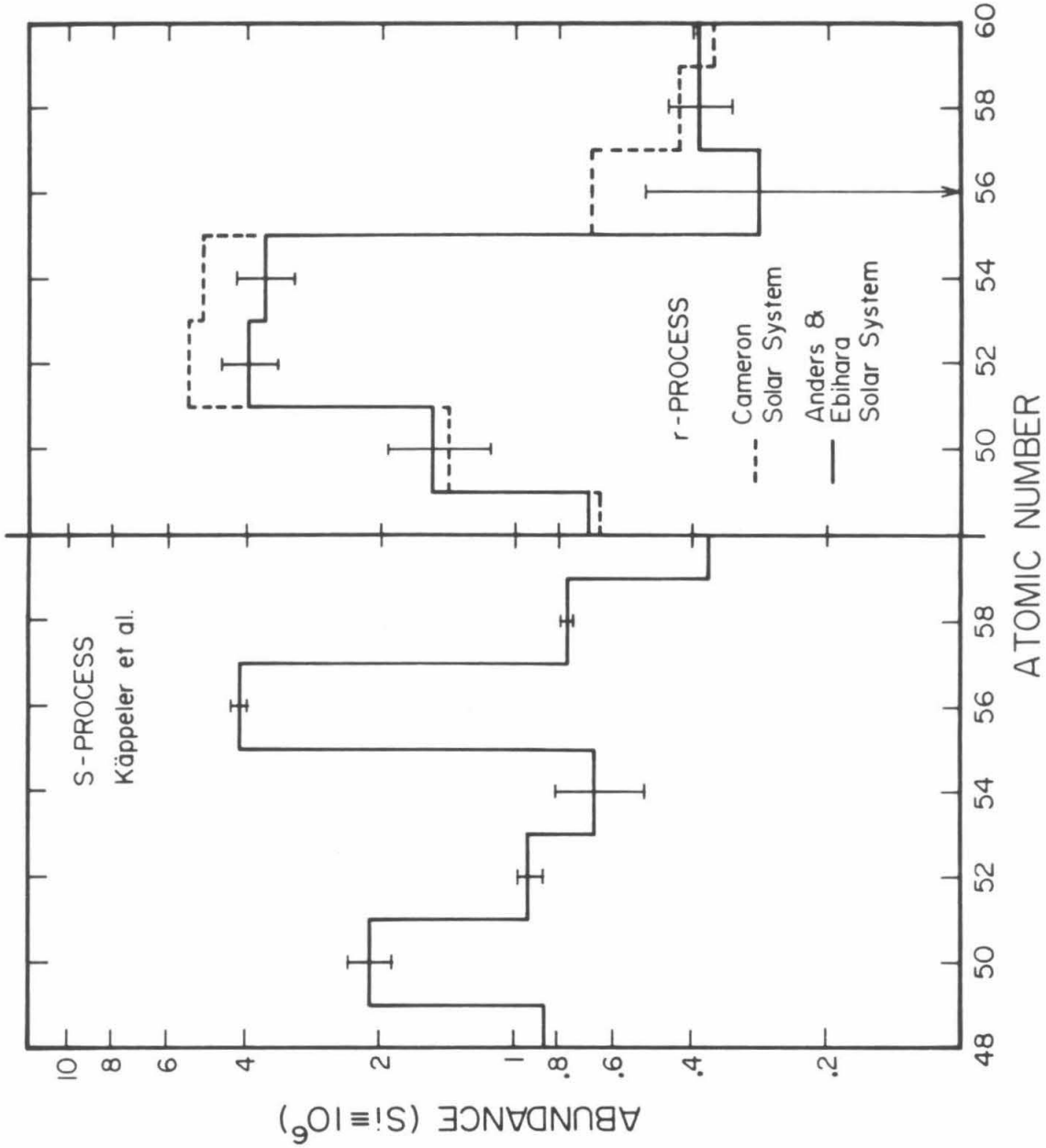
S-PROCESS
Käppeler et al.
r-PROCESS
Cameron
Solar System
Anders &
Ebihara
Solar System
ABUNDANCE (Si≡10⁶)
ATOMIC NUMBER
10
8
6
4
2
1
.8
.6
.4
.2
48
50
52
54
56
58
60

Cameron (1982b) solar system values are used (from Käppeler *et al.*). Table 4.1 shows the details of the decomposition used here for the even charge elements between $_{50}$Sn and $_{60}$Nd. Neodymium is included because it was used in calculating uncertainties later on (see section 4.4). The isotopes which could only be made in the p-process were not included in either the r- or the s-process. As a result, the sum of the r-process and the s-process does not necessarily equal the solar system value. Additionally, for the s-only isotopes, the value derived from the σN curve (Table 7 of Käppeler *et al.*), and not the actual isotopic abundance, was used. R-process abundances of these s-only nuclei were defined to be zero. The largest difference between the solar system and the sum of r- and s-process elemental abundances resulting from this procedure is 5% for Sn with the other elements having less than a 1% effect present.

Table 4.2 summarizes the elemental abundances. The uncertainties in the solar system abundances are those of Anders and Ebihara. For the s-process, in order to test the sensitivity of our results to the form of the s-process used, we have estimated the limits of variation probable by using the percentage uncertainty in the neutron capture cross section for a given isotope as the percentage uncertainty in the s-process abundance of that isotope. This is reasonable on the grounds that the s abundance of the nuclide with mass number A is determined by dividing the σN curve, which is relatively invariant, by the cross section, σ_A. A more appropriate value to use, in light of the equation for the σN curve for an exponential exposure of neutrons is the percentage uncertainty in

$$\frac{1}{\sigma_A}\left[1 + \frac{1}{\sigma_A \tau}\right]^{-1} \qquad (4.1)$$

where τ is the mean neutron exposure and is assumed to have no uncertainty here. For an exponential distribution of exposures, the

Table 4.1

Table 4.1 - $_{50}$Sn				
A	Solar System	s-process	r-process	% error
112	0.0386	-	-	-
114	0.0256	-	-	-
115	0.0145	-	-	-
116	0.565	0.458	-	20 [a]
117	0.296	0.105	0.191	7 [b]
118	0.929	0.655	0.274	8 [b]
119	0.329	0.156	0.173	15 [b]
120	1.24	0.749	0.49	30 [b]
122	0.174	-	0.174	-
124	0.215	-	0.215	-
Total	3.82	2.123	1.52	-

Percentage uncertainties apply to the s-process abundances.

[a] Käppeler *et al.* (1982)

[b] Allen, Gibbons, and Macklin (1971)

[c] Uncertainty of 30% adopted (50% for Xe) - see text.

[d] Uncertainty in (4.1) used with

$\tau = 0.092\ \text{mb}^{-1}$

$\sigma_{^{136}Ba} = 4.22 \pm 0.25\text{mb}$

$\sigma_{^{140}Ce} = 11.5 \pm 0.6\text{mb}$

(Käppeler *et al.* 1982).

Table 4.1 - $_{52}$Te				
A	Solar System	s-process	r-process	% error
120	0.0045	-	-	-
122	0.123	0.121	-	20 [a]
123	0.044	0.0401	-	10 [a]
124	0.226	0.211	-	12 [a]
125	0.344	0.0823	0.262	7 [b]
126	0.918	0.474	0.444	10 [b]
128	1.56	-	1.56	-
130	1.69	-	1.69	-
Total	4.91	0.928	3.96	-

Table 4.1 - $_{54}$Xe				
A	Solar System	s-process	r-process	% error
124	0.00496	-	-	-
126	0.00483	-	-	-
128	0.0939	0.108	-	50 [a]
129	1.20	0.0603	1.14	50 [c]
130	0.189	0.176	-	30 [a]
131	0.941	0.0619	0.879	50 [c]
132	1.15	0.254	0.90	50 [c]
134	0.421	-	0.421	-
136	0.34	-	0.34	-
Total	4.35	0.660	3.68	-

Table 4.1 - $_{56}$Ba				
A	Solar System	s-process	r-process	% error
130	0.00462	-	-	-
132	0.00440	-	-	-
134	0.106	0.131	-	16 [a]
135	0.287	0.0627	0.224	30 [c]
136	0.342	0.359	-	14 [a]
137	0.488	0.446	0.042	30 [c]
138	3.13	3.11	0.02	1.6 [d]
Total	4.36	4.11	0.29	-

Table 4.1 - $_{58}$Ce				
A	Solar System	s-process	r-process	% error
136	0.0022	-	-	-
138	0.0029	-	-	-
140	1.026	0.765	0.261	2.7 [d]
142	0.129	-	0.129	-
Total	1.16	0.765	0.390	-

Table 4.1 - $_{60}$Nd				
A	Solar System	s-process	r-process	% error
142	0.227	0.151	-	19 [a]
143	0.101	0.0292	0.072	30 [c]
144	0.199	0.112	0.087	30 [c]
145	0.0694	0.0158	0.0536	30 [c]
146	0.144	0.0607	0.083	30 [c]
148	0.0477	-	0.0477	-
150	0.0468	-	0.0468	-
Total	0.835	0.369	0.390	-

Table 4.2

Source Abundances (Si ≡ 10^6)

Element	Solar System	s-process	r-process
$_{50}$Sn	3.82 ± 9.4%	2.123 ± 12%	1.52 ± 25%
$_{52}$Te	4.91 ± 12%	0.928 ± 6.4%	3.96 ± 14%
$_{54}$Xe	4.35 ± 13%	0.660 ± 23%	3.68 ± 15%
$_{56}$Ba	4.36 ± 4.5%	4.11 ± 3.8%	0.29 ± 78%
$_{58}$Ce	1.16 ± 5.1%	0.765 ± 2.7%	0.390 ± 16%
$_{60}$Nd	0.835 ± 7.0%	0.369 ± 13%	0.390 ± 15%

abundance of the nuclide with mass number A along the s-process path is proportional to

$$\frac{1}{\sigma_A} \prod_{i=56}^{A} \left[1 + \frac{1}{\sigma_i \tau}\right]^{-1} \qquad (4.2)$$

with σ_i the neutron capture cross section of the nuclide with mass number i along the s-process path. (e.g. see Käppeler *et al.* 1982). Since we are interested only in the uncertainties in the nuclide's relative abundance, we ignore the uncertainty from all terms in the product which are common among the nuclei under consideration leaving only the term (4.1). The use of (4.1) is only important for the magic number nuclei where $\sigma_A \tau < 1$. We have calculated the uncertainties in the isotopes ^{138}Ba and ^{140}Ce using (4.1). For all the others we used the uncertainty in σ_A alone. The isotopic uncertainties assumed are listed in Table 4.1 in the last column. The values are of three types. For those listed in Käppeler *et al.*, we used their uncertainty. For those uncertainties not listed in Käppeler *et al.* we used the uncertainties listed in Allen *et al.* (1971) since, for a number of the nuclei, the cross sections were equal to the values inferred from the σN - N table in Käppeler *et al.* For those cross sections where neither compilation listed uncertainties we used the minimum value of 30% suggested by Käppeler *et al.* except for Xe where 50% seemed more appropriate on the basis of the listed uncertainties. The uncertainties in the r-process are just the uncertainties in the s-process and solar system values added in quadrature for the isotopes involved.

4.3. Preferential Acceleration

A further complication to the determination of the cosmic ray source abundances arises from possible preferential acceleration effects. Comparisons of the derived cosmic ray source abundances with solar system abundances show indications of a possible first ionization potential effect of the type discussed in Cassé and Goret (1978) and references therein. Those elements having a low first ionization potential also have enhancements in the ratio of cosmic ray source abundance to solar system abundance which may be indicative of the preferential acceleration of those elements easiest to ionize.

Figure 4.4 is a plot of the ratio of the cosmic ray source abundance to the solar abundance as a function of the first ionization potential as taken from Brewster, Freier, and Waddington (1983). The ratio is defined to be 1 for Fe. It can be seen that there is a definite, but not perfect, correlation between the two quantities. The work of Cassé and Goret was based only on results in the charge region below iron. Nevertheless, results in the charge 26 to 40 region (Binns *et al.* 1982) have shown that this correlation seems to be present for the higher charges also. Both sets of data are included in the figure.

The actual form of the first ionization potential dependence has not been fully established. Some models involve a step function with the effect being discontinuous at a value of ~ 9 eV. Others use an exponential dependence. But even here the numerical values used in the function depend on what range of ionization potentials is used for the fit. In particular, the two exponentials indicated on the figure by the straight lines are results obtained both with and without including the high first ionization potential elements He and Ne. For our comparison, we have used the "FIP1" form of Brewster *et al.*

$$R = 9.31 \exp\left[-0.288I(eV)\right] \qquad (4.3)$$

Figure 4.4

Plot of the ratio of the cosmic ray source abundance to the solar system abundance as a function of the first ionization potential of the element. Also shown are two possible fits to the trend in the data. From Brewster, Freier, and Waddington (1983).

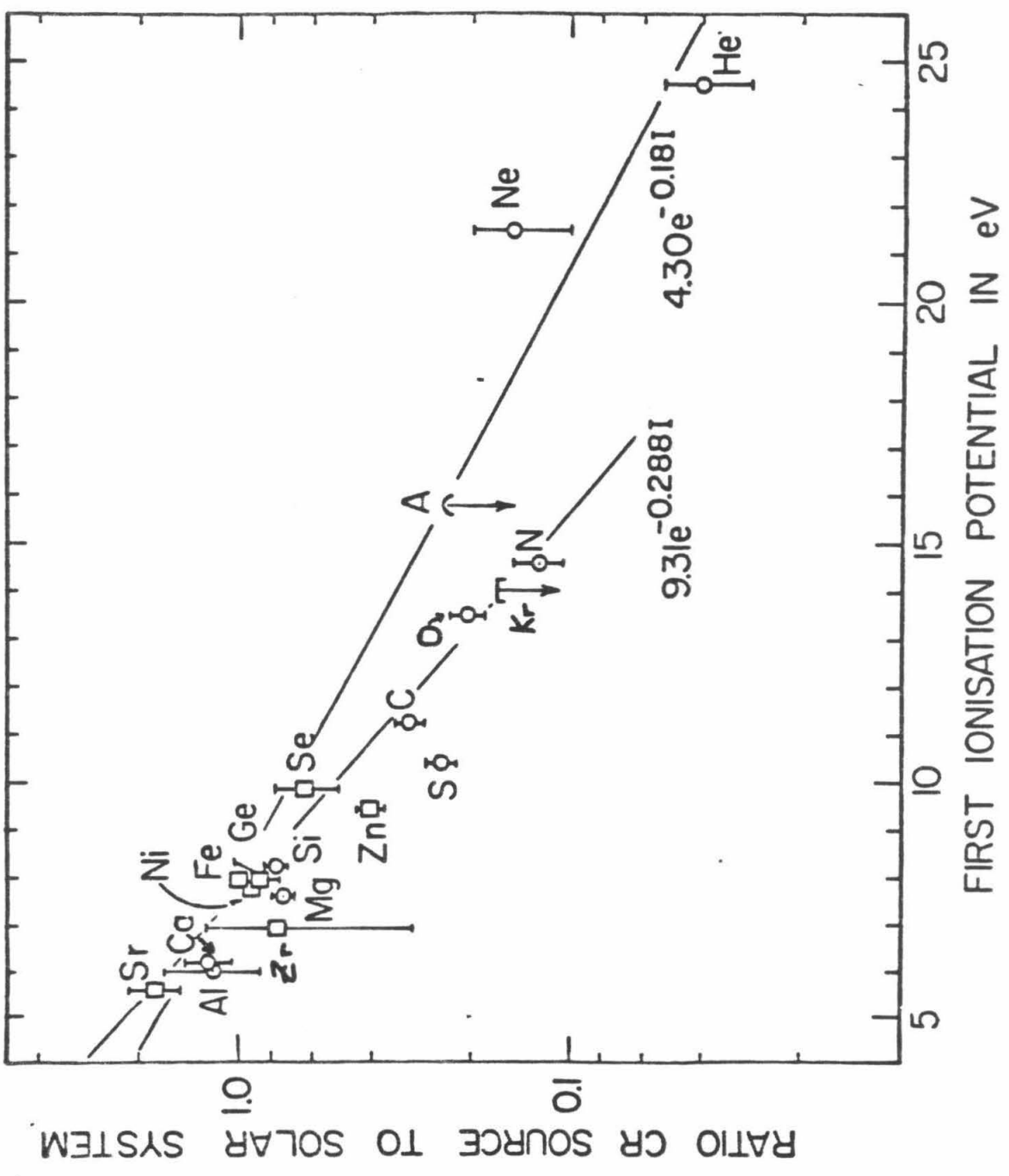
RATIO CR SOURCE TO SOLAR SYSTEM
0.1
1.0
5
10
15
20
25
FIRST IONISATION POTENTIAL IN eV
Sr
Ca
Al
Ni
Fe
Mg
Si
Ge
Se
Zn
S
C
O
Kr
N
A
Ne
He
$9.31e^{-0.288I}$
$4.30e^{-0.18I}$

which was chosen to fit the data with first ionization potential, I, between 5 and 15 eV. R is the ratio of cosmic ray source to solar system. Table 4.3 shows, for the even elements in the Sn-Ce region, the values of R given by this fit along with the first ionization potentials assumed. In order to assess the sensitivity of our results to this effect, we have adopted an uncertainty of 15% for FIP adjustments.

4.4. Cosmic Ray Propagation

Another important effect which alters the abundances observed at earth is due to cosmic ray propagation. As the cosmic rays pass through the interstellar medium, they undergo nuclear interactions with the H and He of which it is primarily composed. These interactions have the effect of reducing the flux of the more abundant nuclei by spallation and of increasing the flux of the rarer nuclei with the fragments of the more abundant ones. For this study, we use the propagation calculations of Brewster, Freier, and Waddington (1983). These calculations model the cosmic ray propagation effects using matrix methods and the "leaky box" formalism of Cowsik *et al.* (1967). In the steady state leaky box model, the observed flux of cosmic ray species i is related to its rate of production at the source by the continuity equation (e.g. Stone and Wiedenbeck 1979)

$$0 = q_i + \sum_j \frac{\Phi_j}{\lambda_{ij}} - \frac{\Phi_i}{\lambda_i} \qquad (4.4)$$

where Φ_i is the observed flux of species i, q_i is its rate of production at the source, λ_i is the total interaction length of species i, λ_{ij} is the interaction length for production of species i from species j, and the sum over j is over all species able to fragment into i. We have ignored energy losses in (4.4). The model is essentially an equilibrium calculation in which nuclear fragmentation and decay, along with escape from the

Table 4.3 FIP Values		
Element	I(eV)	R(FIP1)
$_{50}$Sn	7.34	1.12
$_{52}$Te	9.01	0.695
$_{54}$Xe	12.13	0.283
$_{56}$Ba	5.21	2.08
$_{58}$Ce	5.60	1.86
$_{60}$Nd	5.50	1.91

Ionization potentials and FIP1 from Brewster (private communication and Brewster, Freier, and Waddington 1983).

galaxy, deplete the source nuclei, which are simultaneously being replenished both by fragmentation of higher mass nuclei and by a continuously operating source. Since it is a steady state model, q_i and Φ_i are respectively proportional to the abundances of species i at the source and as observed at earth. For details of the Brewster, Freier, and Waddington calculation one is referred to their article. A few points deserve mention here, however. First, no account is taken of energy loss during transport in their calculation, which should be valid for the energies of 2 GeV/nucleon and higher that we are working with. Second, the cosmic rays are considered to have a mean escape length of 5.5 g cm^{-2} in an interstellar medium composed of pure H. This results in an exponential distribution of pathlengths with this same mean. Finally, although a complete propagation involves isotopes and not elements, because of the large number of possible nuclides to consider, this calculation uses interaction cross sections weighted according to the assumed source isotopic composition and propagates elements only.

Table 4.4 lists the results of propagating the various sources discussed in section 4.1 (Brewster, private communication). The propagation included all the elements with $Z \geq 50$ (see Appendix B). The values for the s-process are not the results of an actual propagation but were derived by subtracting the propagated r-process elemental abundances from those of the propagated solar system. Although this procedure is not exact, any errors made should be small compared to the uncertainties involved. The quoted error limits are estimates based on the source and propagation uncertainties (Table 4.2 source abundance uncertainties were used. FIP values include a 15% uncorrelated uncertainty in the FIP source adjustments). For calculating errors, a simple model of the form

$$\Phi_i = \lambda_i q_i + \frac{\lambda_i \lambda_j}{\lambda_{ij}} q_j \qquad (4.5)$$

Table 4.4
Propagated Fluxes (Arbitrary Units)

NO FIP

Element	Solar System		s-process		r-process	
$_{50}$Sn	7.45 ± 16%	(0.58)	3.83 ± 15%	(0.62)	3.62 ± 22%	(0.47)
$_{52}$Te	6.66 ± 13%	(0.79)	1.76 ± 18%	(0.57)	4.90 ± 14%	(0.87)
$_{54}$Xe	5.66 ± 13%	(0.81)	1.54 ± 20%	(0.45)	4.12 ± 16%	(0.94)
$_{56}$Ba	5.25 ± 7.7%	(0.86)	4.505 ± 6.4%	(0.94)	0.745 ± 38%	(0.40)
$_{58}$Ce	1.47 ± 8.9%	(0.81)	0.882 ± 6.7%	(0.89)	0.588 ± 16%	(0.68)

FIP

Element	Solar System		s-process		r-process	
$_{50}$Sn	8.02 ± 19%	(0.60)	4.64 ± 19%	(0.57)	3.38 ± 23%	(0.57)
$_{52}$Te	5.27 ± 18%	(0.70)	1.81 ± 26%	(0.38)	3.46 ± 19%	(0.86)
$_{54}$Xe	3.36 ± 23%	(0.39)	1.74 ± 31%	(0.11)	1.62 ± 31%	(0.68)
$_{56}$Ba	10.4 ± 15%	(0.90)	9.16 ± 16%	(0.96)	1.24 ± 44%	(0.50)
$_{58}$Ce	2.56 ± 15%	(0.86)	1.584 ± 15%	(0.92)	0.976 ± 20%	(0.76)

Propagated values from Brewster, private communication. See also Brewster, Freier, and Waddington (1983). The number in parentheses is the fraction of the observed abundance assumed to be surviving primary.

was assumed. In (4.4), if Φ_j has no contribution from the secondary component, the summation term, then we have

$$\Phi_j = \lambda_j q_j \tag{4.6}$$

and Φ_j is all surviving primary, i.e. no secondaries. This is approximately true for Bi which has no abundant elements above it on the charge scale. For an element i for which j is the major secondary contributor, we can ignore all terms other than j in the secondary sum and substitute $\lambda_j q_j$ for Φ_j giving us (4.5). In making this approximation we thus ignore the contributions made to element i from all other elements except the source, or primary, component of j. It was assumed that the total interaction cross sections could have an average error of 5% (Letaw *et al.* 1983) and that the partial cross sections had uncertainties of 30% (although they could be in error by as much as 50%, see e.g. Brewster, Freier, and Waddington, 1983). Additionally, in the calculation of the uncertainty contributed by the fragments from higher charges to the observed flux, approximated by the second term above, the uncertainty of the next higher charge even element was used under the assumption that it was the main contributor. The number in parentheses for each entry is the fraction of the observed flux attributed to the surviving primary

4.5. Comparison of the Data with the Models

Figure 4.5 is a comparison between the results of this study and the propagated even element fluxes in the Sn-Ce charge region. No first ionization potential adjustments have been applied to the sources and all the model distributions have been normalized so that the abundance of $_{52}$Te is defined to be one. Because we have constrained our analysis to a limited charge region, we are able to vary the normalization between the model and the data to obtain a "best fit", defined here as a minimum in the χ^2, for the five elements under consideration, $_{50}$Sn, $_{52}$Te, $_{54}$Xe, $_{56}$Ba,

Figure 4.5

Comparison of the data with the results of propagating a solar system type source, a pure s-process source, and a pure r-process source derived from the abundances of Anders and Ebihara (1982) and the s-process of Käppeler *et al.* (1982).

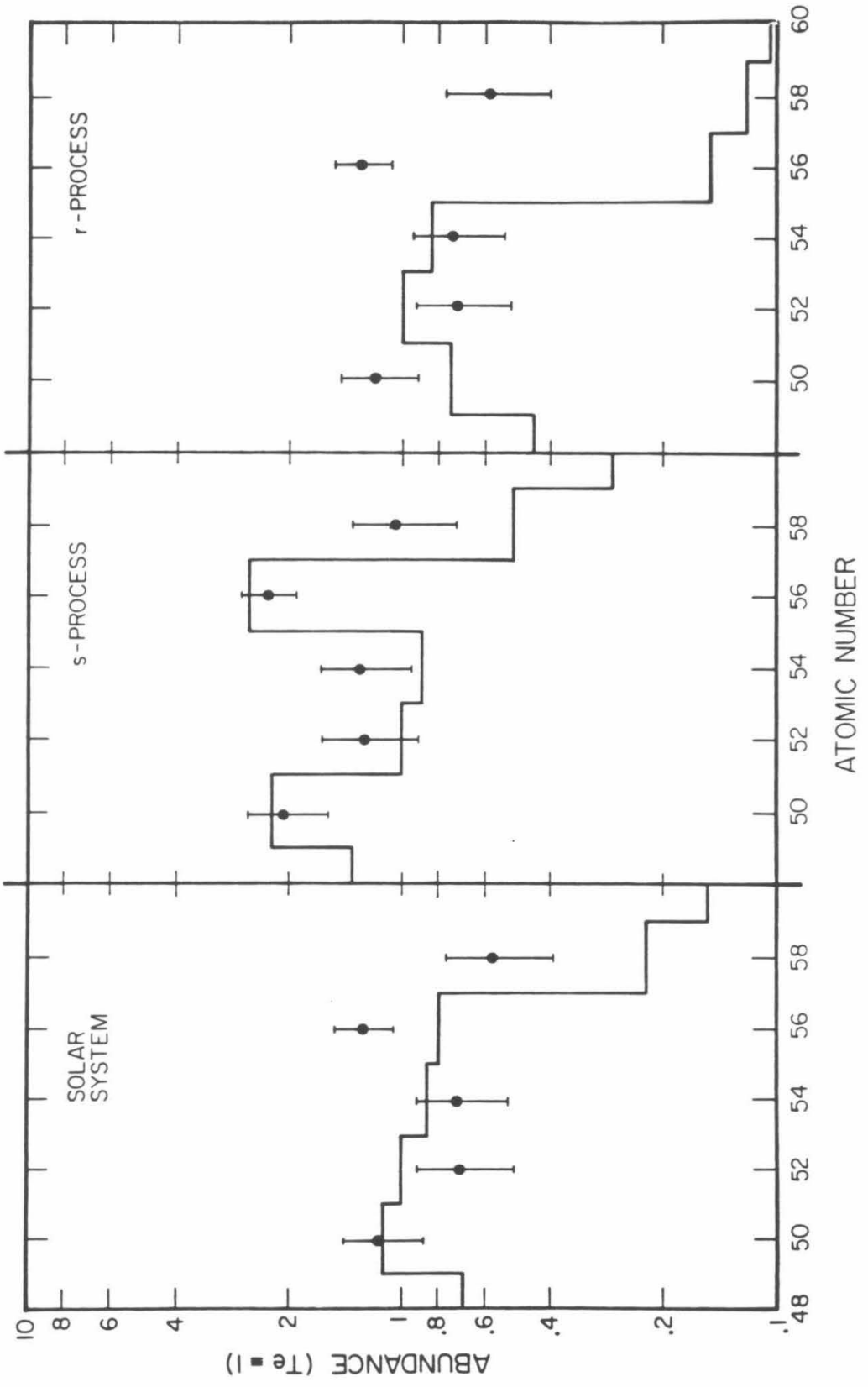
SOLAR SYSTEM
s-PROCESS
r-PROCESS
ABUNDANCE (Te = 1)
ATOMIC NUMBER
10
8
6
4
2
1
.8
.6
.4
.2
.1
48
50
52
54
56
58
60

and $_{58}$Ce. The adjustment of the normalization means that the χ^2 has four degrees of freedom. The data are shown with this best fit normalization applied. Note that the vertical scale is logarithmic. The χ^2 calculation and the error bars indicated on the data do not include the source uncertainties, only those due to the data points, although, as will be seen later, this does not change the nature of the results presented here.

The three panels show, from left to right, the results of propagating solar system, pure s-process, and pure r-process sources. Note that best agreement seems to be with the pure s-process source if no first ionization potential biases are included. Table 4.5 shows the χ^2 values and the probability of obtaining a χ^2 that high or higher by chance.

Figure 4.6 is the same as figure 4.5 except that the sources have had first ionization potential (FIP) adjustments applied before propagation. In this case, the best fit is obtained for a solar system mixture of r- and s-process material with a χ^2 of 3.99 for four degrees of freedom, which corresponds to a 40.6% probability of occurring by chance. The values for the other sources are shown in Table 4.5 under FIP.

Although the previous figures make a pure r-process source highly unlikely on the basis of our measurement, it does not rule out the possibility that a significant fraction of the cosmic ray source may be the result of r-process synthesis. In order to examine this question, we have looked at the χ^2 as a function of the relative amounts of r- and s-process material present at the source by constructing the composite abundance distribution X_i.

$$X_i = fS_i + (1-f)R_i \tag{4.7}$$

where S_i denotes the s-process abundance of element i, R_i denotes its r-process abundance, and f is a parameter which varies from 0 to 1. If the

Table 4.5

χ^2_{min} Values

	r-process		Solar System		s-process	
NO FIP	39.59	(<0.00001%)	11.84	(1.9%)	5.32	(25.6%)
+ERRORS	38.45	(<0.00001%)	11.61	(2.1%)	5.24	(26.4%)
FIP	24.37	(0.007%)	3.99	(40.6%)	15.58	(0.36%)
+ERRORS	18.65	(0.093%)	3.50	(47.8%)	7.63	(10.6%)

"+ ERRORS" includes uncertainties in the source abundances and propagation uncertainties. Numbers in parentheses are the probability of obtaining a χ^2 that high or higher by chance.

Figure 4.6

Comparison of the data with the results of propagating a solar system type source, a pure s-process source, and a pure r-process source derived from the abundances of Anders and Ebihara (1982) and the s-process of Käppeler ***et al.*** (1982) and adjusted for first ionization potential effects as discussed in the text.

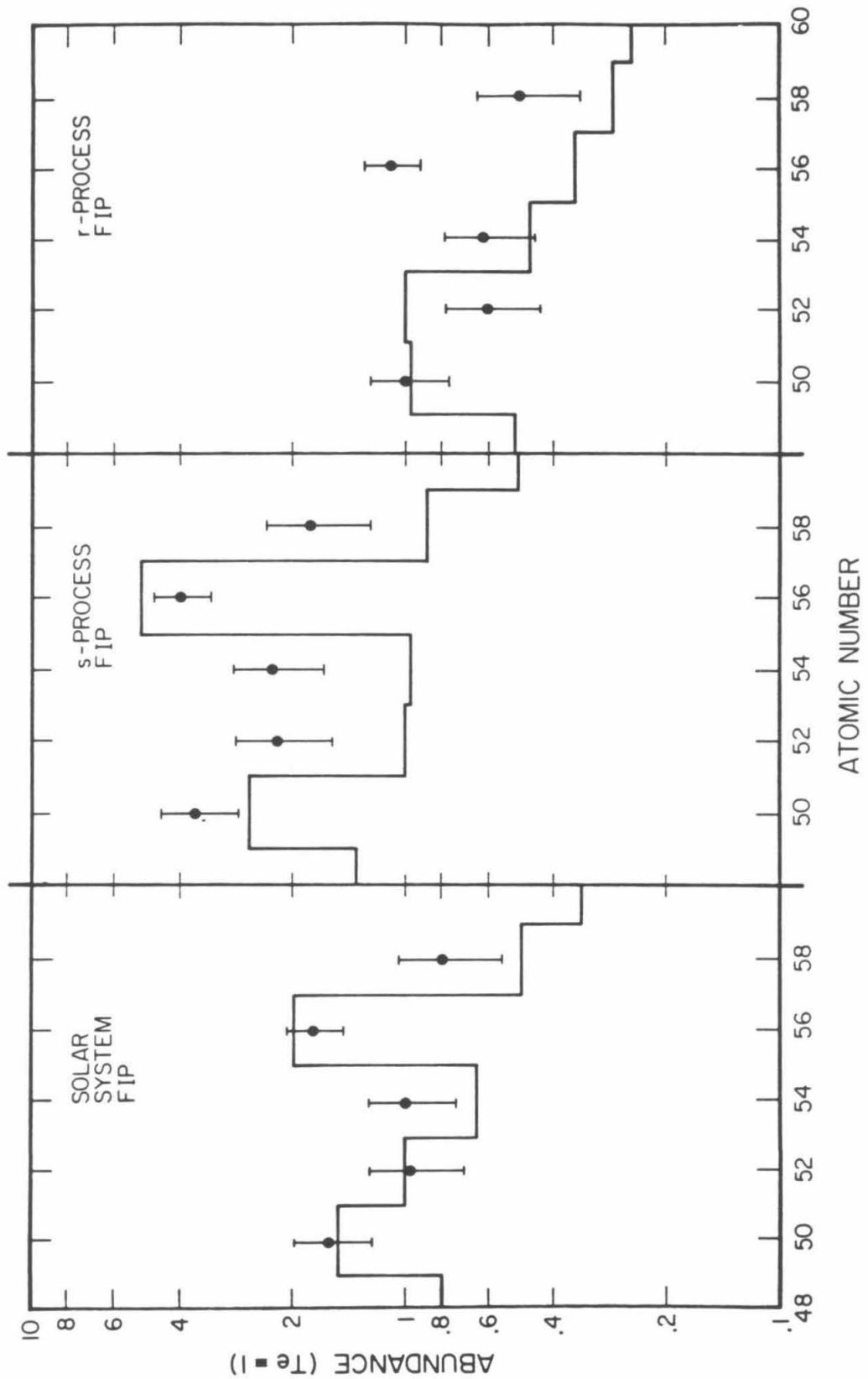
SOLAR SYSTEM FIP
s-PROCESS FIP
r-PROCESS FIP
ABUNDANCE (Te = 1)
ATOMIC NUMBER
10
8
6
4
2
1
.8
.6
.4
.2
.1
48
50
52
54
56
58
60

S_i have the correct ratios to each other for the s-process and the R_i have the correct ratios for the r-process, then the resultant X_i represents a mixture whose relative elemental abundances vary from pure r-process to pure s-process as f goes from 0 to 1. In particular, if we chose the S_i and R_i of Table 4.4, then if f = 0.5

$$X_i = 0.5\ (R_i + S_i) \tag{4.8}$$

and we have the solar system distribution to within a normalization factor. Since we will only be concerned with the relative abundances of the elements in this region, the added factor of 0.5 is inconsequential. A parameter that is more physically meaningful than f is

$$\eta = \frac{1 - f}{f} = \frac{(r/s)_{X_i}}{(r/s)_{SS_i}} \tag{4.9}$$

where the second equality, the ratio of r-process to s-process material in X_i compared with the same ratio in the solar system, follows if R_i and S_i are chosen from Table 4.4, i.e. so that $SS_i = R_i + S_i$ where SS_i are the solar system abundances. When f = 0.5, $\eta = 1$ and the distribution contains the same fraction of s- and r- process material as does the solar system. If f = 0.4, the X_i distribution contains $\eta = 1.5$ times the solar ratio of r- to s-process material.

Although the above formalism will work for the source distributions, it is not immediately obvious than one can do the same for the propagated fluxes. However, since the propagation operation is, in essence, a matrix multiplication, a linear combination of sources is the same linear combination of propagated fluxes. This is only true exactly if one is working with isotopes because the isotopic cross sections for a given element are not all equal and, since the isotopic as well as the elemental abundances vary, this means that the elemental cross section are a function of f in the Brewster, Freier, and Waddington propagation and

therefore so are the matrix elements. Nevertheless, the dependence on f is weak in the weighted cross sections used, generally showing variations of less than 5% from pure r-process to pure s-process material (Brewster, private communication). As a result, the errors should not be significant here.

Using the above formalism, the χ^2 was found for each value of f between 0 and 1 in the same manner as described previously, i.e. using the best fit normalization. Figure 4.7 is the result for the case where no FIP adjustments were applied. The pure r-process is at the left, the solar system at f = 0.5, and the pure s-process at the right. The left hand scale indicates the χ^2 values with selected χ^2 significance levels indicated by the labeled dashed lines. As can be seen from the figure, the best fit is for an f of 0.83 which corresponds to an r-process to s-process ratio of 0.20 times that of the solar system. The $\chi^2 + 1$ uncertainties on this quantity are 0.725 to 0.945 in f, corresponding to an r- to s-process ratio which is from 5.8% to 38% of the solar system value. If we include the errors on the propagated sources listed in Table 4.4, the results are essentially unchanged (Table 4.5 "NO FIP + ERRORS"). The χ^2 curve, to within the accuracy depicted, is the same for the range shown. The pure r-process χ^2 drops from 39.6 to 38.4, still a significant difference at the greater than 99% level. This relative insensitivity to the model uncertainties implies that the data errors dominate the calculation. The absolute uncertainty on the Sn point, for example, changes only from 0.38 to approximately 0.42 if the r-process, best fit errors are added in quadrature. The Ba uncertainty remains unchanged.

We can do the same calculation for the FIP adjusted sources. These results are shown in Figure 4.8. The format is the same as in Figure 4.7 with the solid curve indicating the χ^2 value when only the data point errors are considered. The dashed curve results if the uncertainties in the propagation model are included (Table 4.4). This greater sensitivity

Figure 4.7

χ^2 of the fit between the data and a given mixture of r and s-process material as a function of the mixing parameter, f. Solar system material corresponds to f = 0.5 while a pure r-process corresponds to f = 0 and a pure s-process to f = 1.

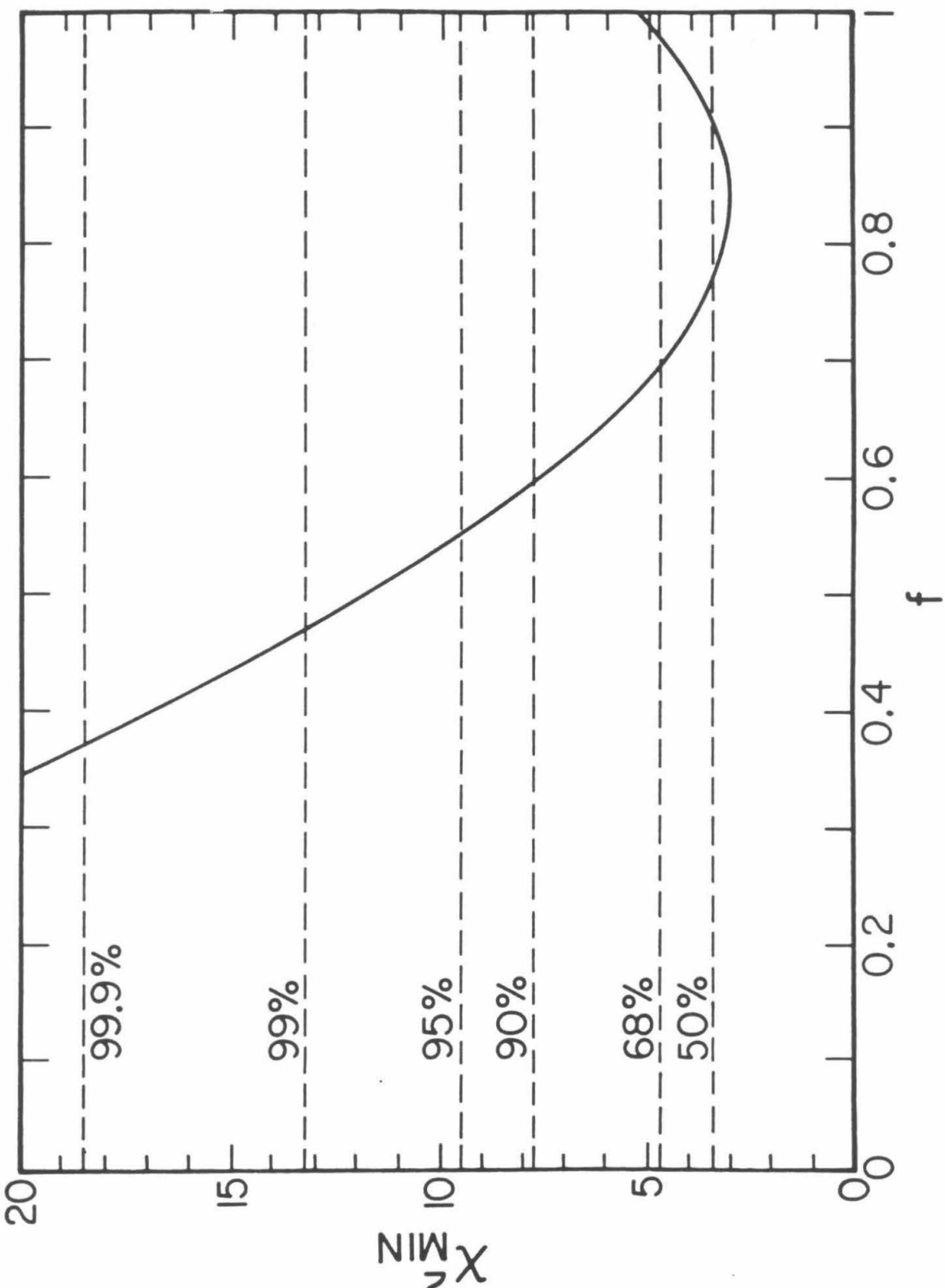
χ^2_{MIN}
20
15
10
5
0
0
0.2
0.4
0.6
0.8
1
f
99.9%
99%
95%
90%
68%
50%

Figure 4.8

χ^2 of the fit between the data and a given mixture of r and s-process FIP adjusted material as a function of the mixing parameter, f. Solar system material corresponds to f = 0.5 while a pure r-process corresponds to f = 0 and a pure s-process to f = 1. The solid curve includes only the data uncertainties. The dashed curve includes uncertainties in the model as presented in Table 4.4.

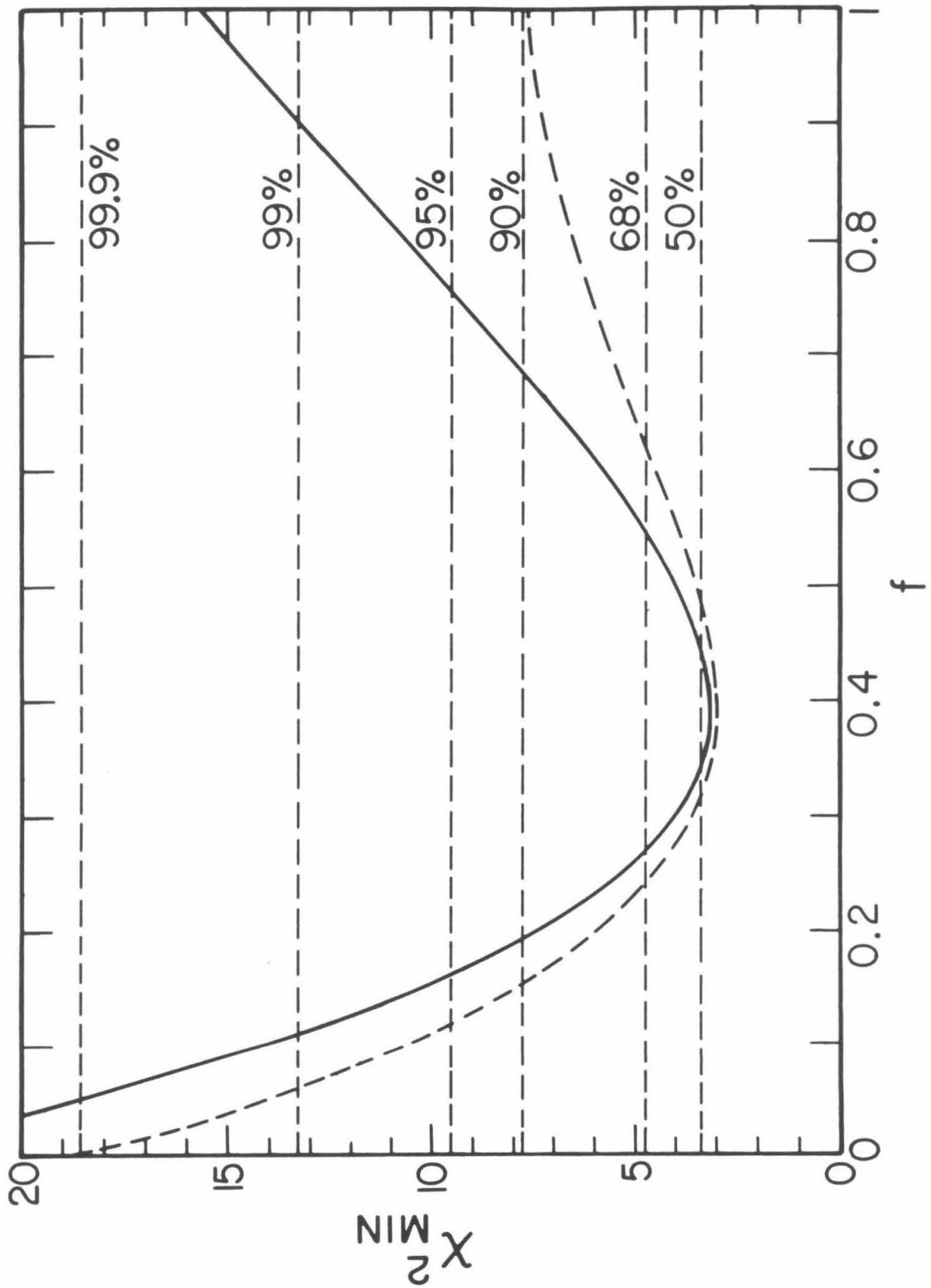
99.9%
99%
95%
90%
68%
50%
0
0.2
0.4
0.6
0.8
1
f
0
5
10
15
20
χ^2_{MIN}

of the calculated χ^2 to the uncertainties on the model is mainly the result of the FIP adjustment increasing the Ba abundance by a factor of approximately 2, resulting in larger absolute uncertainties in this quantity. Nevertheless, the general character of the curve does not change. The minimum in both cases occurs at 0.40 which is an r-process enrichment of 1.50 over the solar system value. Again, the $\chi^2 + 1$ uncertainty limits are 0.28 to 0.55 in f or 2.6 to 0.82 in η. (If we consider only the data errors, these limits become 0.30 to 0.51 for f and 2.3 to 0.96 in η).

The sensitivity of the calculation to the different element abundances is indicated by Figures 4.9 and 4.10. In these, the quantity

$$\Delta_i = \frac{D_i - X_i}{\sigma_i} \qquad (4.10)$$

is plotted as a function of f. Here, X_i is the r-s combination for element i with the best-fit normalization applied, D_i is the data value, and σ_i is the uncertainty in D_i. For the illustrated curves, σ_i includes only the data errors. Each curve is labeled with the appropriate element. Figure 4.9 addresses the non-FIP case, while Figure 4.10 applies for the FIP adjusted values. Note that in both cases Ba shows the greatest degree of variation and that, additionally, a value of f can be found for which all elements are in reasonable agreement with the theory, as could be expected from the χ^2 analysis. Cerium is the only element which remains significantly overabundant both with and without FIP. However, the effect is less than two sigma for all acceptable values of χ^2 and is therefore marginal at best.

Another, slightly different, way of viewing the data can be seen in Figure 4.11. In this diagram, the ratio of Ba to Te is plotted against the ratio of Sn to Te. Since Sn and Ba are both primarily s-process elements, while Te is primarily r-process, this plot is effectively a display of the correlation between these two measurements of the amount of r-

Figure 4.9

Contributions to the χ^2 for each element as a function of the mixing parameter f discussed in the text. No first ionization potential adjustments were applied.

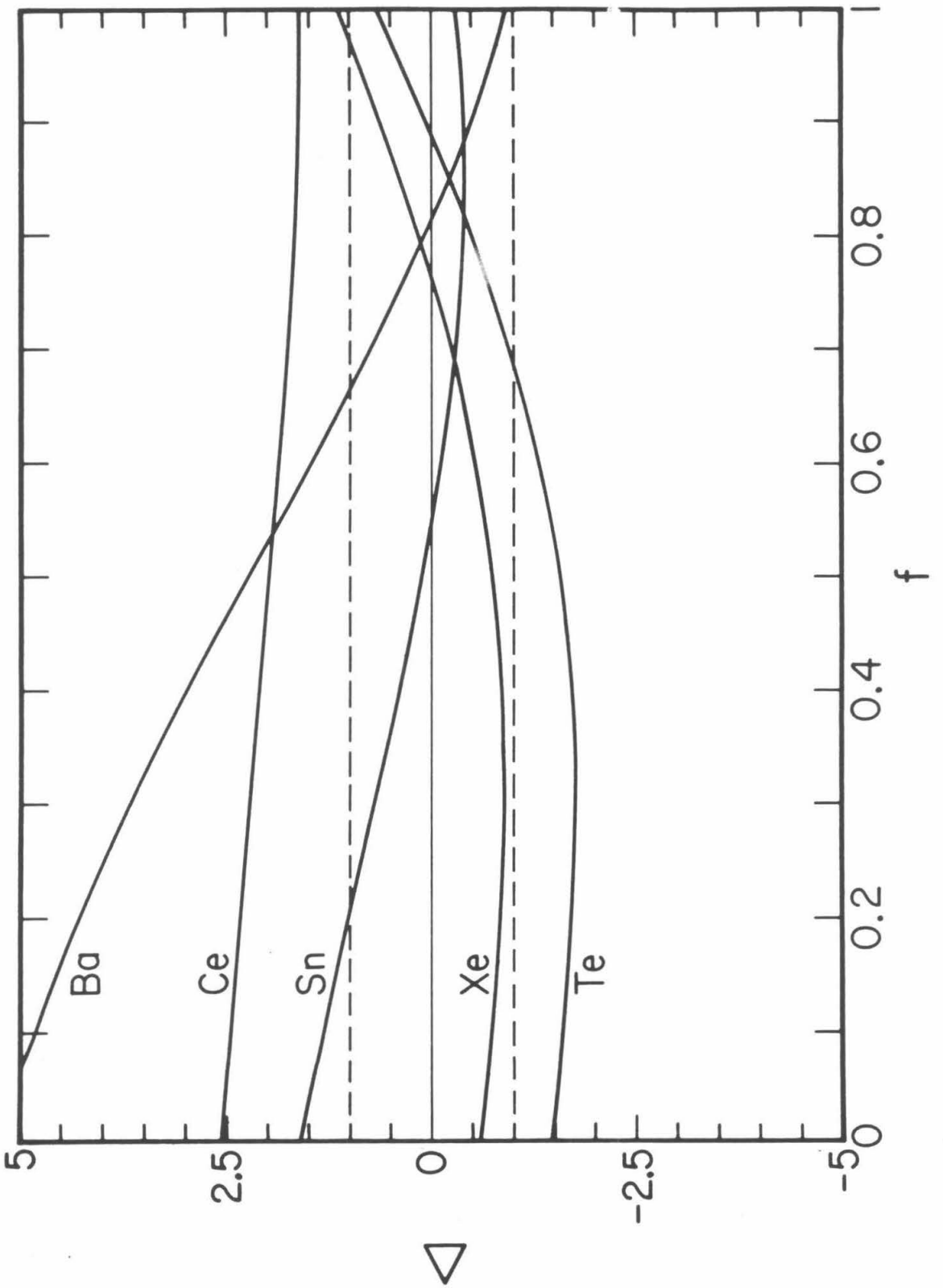
Ba
Ce
Sn
Xe
Te
5
2.5
0
-2.5
-5
0
0.2
0.4
0.6
0.8
f
▽

Figure 4.10

Contributions to the χ^2 for each element as a function of the mixing parameter f discussed in the text. Source abundances were altered according to first ionization potential biases.

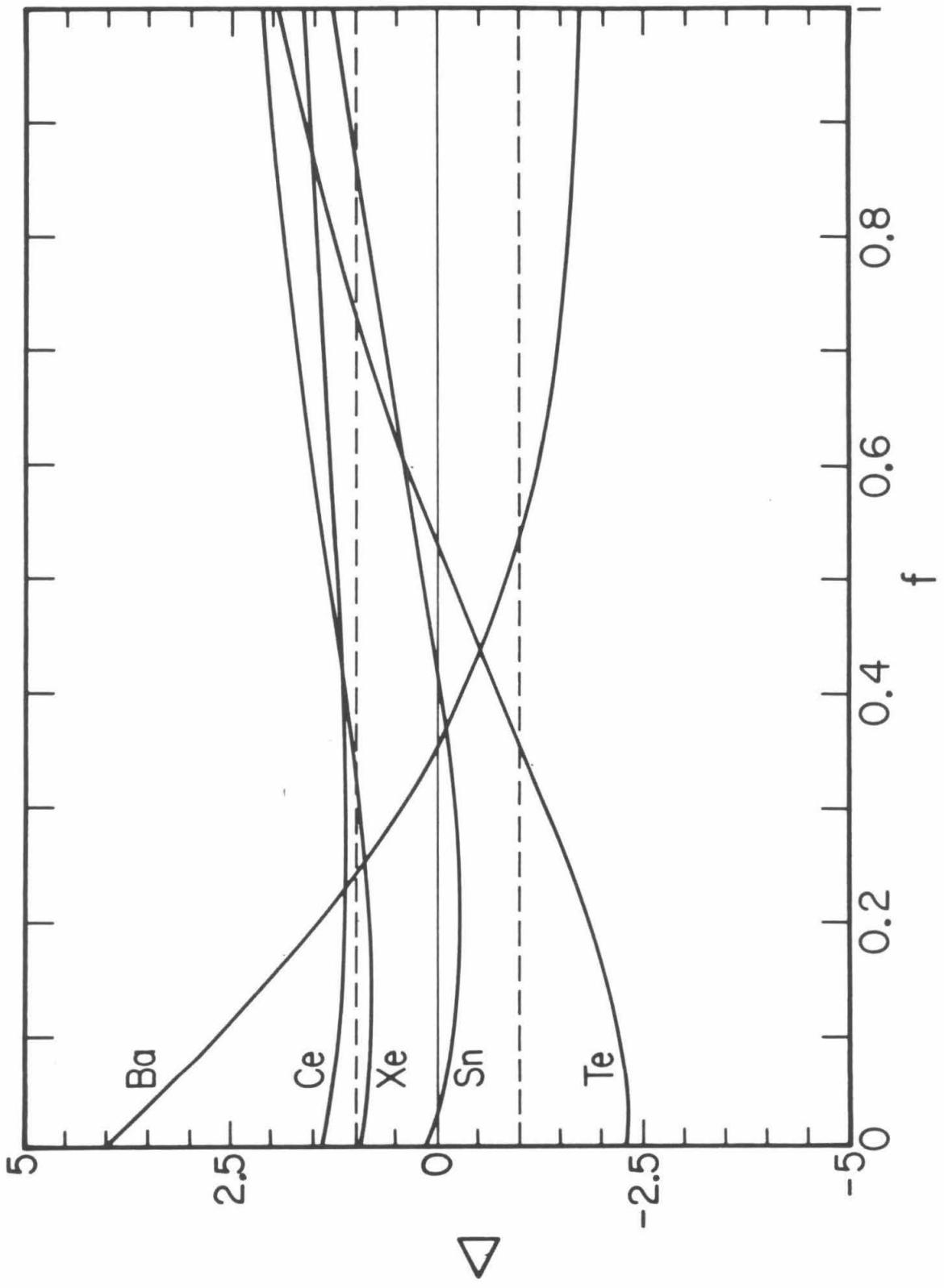
Ba
Ce
Xe
Sn
Te
5
2.5
0
-2.5
-5
0
0.2
0.4
0.6
0.8
f
▽

Figure 4.11

The results of our measurement and of the propagation calculation of Brewster, Freier and Waddington (1983) applied to r, s, and solar system sources both with and without first ionization potential (FIP) effects included are shown. The solid and dashed contours illustrate the 68% and 50% significance levels based on a χ^2 calculation using the three elements $_{50}$Sn, $_{52}$Te, and $_{56}$Ba.

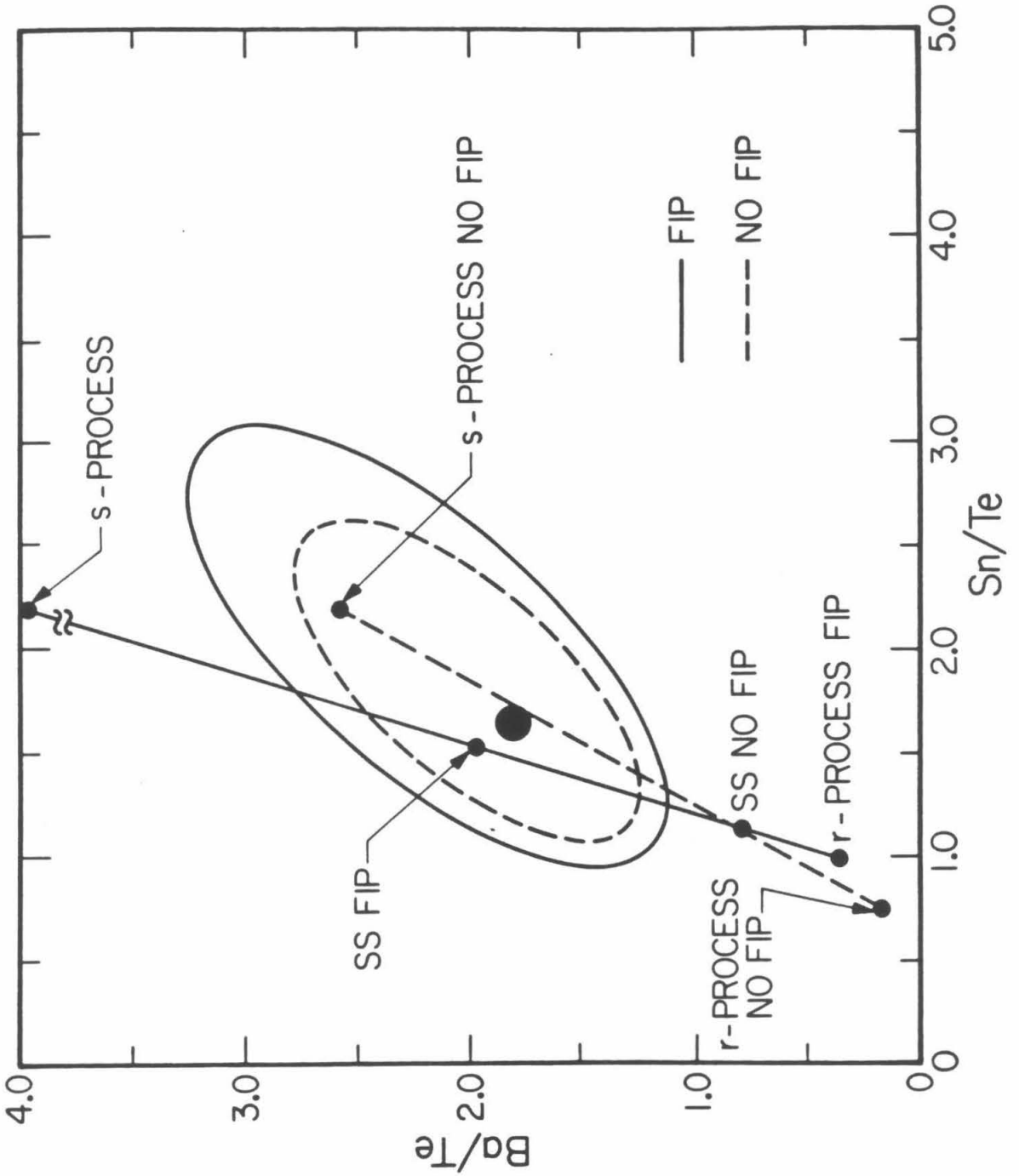
s-PROCESS
s-PROCESS NO FIP
FIP
NO FIP
SS FIP
SS NO FIP
r-PROCESS FIP
r-PROCESS NO FIP
Ba/Te
Sn/Te
0
1.0
2.0
3.0
4.0
5.0

and s-process material present. The data point is shown as the large filled circle surrounded by the 50% (dashed) and 68% (solid) χ^2 error contours. Their elliptical shape is the result of correlations arising from using Te as the normalizer for both axes. Also shown on the plot are the results from the Brewster, Freier, and Waddington propagations. The dashed line connects those points resulting from the pure r-process, the solar system, and the pure s-process, with no first ionization potential adjustments applied. The solid does the same for the FIP sources. These lines are "mixing lines" with position along the line indicating the relative amounts of r- and s-process material present, similar to the X_i used previously. This figure is consistent with the results obtained using all 5 elements. We are in agreement with both a solar system source with FIP applied and with an s-dominated mixture if no FIP is used. Using only the three elements $_{50}$Sn, $_{52}$Te, and $_{56}$Ba, we are inconsistent with a pure r-process source at the greater than 99% level whether or not first ionization potential effects are included. Consideration of model uncertainties reduces the significance of the difference with r-process plus FIP to the 98% level but leaves the no FIP r-process significance essentially unchanged.

4.6. Comparison with Other Measurements

Table 4.6 lists our results along with recent measurements from two other experiments, the Ariel VI electronic detector and a balloon borne plastic track detector (Fowler *et al.*, 1981). The balloon values are "subject to significant and rapidly charge-dependent corrections due to threshold effects for the tracks in plastic" (Fowler *et al.*, 1981). For the Ariel VI data, no claim of resolving the individual even elements in this charge range has been made.

Although the balloon data are consistent with a uniform distribution in this limited charge region, the Ariel VI results do posses a significant

Table 4.6
Experimental Results

Element	HEAO	Ariel VI	Balloon
$_{50}$Sn	1.65 ± 0.38	0.66 ± 0.22	1.21 ± 0.37
$_{52}$Te	1.00 ± 0.28	1.00 ± 0.23	1.00 ± 0.32
$_{54}$Xe	1.02 ± 0.27	0.34 ± 0.17	0.89 ± 0.27
$_{56}$Ba	1.80 ± 0.30	1.18 ± 0.23	0.87 ± 0.27
$_{58}$Ce	0.81 ± 0.25	0.29 ± 0.17	0.94 ± 0.27

structure, particularly the presence of a peak at charge 56. The difference between our results and the Ariel VI findings are significant at the 75% level using the same minimum χ^2 method discussed previously. If we perform the same analysis with the Ariel VI abundances as was done in Figures 4.7 and 4.8, we find that the χ^2 curves resemble ours in both the FIP and no FIP cases, although the value of χ^2 at the minimum is larger for the Ariel VI data in both cases.

4.7. Summary

In the previous sections we have shown that a pure r-process source is not consistent with our data either with or without adjustments for first ionization potential effects. The source composition requires a mixture of both the r- and the s-process. If one assumes that the cosmic ray abundances are altered by the same first ionization potential effects as seen at lower charges, then we are consistent with a solar system mixture of r- and s-process material. The best fit is obtained with a mixture which has

$$\frac{(r/s)_{CRS}}{(r/s)_{SS}} = 1.50^{+1.1}_{-0.7}$$

where CRS designates the cosmic ray source and SS the solar system. On the other hand, if no first ionization potential effects are considered, we are most consistent with an s-process dominated mixture having

$$\frac{(r/s)_{CRS}}{(r/s)_{SS}} = 0.20^{+0.18}_{-0.14}$$

and permitting an almost pure s-process source.

We cannot choose between the FIP and no FIP cases on the basis of the present data. Additional steps beyond the scope of this initial study will address such matters as obtaining an absolute normalization to the

iron region. This will help determine if the data points are consistent with a FIP plot of the sort shown in Figure 4.4. Although our results show that we can choose a mixture of r and s-process material which, when altered by a function of first ionization potential, matches the data, the normalization to iron is necessary to establish consistency with the other charge regions. If such can be shown to exist, the hypothesis of a solar system type source altered by ionization potential biases becomes an even more attractive possibility because of the wide charge range over which evidence of its effects are seen. As mentioned earlier, results in the charge 26 to 40 region, also from the HEAO Heavy Nuclei Experiment (Binns *et al.* 1982), show that the abundances are consistent with a solar system type composition altered by FIP.

The other possibility, that of almost pure s-process material, cannot be ruled out either. Results from passive balloon borne detectors indicated the presence of a substantial amount of r-process material in the cosmic radiation, based on the detection of a significant flux of trans-bismuth nuclei (Fowler *et al.* 1977). This result was in agreement with the intuitive association of both cosmic rays and the r-process with supernovae because of the extremes involved for both: cosmic ray energies and r-process neutron fluxes. However, recent results from this detector (Binns *et al.* 1982) have placed a more stringent upper limit on the actinide flux with the observation of only one possible actinide ($88 \leq Z \leq 100$) for some 100 platinum-lead ($74 \leq Z \leq 87$) nuclei, a result which is inconsistent with the earlier balloon measurements. The result is, nevertheless, still consistent with a solar system type mixture and does not require pure s-process material. However, being an upper limit, it does not rule out the possibility either.

Resolution of the r- and s-process composition of the cosmic radiation must await a comprehensive picture over the entire charge range to remove the free parameters remaining in our analysis. Although we have

been using combinations of solar system r- and s-process material in an attempt to reproduce our observations, it is possible that the cosmic ray r-process is not the same as that seen in the solar system. Nor for that matter can we be sure that the s-process is the same. The ledge-precipice structure seen in Figure 4.2 is a function of the cross sections of magic number isotopes along the s-process path. However, the relative levels of the plateaus, or ledges, is a function of the total neutron exposure, which may be different for the cosmic rays than for the solar system. The detection of a significant difference in abundances between elements on the different plateaus or ledges could be an indication of an s-process differing from that of the solar system. The most comprehensive picture, of course, would result from a measurement of the ultra-heavy isotopic abundances. But given the combination of the low fluxes of the ultra-heavies and the accuracy with which measurements must be made in order to resolve isotopes, this goal will not be realized for some time.

Appendix A

The following is a list of the time periods used in the analysis. Gaps of less than 0.1 days were ignored.

Start		End		
Year	Day	Year	Day	Δ t
79	268.0	79	268.3	0.3
79	268.5	79	317.0	48.5
79	318.1	79	340.0	22.0
79	341.0	79	347.0	6.0
79	348.1	79	366.0	17.9
80	2.0	80	7.0	5.0
80	8.1	80	86.1	78.0
80	87.0	80	92.0	5.0
80	93.1	80	93.9	0.8
80	94.0	80	100.5	6.5
80	101.0	80	108.0	7.0
80	109.1	80	131.1	22.0
80	133.0	80	210.0	77.0
80	211.0	80	228.1	17.1
80	230.0	80	262.8	32.7
80	263.1	80	300.0	36.9
80	300.1	80	355.3	55.2

Appendix B

The decomposition presented in detail in Chapter 4 for the even charge elements in the Sn-Ce region was also done for all of the elements with charge greater than 50 in order to have a consistent set of abundances to propagate over the whole charge range. The r- and s-process abundances that result are listed here. As before, the solar system abundances are from Anders and Ebihara (1982), and the s-process is that of Käppeler *et al.* (1982). The method is the same as detailed in Chapter 4 with s-only isotope abundances directly from Käppeler *et al.* and p-process isotopes ignored. The abundances marked with [b] were indicated as having s-process branches by Käppeler *et al.*. This branching was ignored in the assigments made here since the effect on the Sn-Ce region is small.

Element	Solar System	s process	r process
48 Cd	1.69	0.859	0.691
49 In	0.184	0.0617	0.114
50 Sn	3.82	2.123	1.52
51 Sb	0.352	0.0442	0.308
52 Te	4.91	0.928	3.96
53 I	0.90	0.0437	0.856
54 Xe	4.35	0.660	3.676
55 Cs	0.372	0.0428	0.329
56 Ba	4.36	4.11	0.286
57 La	0.448	0.298	0.150
58 Ce	1.16	0.765	0.390
59 Pr	0.174	0.0764	0.098
60 Nd	0.835	0.369	0.390
62 Sm [b]	0.262	0.0608	0.1810
63 Eu [b]	0.0972	0.00398	0.0932
64 Gd	0.331	0.0395	0.2892
65 Tb	0.0589	0.00323	0.0557
66 Dy	0.398	0.0631	0.3328
67 Ho	0.0875	0.00493	0.0826

Element	Solar System	s process	r process
68 Er	0.253	0.0414	0.2073
69 Tm	0.0386	0.00539	0.0332
70 Yb	0.243	0.0664	0.1764
71 Lu [b]	0.0370	0.00563	0.0313
72 Hf [b]	0.176	0.0658	0.1097
73 Ta	0.0226	0.00687	0.0157
74 W	0.137	0.0474	0.0895
75 Re	0.0533	0.00346	0.0498
76 Os	0.714	0.0506	0.6606
77 Ir [b]	0.660	0.0662	0.594
78 Pt	1.37	0.0581	1.312
79 Au	0.186	0.00783	0.178
80 Hg	0.52	0.2068	0.270
81 Tl	0.184	0.0831	0.1011
82 Pb	3.13	0.819	2.310
83 Bi	0.144	0.0163	0.128
90 Th	0.0420	0.0	0.0420
92 U	0.0238	0.0	0.0238

Element	A	Solar System	s-process	r-process
48 Cd	106	0.0199	0.0	0.0
	108	0.0142	0.0	0.0
	110	0.199	0.194	0.0
	111	0.204	0.0789	0.125
	112	0.383	0.207	0.176
	113	0.194	0.0842	0.110
	114	0.456	0.295	0.161
	116	0.119	0.0	0.119
49 In	113	0.0079	0.0	0.0
	115	0.176	0.0617	0.114
50 Sn	112	0.0386	0.0	0.0
	114	0.0256	0.0	0.0
	115	0.0145	0.0	0.0
	116	0.565	0.458	0.0
	117	0.296	0.105	0.191
	118	0.929	0.655	0.274
	119	0.329	0.156	0.173
	120	1.24	0.749	0.49
	122	0.174	0.0	0.174
	124	0.215	0.0	0.215
51 Sb	121	0.202	0.0442	0.158
	123	0.150	0.0	0.150
52 Te	120	0.0045	0.0	0.0
	122	0.123	0.121	0.0
	123	0.044	0.0401	0.0

	124	0.226	0.211	0.0
	125	0.344	0.0823	0.262
	126	0.918	0.474	0.444
	128	1.56	0.0	1.56
	130	1.69	0.0	1.69
53 I	127	0.90	0.0437	0.856
54 Xe	124	0.00496	0.0	0.0
	126	0.00483	0.0	0.0
	128	0.0939	0.108	0.0
	129	1.20	0.0603	1.14
	130	0.189	0.176	0.0
	131	0.941	0.0619	0.879
	132	1.15	0.254	0.896
	134	0.421	0.0	0.421
	136	0.34	0.0	0.34
55 Cs	133	0.372	0.0428	0.329
56 Ba	130	0.00462	0.0	0.0
	132	0.00440	0.0	0.0
	134	0.106	0.131	0.0
	135	0.287	0.0627	0.224
	136	0.342	0.359	0.0
	137	0.488	0.446	0.042
	138	3.13	3.11	0.02
57 La	138	0.00040	0.0	0.0
	139	0.448	0.298	0.150
58 Ce	136	0.0022	0.0	0.0
	138	0.0029	0.0	0.0

	140	1.026	0.765	0.261
	142	0.129	0.0	0.129
59 Pr	141	0.174	0.0764	0.098
60 Nd	142	0.227	0.151	0.0
	143	0.101	0.0292	0.072
	144	0.199	0.112	0.087
	145	0.0694	0.0158	0.0536
	146	0.144	0.0607	0.083
	148	0.0477	0.0	0.0477
	150	0.0468	0.0	0.0468
62 Sm	144	0.0081	0.0	0.0
	147 [b]	0.0406	0.00605	0.0346
	148	0.0295	0.0247	0.0
	149	0.0363	0.00263	0.0337
	150	0.0193	0.0118	0.0
	152 [b]	0.0694	0.0156	0.0536
	154	0.0589	0.0	0.0589
63 Eu	151 [b]	0.0466	0.00149	0.0451
	153 [b]	0.0506	0.00249	0.0481
64 Gd	152	0.00066	0.0	0.0
	154	0.00695	0.00524	0.0
	155	0.0490	0.00246	0.0465
	156	0.0682	0.0119	0.0563
	157	0.0520	0.00452	0.0475
	158	0.0821	0.0154	0.0667
	160	0.0722	0.0	0.0722
65 Tb	159	0.0589	0.00323	0.0557

66 Dy	156	0.000227	0.0	0.0
	158	0.000398	0.0	0.0
	160	0.00915	0.00818	0.0
	161	0.0756	0.00232	0.0733
	162	0.101	0.0137	0.0873
	163	0.0991	0.00402	0.0951
	164	0.112	0.0349	0.0771
67 Ho	165	0.0875	0.00493	0.0826
68 Er	162	0.000354	0.0	0.0
	164	0.00395	0.0	0.0
	166	0.0845	0.0120	0.0725
	167	0.0579	0.00431	0.0536
	168	0.0686	0.0251	0.0435
	170	0.0377	0.0	0.0377
69 Tm	169	0.0386	0.00539	0.0332
70 Yb	168	0.000328	0.0	0.0
	170	0.00753	0.00782	0.0
	171	0.0350	0.00415	0.0309
	172	0.0532	0.0145	0.0387
	173	0.0394	0.00686	0.0325
	174	0.0768	0.0331	0.0437
	176	0.0306	0.0	0.0306
71 Lu	175	0.0359	0.00457	0.0313
	176 [b]	0.00106	0.00106	0.0
72 Hf	174	0.00028	0.0	0.0
	176 [b]	0.00902	0.00902	0.0

	177	0.0327	0.00383	0.0289
	178	0.0477	0.0172	0.0305
	179	0.0241	0.00420	0.0199
	180	0.0620	0.0316	0.0304
73 Ta	180	2.78e-06	0.0	0.0
	181	0.0226	0.00687	0.0157
74 W	180	0.000178	0.0	0.0
	182	0.0360	0.0169	0.0191
	183	0.0196	0.00980	0.0098
	184	0.0421	0.0207	0.0214
	186	0.0392	0.0	0.0392
75 Re	185	0.0190	0.00346	0.0155
	187	0.0343	0.0	0.0343
76 Os	184	0.000129	0.0	0.0
	186	0.0115	0.0116	0.0
	187	0.0089	0.00566	0.0
	188	0.0954	0.0128	0.0826
	189	0.115	0.00336	0.112
	190	0.189	0.0172	0.172
	192	0.294	0.0	0.294
77 Ir	191	0.246	0.00383	0.242
	193 [b]	0.414	0.0624	0.352
78 Pt	190	0.000178	0.0	0.0
	192	0.0107	0.0106	0.0
	194	0.451	0.0128	0.438
	195	0.463	0.00474	0.458
	196	0.347	0.0300	0.317

	198	0.0986	0.0	0.0986
79 Au	197	0.186	0.00783	0.178
80 Hg	196	0.00078	0.0	0.0
	198	0.052	0.0103	0.0
	199	0.0874	0.0129	0.0745
	200	0.120	0.0635	0.056
	201	0.0686	0.0329	0.0357
	202	0.155	0.0872	0.068
	204	0.0359	0.0	0.0359
81 Tl	203	0.0542	0.0255	0.0287
	205	0.130	0.0576	0.0724
82 Pb	204	0.0612	0.0606	0.0
	206	0.594	0.180	0.414
	207	0.644	0.176	0.468
	208	1.830	0.402	1.428
83 Bi	209	0.144	0.0163	0.128
90 Th	232	0.0420	0.0	0.0420
92 U	235	0.00573	0.0	0.00573
	238	0.0181	0.0	0.0181

REFERENCES

Anders, E. and Ebihara, M. 1982, "Solar System Abundances of the Elements", *Geochim. Cosmochim. Acta*, **46**, 2363.

Allen, B.J., Gibbons, J.H., and Macklin, R.L. 1971, "Nucleosynthesis and Neutron-Capture Cross Sections", *Adv. Nuc. Phys*, **4**, 205.

Arnett, W.D. 1973, "Explosive Nucleosynthesis in Stars", *Ann. Rev. Astron. Ap.*, **11**, 73.

Bevington, P.R. 1969, *Data Reduction and Error Analysis for the Physical Sciences*, McGraw-Hill, New York.

Binns, W.R., Israel, M.H., Klarmann, J., Scarlett, W.R., Stone, E.C., and Waddington, C.J. 1981a, "The UH-Nuclei Cosmic Ray Detector on the Third High Energy Astronomy Observatory", *Nucl. Inst. Meth.*, **185**, 415.

Binns, W.R., Fickle, R.K., Garrard, T.L., Israel, M.H., Klarmann, J., Stone, E.C., and Waddington, C.J. 1981b, "Cosmic-Ray Abundances of Elements with Atomic Number $26 \leq Z \leq 40$ Measured on HEAO 3", *Ap. J. (Letters)*, **247**, L115.

Binns, W.R., Fickle, R.K., Garrard, T.L., Israel, M.H., Klarmann, J., Stone, E.C., and Waddington, C.J. 1982, "The Abundance of the Actinides in the Cosmic Radiation as Measured on HEAO 3", *Ap. J. (Letters)*, **261**, L117.

Binns, W.R., Fickle, R.K., Garrard, T.L., Israel, M.H., Klarmann, J., Krombel, K.E., Stone, E.C., and Waddington, C.J. 1983, "Cosmic Ray Abundances of

Sn, Te, Xe, and Ba Nuclei Measured on HEAO 3", *Ap. J. (Letters)*, **267**, L93.

Binns, W.R. 1980, "Mass Properties of Instrument", HEAO C-3 Internal Report WRB-05.

Blake, J.B. and Schramm, D.N. 1976, "A Possible Alternative to the r-Process", *Ap. J.*, **209**, 846.

Blake, J.B. and Margolis, S.H. 1981, "Indicators of Nucleosynthesis and and Acceleration Processes in the Ultraheavy Cosmic Rays: $24 \leq Z \leq 59$, *Ap. J.*, **251**, 402.

Brewster, N.R., Freier, P.S., and Waddington, C.J. 1983, "The Propagation of Ultraheavy Cosmic Ray Nuclei", *Ap. J.*, **264**, 324.

Burbidge, E.M., Burbidge, G.R., Fowler, W.A., and Hoyle, F. 1957, "Synthesis of the Elements in Stars", *Rev. Mod. Phys.*, **29**, 547.

Cameron, A.G.W. 1955, "Origin of Anomalous Abundances of the Elements in Giant Stars", *Ap. J.*, **121**, 144.

Cameron, A.G.W. 1960, "New Neutron Sources of Possible Astrophysical Importance" - Abstract of Paper Presented at the 106th Meeting of the American Astronomical Society, August 22-25, 1960 at the Universidad Nacional de Mexico, Mexico City, *Astron. J.*, **65**, 485.

Cameron, A.G.W. 1968, "A New Table of Abundances of the Elements in the Solar System", in *Origin and Distribution of the Elements*, ed. L.H. Ahrens, (New York: Pergamon Press), p 125.

Cameron, A.G.W. 1973, "A Critical Discussion of the Abundances of Nuclei", in *Explosive Nucleosynthesis*, ed. D.N. Schramm and W.D. Arnett, (Austin: University of Texas Press), p 3.

Cameron, A.G.W. 1982a, "The Heavy Element Yields of Neutron Capture Nucleosynthesis", *Ap. Space Sci.*, **82**, 123.

Cameron, A.G.W. 1982b, "Elemental and Nuclidic Abundances in the Solar System", in *Essays in Nuclear Astrophysics*, ed. C.A. Barnes, D.D. Clayton, and D.N. Schramm (New York: Cambridge University Press), p 23.

Cassé, M. and Goret, P. 1978, "Ionization Models of Cosmic Ray Sources", *Ap. J.*, **221**, 703.

Cowan, J.J., Cameron, A.G.W, and Truran, J.W. 1983, "Explosive Helium Burning in Supernovae: A Source of r-Process Elements", *Ap. J.*, **265**, 429.

Cowsik, R., Pal, Yash, Tandon, S.N., and Verma, R.P. 1967, "Steady State of Cosmic Ray Nuclei - Their Spectral Shape and Pathlength at Low Energies", *Phys. Rev.*, **158**, 1238.

Derrickson, J.H., Eby, P.B., and Watts, J.W. 1981, "The Predicted Deviation from the Z^2 Dependence of the Ion Chamber and the Cherenkov Counter Response on the HEAO-3 Experiment", *Proc. 17th Int. Cosmic Ray Conf.* (Paris), **8**, 88.

Fleischer, R.L., Price, P.B., Walker, R.M., Maurette, M., and Morgan, G. 1967, "Tracks of Heavy Primary Cosmic Rays in Meteorites", *J. Geophys. Res.* , **72**, 355.

Fowler, P.H. 1977, "Ultra Heavy Cosmic Rays", *Proc. 13th Int. Cosmic Ray Conf.* (Denver), **5**, 3627.

Fowler, P.H., Walker, R.N.F., Masheder, M.R.W., Moses, R.T., and Worley, A. 1981, *Nature*, **291**, 45.

Garrard, T.L. 1979a, "HNE Library Generator", Space Radiation Lab Technical Report 78-3.

Garrard, T.L. 1979b, "Stoermer Cutoff Calculation, Cutoff Algorithm", HEAO C-3 Internal Report TLG-2.

Garrard, T.L. 1980, "Note on Ckv Map", HEAO C-3 Internal Report TLG-11.

Garrard, T.L. and Ennis, J. 1980a, "Determination of Forbidden Particle Trajectories", HEAO C-3 Internal Report TLG-7.

Garrard, T.L. and Ennis, J. 1980b, "Determination of Forbidden Particle Trajectories", HEAO C-3 Internal Report TLG-7B.

Greiner, D.E., Lindstrom, P.S., Heckman, H.H., Cork, Bruce, and Breser, F.S. 1975, "Momentum Distribution of Isotopes Produced by Fragmentation of Relativistic ^{12}C and ^{16}O Projectiles", *Phys. Rev. Letters*, **35**, 152.

Israel, M.H., Klarmann, J., Love, P.L., and Tueller, J. 1979, "Cosmic Ray Abundances in the Interval $26 \leq Z \leq 40$", *Proc. 16th Int. Cosmic Ray Conf.* (Kyoto), **12**, 65.

Israel, M.H. 1979, "Crude C Agreement", HEAO C-3 Internal Report MI-19.

Israel, M.H. 1980, "Empirical Functions of C/I for ZEST and for Energy", HEAO C-3 Internal Report MI-22.

Israel, M.H., Klarmann, J., Binns, W.R., Fickle, R.K., Waddington, C.J., Garrard, T.L., and Stone, E.C. 1981, "Implications of Ultraheavy Cosmic Ray Source Composition Derived from Observations by the HEAO-3 Heavy Nuclei Experiment", *Proc. 17th Int. Cosmic Ray Conf.* (Paris), 2, **36**.

Janni, J.F. 1966, "Calculation of Energy Loss, Range, Pathlength, Straggling, Multiple Scattering, and the Probability of Inelastic Nuclear Collisions for 0.1 to 1000 MeV Protons", Technical Report No. AFWL-TR-65-150, Air Force Weapons Laboratory, Kirtland Air Force Base, New Mexico.

Käppeler, F., Beer, H., Wisshak, K., Clayton, D.D., Macklin, R.L., and Ward, R.A. 1982, "s-Process Studies in the Light of New Experimental Cross Sections: Distribution of Neutron Fluences and r-Process Residuals", *Ap. J.*, **257**, 821.

Krombel, K.E. 1980, "Charge Estimation Including Energy Loss", HEAO C-3 Internal Report KK-03.

Letaw, J.R., Silberberg, R., and Tsao, C.H. 1983, "Proton Nucleus Total Inelastic Cross Sections: An Empirical Formula for E > 10 MeV", *Ap. J. Suppl.*, **51**, 271.

Linder, H.G. 1979, "Data Processing Plan for High Energy Astronomy Observatory-C (HEAO-C)", Document X-565-79-6, Goddard Space Flight Center, Greenbelt, Maryland.

Mewaldt, R.A. 1983, "The Elemental and Isotopic Composition of Galactic

Cosmic Ray Nuclei", to be published in *Reviews of Geophysics and Space Physics* as part of the U.S. Quadrennial Report tc the IUGG (1979-1982).

Norman, E.B. and Schramm, D.N. 1979, "On the Conditions Required for the r-process", *Ap. J.*, **228**, 881.

Roederer, J.G. 1970, *Dynamics of Geomagnetically Trapped Radiation*, Springer, New York.

Schramm, D.N. 1973, "The Dynamic r-Process", in *Explosive Nucleosynthesis*, ed. D.N. Schramm and W.D. Arnett (Austin: University of Texas Press), p 84.

Shirk, E.K. and Price, P.B. 1978, "Charge and Energy Spectra of Cosmic Rays with $Z \geq 60$: The *Skylab* Experiment", *Ap. J.*, **220**, 719.

Stone, E.C. and Wiedenbeck, M.E. 1979, "A Secondary Tracer Approach to the Derivation of Galactic Cosmic-Ray Source Isotopic Abundances", *Ap. J.*, **231**, 606.

Störmer, C. 1955, *The Polar Aurora*, Oxford University Press, London.

Westfall, G.D., Wilson, L.W., Lindstrom, P.J., Crawford, H.J., Greiner, D.E., and Heckman, H.H. 1979, "Fragmentation of Relativistic ^{56}Fe", *Phys. Rev. C*, **19**, 1309.